DNA Nanostructures in Advanced Plasmonic Applications

Kevin Martens

DNA Nanostructures in Advanced Plasmonic Applications

Kevin Martens

München 2022

DNA Nanostructures in Advanced Plasmonic Applications

Kevin Martens

Dissertation
an der Fakultät für Physik
der Ludwig-Maximilians-Universität
München

vorgelegt von
Kevin Martens
aus Starnberg

München, den 13. April 2022

Erstgutachter: Prof. Dr. Tim Liedl
Zweitgutachter: Prof. Dr. Alexander Govorov
Tag der mündlichen Prüfung: 1. Juni 2022

Abstract

Chiral structures can be found anywhere from particle physics over electromagnetism to chemistry and biology. Although circular dichroism (CD) has long been used to trace changes of protein configurations or chiral molecular states, chiral plasmonic nanostructures have only shown their potential in recent years. The ability to design nanostructures with tailored geometries and specific functions on the nanoscale is one of the possibilities offered by DNA nanotechnology.

In this thesis, we use DNA origami to assemble model meta-molecules from multiple plasmonic particles, accurately positioned in space. This approach allows us to build up varying molecular geometries piece by piece and study their impact on their surrounding optical near fields, confirming numerical simulations elucidating the intricate chiral optical fields in complex architectures. With this, we studied the emergence of CD signatures by step-wise constructing of a gold nanohelix, composed of single spherical nanoparticles. In this, we were able to show the effects of varying geometries by implementing sign flipping signals through addition or removal of single particles.

We furthermore studied the effects of a spherical transmitter particle situated within a pair of nanorods in a chiral geometry. The transmitter particle not only enhances the CD response and causes a redshift of the plasmonic resonance frequency of the nanorods, it also triggers the emergence of an additional chiral signal at the resonance frequency of the nanosphere.

In conclusion, we present an approach of utilizing specific plasmonic heating effects to construct a novel type of DNA nanowalker: a nanowheel. Unlike previous DNA walkers, which are based on the process of strand displacement, this nanowheel is fueled by light and could therefore potentially reach significantly higher speeds than any previous attempts.

Zusammenfassung

Chirale Strukturen sind überall zu finden, von der Teilchenphysik über den Elektromagnetismus bis hin zur Chemie und Biologie. Obwohl der Zirkulardichroismus schon lange genutzt wird, um Veränderungen der Proteinkonfiguration oder chirale Molekülzustände nachzuweisen, haben chirale plasmonische Nanostrukturen ihr Potenzial erst in den letzten Jahren gezeigt. Die Fähigkeit, Nanostrukturen mit maßgeschneiderten Geometrien und spezifischen Funktionen auf der Nanoskala zu entwerfen, gehört zu den Möglichkeiten, die die DNA-Nanotechnologie bietet.

In dieser Arbeit verwenden wir DNA-Origami, um Modell-Metamoleküle aus mehreren plasmonischen Partikeln zusammenzusetzen, die genau im Raum positioniert sind. Dieser Ansatz ermöglicht es uns, verschiedene Molekülgeometrien Stück für Stück aufzubauen und ihre Auswirkungen auf die sie umgebenden optischen Nahfelder zu studieren, wobei die komplizierten chiralen optischen Felder in solch komplexen Architekturen durch numerische Simulationen aufgeklärt werden. Auf diese Weise haben wir die Entstehung von Zirkulardichroismus durch den schrittweisen Aufbau einer Gold-Nanohelix untersucht, die aus einzelnen kugelförmigen Nanopartikeln besteht. Dabei konnten wir die Auswirkungen unterschiedlicher Geometrien aufzeigen, indem wir durch Hinzufügen oder Entfernen einzelner Partikel eine Vorzeichenumkehr in den Signalen implementierten.

Darüber hinaus untersuchten wir die Auswirkungen eines kugelförmigen Transmitterpartikels, das sich innerhalb eines Paares von Nanorods in einer chiralen Geometrie befindet. Das Transmitterpartikel verstärkt nicht nur den Zirkular-dichroismus und bewirkt eine Rotverschiebung der plasmonischen Resonanzfrequenz der Nanorods, sondern löst auch das Auftreten eines zusätzlichen chiralen Signals auf Höhe der Resonanzfrequenz der Nanosphäre aus.

Zum Schluss stellen wir einen Ansatz zur Anwendung der spezifischen plasmonischen Heizeffekte vor, um eine neue Art von DNA-Nanowalker - ein Nanowheel - zu konstruieren. Im Gegensatz zu bisherigen DNA-Walkern, die auf dem Prozess des Strand Displacements beruhen, wird dieses Nanowheel durch Licht angetrieben und könnte

daher potenziell deutlich höhere Geschwindigkeiten erreichen als alle bisherigen Versuche.

Acknowledgments

Tim

Vielen Dank für die Unterstützung über all die Jahre. Du hast seit meiner Bachelor Arbeit im Jahre 2013, trotz aller Schwierigkeit in meiner Forschung, stehts an mich geglaubt und hast alles dafür getan, dass ich schlussendlich mein Potential erfüllen konnte.

The Group

Thank you so much for everybody who came and went over all those years. I will always remember all the work, but also all the fun and laughers we shared. Special thanks to Prof. Kitzerow, Susi, Tao, Timon, Eva, Francesca, Linh, Wooli, Mauricio and Amelie for everything you taught me.

The Chair

Thanks to everybody in the Rädler chair for a wonderful working environment over all these years. I had an amazing time with you during all the 3pm cakes, lunch breaks, PhD parties, kicker tournaments, excursions, and most importantly, Antholz trips.

The Rest

Thanks to everybody who supported me during my studies. My fellow students during my bachelors and masters at LMU, I could have never done it alone. All my friends and family, who endured all my complaints and also countless narrations of things you neither understand nor care about. Also, thanks to everybody working at LMU for creating such a helpful environment for learning and growth.

Content

I Background and Literature 1

1 Straightforward Summary for the Public 3

2 DNA Nanotechnology

2.1 DNA 9

2.2 Early DNA Nanotechnology 12

2.3 DNA Origami 15

2.4 Applications 19

3 Plasmonics

3.1 The Drude Model 25

3.2 Nanoplasmonics 26

3.3 Plasmonic Circular Dichroism 31

4 Methods

4.1 Introduction to Microscopy 35

4.2 Dark-field Microscopy 36

4.3 Transmission Electron Microscopy 38

II Experiments

5 Large Pitch and Small Pitch Helix

5.1 Introduction 45

5.2 Chirality 47

5.3 Experiments and Discussion 48

5.4 Theoretical Model 52

5.5 Conclusion 53

6 Chirality Transfer

6.1 Introduction 55

6.2 Experiments 57

6.3 Numerical Simulations 60

6.4 Discussion 61

6.5 Conclusion 63

7 Towards the Nanowheel

7.1 Introduction 65

7.2 Design 66

7.3 Experiments 69

7.4 Conclusion 72

8 Conclusion 73

III Appendix

Appendix

A.1 Materials 77

A.2 DNA Origami Design 77

A.3 DNA Origami Synthesis 85

A.4 DNA Origami Nanoparticles Assembly Synthesis 99

A.5 CD and Extinction Measurements 122

A.6 Numerical Simulations 123

Bibliography 127

I

Background and Literature

Chapter 1

Straightforward Summary for the Public

This chapter will explain the thesis in simple terms for the general public in German

Wenn sich die Wissenschaft mit DNA beschäftigt denken die meisten Leuten an Gentechnologie. Das Genom, die Bauanleitung für jedes Lebewesen auf unserem Planeten, übt eine große Faszination auf die Menschheit aus. Die Tinte mit der diese Bauanleitung geschrieben ist, ist die DNA. Nachdem wir gelernt haben sie zu lesen und zu verstehen haben wir im nächsten Schritt Möglichkeiten entwickelt sie umzuschreiben. Dies offenbart unvorstellbare Möglichkeiten, bringt aber auf viele Gefahren und ethische Probleme mit sich. Es gibt jedoch noch einen anderen Bereich der Wissenschaft, der sich mit der DNA beschäftigt. Bei diesem steht nicht im Fokus, was mit der Tinte geschrieben wird, sondern die Tinte selbst und die Frage: wofür können wir die Tinte sonst noch verwenden? Diese Arbeit handelt von einem Bereich der Wissenschaft, bei dem die Tinte als Baumaterial verwendet wird. Wir nennen dies DNA-Nanotechnologie.

Um dies zu verstehen, müssen wir uns mit dem Aufbau der DNA beschäftigen. Die DNA ist ein längliches Molekül, welches im Normalfall aus zwei Einzelsträngen besteht, die durch eine Reihe von 4 unterschiedlichen Basen der Länge nach miteinander verbunden sind, wie in Abbildung 1.1a gezeigt. Die Reihenfolge dieser Basen stellt den genetischen Code dar, um einen Menschen zu codieren benötigt man 3 Milliarden Basenpaare. Der doppelsträngige Aufbau wird in der Natur dafür verwendet den genetischen Code, die Erbinformation, schnell und einfach kopieren zu können. Anders betrachtet kann man jedoch auch sagen, wenn DNA Einzelstränge die passende Basensequenzen zueinander haben, verbinden sie sich miteinander. Dies bedeutet man kann 2 DNA Einzelstränge mit komplementärer Basensequenzen zueinander einfach in einer Flüssigkeit lösen und sie werden sich von alleine miteinander verbinden. Man kann jedoch auch 4 DNA Einzelstränge synthetisieren, die alle jeweils zur Hälfte mit einem Einzelstrang komplementär sind und zur anderen Hälfte mit einem anderen, siehe Abbildung 1.1b. Auf

diese Weise wird eine Art Knoten aus DNA gebildet. Diese so genannte Holliday Junction bildet den Grundstein der DNA-Nanotechnologie und ist als 3D Modell in Abbildung 1.1c dargestellt.

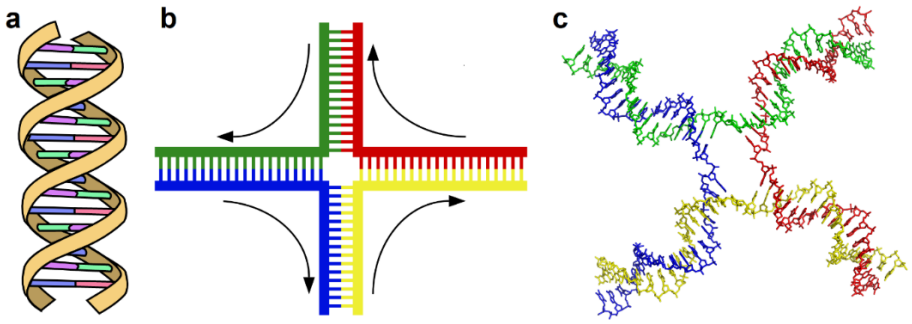

Abbildung 1.1: **a**) Vereinfachte Darstellung einer DNA-Doppelhelix. **b**) Konzeptuelle und **c**) 3D Darstellung einer Holliday Junction. Illustrationen von Leyo, Mouagip und Zephyris, verbreitet unter CC BY-SA 3.0 [1].

Aufbauend auf dieser Grundidee wurden immer mehr, zunehmend kompliziertere Strukturen aus DNA entworfen, wie z.B. einen Würfel aus DNA-Strängen, zu sehen in Abbildung 1.2a. Zunächst verwendete man dafür nur kurze DNA-Stränge mit maximal 50 Basenpaaren und passend synthetisierten Basensequenzen. Bald kam jedoch die Idee auf einen längeren DNA-Strang (ca. 8000 Basenpaare) aus einem Bakteriophagen zu gewinnen und diesen mit zahlreichen kürzeren DNA-Strängen in eine gewünschte Form zu bringen. Mit dieser Technik, DNA-Origami genannt, lassen sich größere Strukturen und stabilere Strukturen entwerfen, bei dessen Design man fast keine Einschränkungen hat. Ein paar einfacher Beispiele sind in Abbildung 1.2b dargestellt.

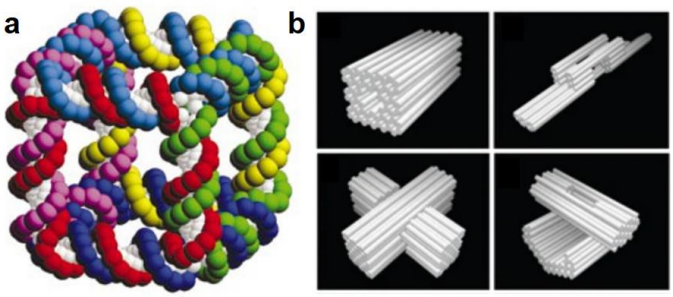

Abbildung 1.2: **a**) Würfel aus DNA-Strängen und **b**) verschieden Beispiele für DNA-Origami Strukturen als 3D Modelle. Wiederverwendet aus [2, 3], mit Genehmigung von Springer Nature.

Mit dieser Technik lassen sich nun also Strukturen in Größen von ungefähr 100 nm (0,0001 mm) herstellen, doch wofür kann man diese verwenden? Aktuell existieren sehr viele Ideen und Ansätze für Anwendungen in verschiedenen Bereichen, wie z.B. Nanoroboter, die verschiedene Funktionen innerhalb des menschlichen Körpers ausführen können. Der Fokus dieser Arbeit liegt jedoch auf einer grundlegenderen Anwendung, nämlich der Erforschung der Nanowelt.

Die Nanowelt folgt anderen Regeln als wir sie aus unserer Makrowelt gewohnt sind, obwohl ihr natürlich die gleichen Naturgesetze zu Grunde liegen. Ein einfaches Beispiel hierfür ist Metall. Wir wissen, das Metall glänzt. Das bedeutet, wenn Licht auf eine metallische Oberfläche trifft, wird es reflektiert. In wirklich ist das jedoch nur die halbe Wahrheit. Wenn man das Ganze auf der Nanoebene betrachtet, stellt man fest, dass das Licht erst in das Metall eindringt, bevor es reflektiert wird. Diese Eindringtiefe beträgt ungefähr 200 nm für Gold, vernachlässigbar in der Makrowelt. Wenn ein Goldpartikel, jedoch kleiner als dies Eindringtiefe ist, verändert sich das optische Verhalten im Vergleich zu Gold in der Makrowelt vollkommen. Ein Gold Nanopartikel reflektiert das Licht nicht, stattdessen können seine freien Elektronen durch eine elektromagnetische Welle wie das Licht angeregt werden und absorbieren Licht einer bestimmten Wellenlänge. Anstatt der goldenen Farbe, die durch Reflektion des Lichts entsteht, haben Gold Nanopartikel eine rote Farbe, weil diese auf der Absorption des Lichts beruht, ähnlich wie im Bespiel des Lykurgus Bechers in Abbildung 1.3. Um dieses Phänomen, genannt Plasmonik, genauer experimentell untersuchen zu können benötigt man Strukturen die Goldpartikel auf der Nanoebene platzieren können. An dieser Stelle kommt die DNA-Nanotechnologie ins Spiel.

Abbildung 1.3: Der Lykurgus Becher hat eine andere Farbe bei der Beleuchtung von vorne, wobei die Farbe auf Reflektion beruht, als bei der Beleuchtung von hinten, wobei die Farbe auf Absorption beruht. (British Museum, London, verbreitet unter CC BY-NC-SA 4.0)

DNA-Stränge können sich nicht nur miteinander verbinden, sie können auch mit bestimmten chemikalischen Stoffen modifiziert werden, wie z.B. Thiolgruppen. Diese Thiolgruppen haben eine hohe Affinität zu Gold, somit können Goldpartikel mit derart modifizierten DNA-Strängen umhüllt werden. Diese DNA-Stränge können sich dann wiederum mit komplentären DNA-Einzelsträngen verbinden, die aus einem DNA-Origami herausragen. Mit dieser Technik kann man mehrere verschiedene Goldpartikel an bestimmte Stellen eines DNA-Origamis anbinden, man kann also ihre Distanz und Ausrichtung zu einander frei bestimmen. Dies ist deswegen so interessant, weil die im letzten Absatz erwähnten Oszillationen innerhalb der Nanopartikel, die sogenannten plasmonischen Schwingungen, mit anderen Nanopartikeln in ihrer Nähe koppeln können. Dies wird besonders interessant, wenn die Partikel in einer chiralen Anordnung vorliegen. Chiralität bedeutet so viel wie Händigkeit, geometrische Formationen, die keine Drehspiegelachse besitzen sind chiral. Solche Anordnungen von Nanopartikeln absorbieren nicht nur Licht einer bestimmten Wellenlänge, sondern auch Licht einer bestimmten Polarisation. Das bedeutet sie absorbieren linksdrehendes Licht anders als rechtsdrehendes Licht, dies nennt man Zirkulardichoismus. Da es unzählige verschiedene Möglichkeiten gibt für chirale Anordnungen mit Nanopartikeln, gibt es auch unzählige verschiedene Signale die entdeckt und erforscht werden können und die DNA-Nanotechnologie macht es möglich all diese zu synthetisieren und zu messen.

In dieser Arbeit habe ich mich zwei verschiedenen Arten von chiralen Nanopartikel Anordnungen beschäftigt. Zum einen habe ich Helices aus Goldpartikeln erforscht. Wie in Abbildung 1.4 zu sehen ist, hat so einen Goldhelix in ihrer Mitte ein DNA-Origami, welches sozusagen einen Stamm bildet. An diesem sind in regelmäßigen Abständen Gold Nanopartikel befestigt, die somit die Helix bilden. Für meine Arbeit habe ich zwei verschiedene Versionen davon konstruiert. Die eine mit einem langen Stamm, an dem bis zu 7 Goldpartikel mit 40 nm Durchmesser befestigt werden können (Abbildung 1.4a) und die andere mit einem deutlichen kürzeren, jedoch dickeren Stamm, and dem 6 Partikel mit 20 nm Durchmesser befestigt werden können (Abbildung 1.4b). Die optischen Eigenschaften von beiden Helices mit verschiedenen Anzahlen von Goldpartikeln wurden gemessen. Dabei konnte gezeigt werden, dass die Signale der beiden Helices sich stark unterscheiden, weil durch ihre verschiedenen Formen die Abstände der Partikel zueinander verschieden sind und die plasmonischen Schwingungen demnach ungleich stark zwischen den Partikeln übertragen werden.

Die andere chirale Struktur besteht aus einem DNA-Origami welches zwei längliche Goldstäbchen in einem 90° Winkel zueinander positioniert. Diese so genannten Nanorods mit einer Länge von 54 nm und einen Durchmesser von 22 nm wurden so angeordnet, dass sie übereinander betrachtet, ein L ergeben, wie in Abbildung 1.4c gezeigt. Diese Struktur ist bereits chiral. Ich konnte jedoch zeigen, dass ein zusätzliches, kugelförmiges 38 nm Nanopartikel zwischen den Nanorods als plasmonische Brücke fungiert und das chirale Signal somit verstärken kann. Des Weiteren konnte ein zusätzliches Signal beobachtet werden, welches beweist, dass diese Position innerhalb einer chiralen Struktur auch chirale plasmonische Schwingungen innerhalb des sphärischen Partikels ausgelöst hat, obwohl dieses Partikel keine chirale Geometrie vorweisen kann.

Dies sind zwei Beispiele, wie DNA-Nanotechnologie benutzt werden kann um Strukturen auf der Nanoebene zu erforschen, wodurch wir ihrer Eigenschaften besser verstehen können. Mit diesem Wissen können eines Tages vielleicht komplett neue Materialien erschaffen werden mit speziellen optischen Eigenschaften, die wir zu diesem Zeitpunkt so noch gar nicht kennen. All dies und vieles mehr gehört zu den Geheimnissen, die die Nanowelt für uns bereithält.

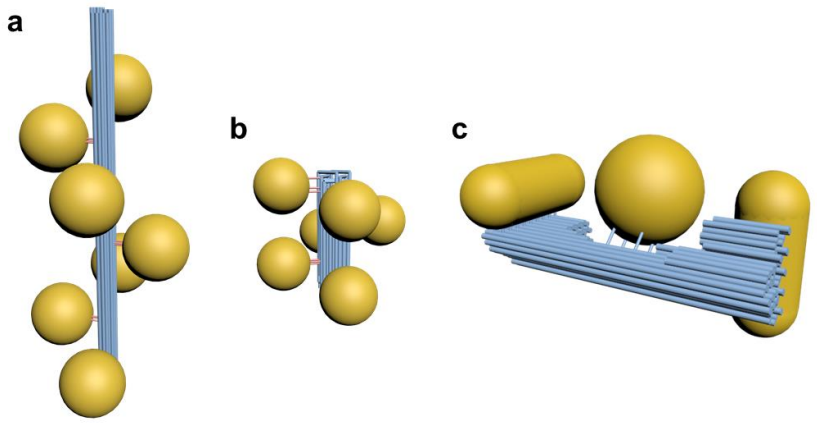

Abbildung 1.4: 3D-Modelle einer **a**) länglichen Goldhelix **b**) flachen Goldhelix und **c**) einer Struktur mit Nanorods und einem plasmonischen Brückenpartikel. Die blauen Zylinder repräsentieren DNA-Doppelhelices und die geldblichen Elemente Goldpartikel.

Chapter 2

DNA Nanotechnology

2.1 DNA

The deoxyribonucleic acid, or DNA, carries the genome of every living being. It encodes the blueprint for the entire biological organism and the genetic information that gets passed on to the next generation. Apart from this function, however, it was discovered that DNA could be used in an entirely different manner: as a building material. Before one can understand the meaning of this and the numerous possibilities it reveals, one must study the DNA first.

In the year 1869, Friedrich Miescher of the University of Tübingen, isolated phosphate-rich chemicals from the nuclei of white blood cells [4]. He called his discovery nuclein, later referred to as nucleic acids. Although the significance of this discovery was not immediately apparent, he already proposed a connection between these molecules and heredity [5]. The chemical composition of nucleic acids was later determined by Albrecht Kossel. One by one, he extracted 4 different bases, which he called nucleic bases [6]. He was awarded the Nobel Prize for Physiology or Medicine in 1910 for his work. However, the chemical structure of nucleic acids remained unknown for several more decades, even though numerous scientists were working towards it. The breakthrough came through x-ray crystallography and the work of Maurice Wilkins and Rosalind Franklin at the King's College London. Wilkins and his graduate student Raymond Gosling had already obtained the first diffraction picture of DNA [7] before Franklin took over the project and refined the setup to obtain the famous photo 51, depicted in figure 2.1a [8]. This photo was critical evidence in identifying the structure of DNA and was used by James Watson and Francis Crick to develop the chemical model of the DNA molecule, shown in figure 2.1b [9]. Wilkins, Franklin and Watson, and Crick all published their work in 3 separate papers in the same issue of nature in 1953 [8-10]. Wilkins, Watson and Crick

were awarded the Nobel Prize of Physiology or Medicine in 1962; Franklin had died 4 years earlier.

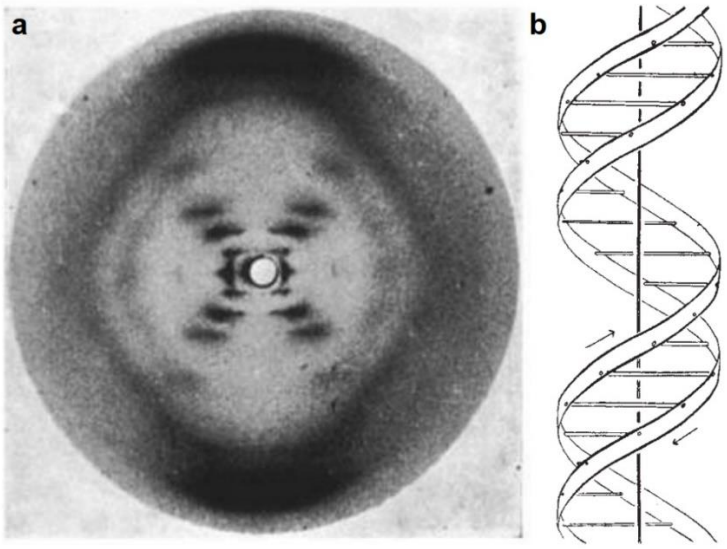

Figure 2.1: **a**) X-ray diffraction image of a paracrystalline gel composed of DNA fiber, taken by Rosalind Franklin and her graduate student Raymond Gosling. Originally published in nature, 1953. **b**) Illustration of the double helix as published in 1953. The ribbons symbolize the two phosphate-sugar chains and the horizontal rods the base pairs. The vertical line marks the fiber axis. Reprinted from [8] and [9], with permission from Springer Nature.

Located in the cell's nucleus, the DNA is an elongated molecule, consisting of a long chain of so-called nucleotides, which in turn are made of the sugar deoxyribose, phosphate, and one of four nucleobases, as can be seen in figure 2.2. The hydrophilic phosphate, which gives the DNA a negative charge in solution, forms the backbone together with the deoxyribose. The nucleobases are guanine, cytosine, adenine, and thymine, usually abbreviated with their first letter: G, C, A, and T. These abbreviations are also used for the nucleotides, since they only differ by their bases. The sequence of these nucleotides defines the genetic code. Two of the bases are purines (G and A), while the other two and pyrimidines (C, T). Each of these bases can only bond to one of the other bases. G and C can bond via three hydrogen bonds, while A and T can bond via two hydrogen bonds. A single-stranded DNA molecule can therefore bond to another, forming the DNA double helix. The double helix is not only stabilized by the hydrogen bonds between the bases but even more dominantly by a stacking force between the base pairs along the helix axis.

To form a double helix, the single strands need to be in opposite direction to each other. The direction of a single DNA strand is defined by the deoxyribose ring, which is composed of an oxygen atom and 5 carbon atoms, which are numbered from 1' to 5'. The 1' binds to the base, while the 3' is connected to an OH-group that can bind to the phosphate of the next nucleotide and the 5' binds to the phosphate. A DNA double helix, therefore, always connects a DNA strand going from 5' to 3' to a DNA strand going from 3' to 5'. The strands are located around each other in a helix shape, mainly stabilized by the stacking interaction between consecutive bases and not as much by the hydrogen bonds between the bases as formerly presumed. The DNA double helix specifics can vary between different configurations, the A-, B-, and Z-DNA. The B-DNA is the most common under the conditions found in cells and has a pitch of 3.4 nm, which means 10.5 base pairs (bp) per turn. This double helix forms a minor groove of 1.2 nm as well as a major groove of 2.2 nm, which represent the main binding points for other molecules. The diameter is between 2.2 nm to 2.6 nm, depending on the solution. The length of a nucleotide amounts to 0.33 nm. The hybridization into a double helix also drastically changes the bending stiffness of the DNA molecule. A single DNA strand has a persistence length of around 4 nm [11], while a DNA double helix has a persistence length of around 45 nm [12].

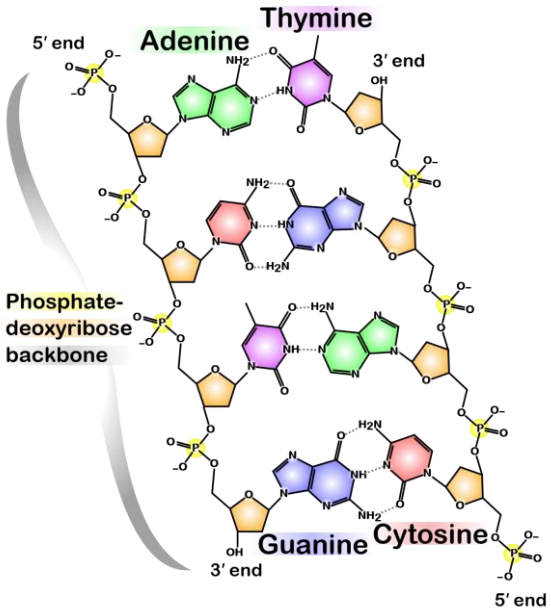

Figure 2.2: Chemical structure of DNA double helix, dotted lines represent hydrogen bonds. Illustration by Madprime, distributed under CC BY-SA 3.0 at [1].

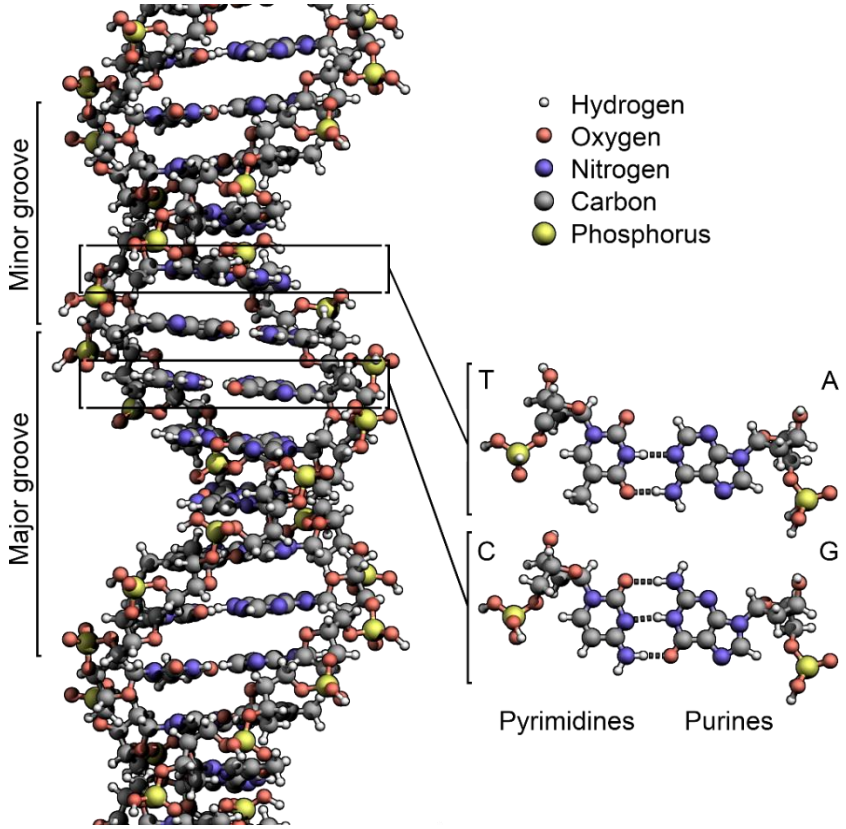

Figure 2.3: Chemical structure of the DNA double helix with detailed structure of two base pairs. Illustration by Zephyris, distributed under CC BY-SA 3.0 at [1].

2.2 Early DNA Nanotechnology

The journey towards DNA nanotechnology started in 1964 with the molecular biologist Robin Holliday. In his work, he discovered an alternative form of DNA hybridization that occurs during gene-conversion events in the meiosis of cells [13]. The model he proposed was named after him, Holliday Junction, and would later be an important cornerstone for a completely new field of research. A Holliday junction is made of at least 3 DNA strands that hybridize with each other. If a standard DNA double helix is a two-way street, a Holliday junction is the intersection.

The concept of using Holliday Junctions to give DNA a different purpose than information storage is based on a simple idea: If short DNA strands, so-called oligonucleotides, carry a base sequence of which a portion is complementary to the bases of another oligonucleotide, the base-pairing rules will make sure that these portions will hybridize, leaving the rest of the oligonucleotide free to hybridize with the next oligonucleotides, therefore enabling them to assemble into any kind of 3D nanostructure. This was first

proposed in 1982 by Ned Seeman [14]. Inspired by the M. C. Escher woodcut “Depth”, he imagined not only different synthetic junctions but 2- or 3-dimensional DNA lattices. As a crystallographer, he wanted to use these lattices to align other target molecules for crystallographic studies. The first experiments were published in the following year [15], but it would take until 1991 before the first 3D nanoscale object, a DNA cube could be synthesized by using 8 Holliday Junctions as edges and connecting them with complementary base sequences [16]. Seeman went on to synthesize Borromean rings [17] and the first DNA nanomachine, which uses different buffers to trigger the transition between B-DNA and Z-DNA, which changes the structure and therefore the distance between 2 attached fluorescent molecules [18]. This distance has an effect on the fluorescence resonance energy transfer (FRET) between the molecules, which is easily detectable and was therefore used as proof for the transition. For all these structures, one needs DNA oligonucleotides with specifically defined base sequences. The feasibility and cost of DNA nanotechnology, therefore, largely depended on progress in the field of DNA synthesis, which luckily provided increasingly faster and cheaper access to oligonucleotides.

Several different approaches towards functionality have been studied in the following years. One way that has already been discussed is using different buffer conditions as a trigger. Gueron and collaborators discovered in 1993 that in acidic conditions, DNA could hybridize in an entirely different confirmation, which they called i-motif [19]. Due to an additional hydrogen ion, cytosine bases can bind to each other, oligonucleotides with sufficient C-bases can therefore hybridize without having complementary sequences. I-motifs can even consist of 3 or 4 strands binding to each other in different variations. If the pH is increased, the DNA strands switch to B-DNA conformation and can therefore act as a DNA nanomachine [20].

Another possibility to achieve controllable motion was published by Neumann and collaborators in 2000. Here DNA was used as a fuel to open and close a DNA structure shaped like a pair of tweezers [21]. As shown in figure 2.5, the DNA tweezer in the open state has sections of single-stranded DNA on each side, which can be brought together by a fuel strand F with complementary sections to both sides. The fuel strand furthermore has a section that is not complementary to any part of the tweezer, the so-called toehold, which is crucial for the opening mechanism. If the complementary fuel strand $\bar{F}$ is added,

it starts to hybridize on the toehold section, triggering a chain reaction all the way through until it hybridized completely with the fuel strand F. This double helix of F and $\bar{F}$ is now a waste product of the mechanism, the structure itself remains the same. This process is called strand displacement and was later used in copious DNA machines.

Another step forward was the manipulation of precious metals with DNA nanotechnology, as published by Schultz and collaborators in 1996 [22]. In this work DNA was used to assemble gold nanocrystals into spatially defined structures. Since top-down methods (breaking down of a system into smaller parts) for obtaining crystals only reach the upper end of the nanometer regime, this bottom-up method (assembling a system from smaller parts) opened new possibilities for the construction of metallic nanostructures. For this, gold nanoparticles were attached to the end of DNA oligonucleotides using thiol-modifications, which would later become a standard approach in DNA nanotechnology. The resulting oligonucleotide-Au conjugates could then be assembled into dimer or trimer assemblies through the addition of complementary DNA templates, making them the first gold nanoparticle assemblies with DNA.

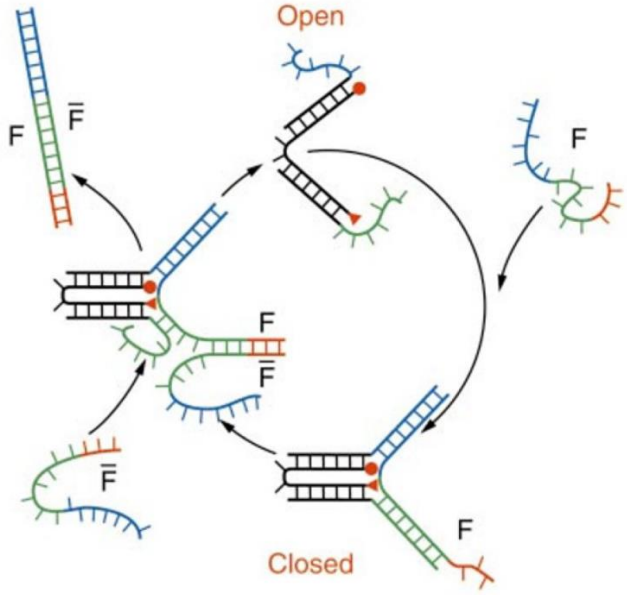

Figure 2.4: DNA tweezer with DNA-fueled opening and closing mechanism. Fuel strand F hybridizes to structure to close the tweezer, fuel strand $\bar{F}$ hybridizes to F via strand displacement, starting with the toehold section in orange, opening the tweezers. Reprinted from [21, 112], with permission from Springer Nature.

Ned Seeman and his coworkers continued the work on DNA nanotechnology and developed 2-dimensional assemblies of DNA oligonucleotides in 1998 that they called DNA crystals [23]. This was accomplished by using a tile structure of either 2 or 4 different tiles, consisting of 4 or 5 DNA oligonucleotides, each selectively bound to 4 tiles around them, using base pairing. Through the self-assembly of these tiles, large crystals of several micrometers in length could be synthesized and observed by atomic force microscopy. A further step towards more complex large structures was taken by LaBean and collaborators in 2003 [24]. Their work is based on DNA tiles in the shape of a four-armed junction containing 9 oligonucleotides. These 4 × 4 tiles can self-assemble to nanoribbons, if assembled parallel, so that all tiles face the same direction, or 2D nanogrids, if assembled antiparallel, were adjacent tiles face in different directions. The tiles can also incorporate a biotin-group at their center, to which streptavidin can bind, forming a protein nanoarray on DNA lattice. They furthermore showed that the DNA arrays could even be metalized by using a two-step procedure to form highly conductive nanowires with lengths of up to 5 μm.

The approach of constructing large structures through tiles was brought even further in 2012 when Yin and collaborators showed that even 2-dimensional structures with arbitrary shapes could be obtained this way [25]. This was made possible by using 362 distinct DNA tiles, each consisting of only a single oligonucleotide. All of them together would form a flat square, representing a molecular canvas, where each DNA tile is one pixel. Since every DNA tile is unique, it can either be included in the assembly process or left out. This control over each pixel made it possible to draw anything from letters to symbols with DNA. The technique is analogously applicable in 3 dimensions, where tiles become bricks, and the canvas is now a block made of 10 by 10 by 10 bricks [26].

2.3 DNA Origami

The year 2006 marked an essential step in the field of DNA nanotechnology, as Paul Rothemund from the University of Southern California, Caltech, developed the DNA origami [27]. Years before complex structures could be assembled through the DNA tile approach, he was able to assemble any arbitrary structure using a long circular DNA single-strand, which he called scaffold strand, and combined it with a multitude of shorter

DNA oligonucleotides, called staple strands. These staple strands were designed to not only hybridize to the scaffold strand in one place but in several sections, therefore folding the scaffold strand into any desired 2-dimensional structure, as visualized in figure 2.5. To prove this, he folded the DNA into several different flat shapes, for example, a star or a circle with 3 holes, representing a smiley face. He used the genome of the bacteriophage M13mp18 as a scaffold, which had been sequenced in its entirety, making it possible to design staple strands with the correct sequences to achieve the folding. Once the staple strands were synthesized, they only had to be placed in buffer together with the scaffold strand, heated to break up all unspecific base pairings, and then slowly cooled down to let every oligonucleotide find its place in the DNA origami. This method made it easy to construct complex DNA structures with many possible shapes and addressable sites.

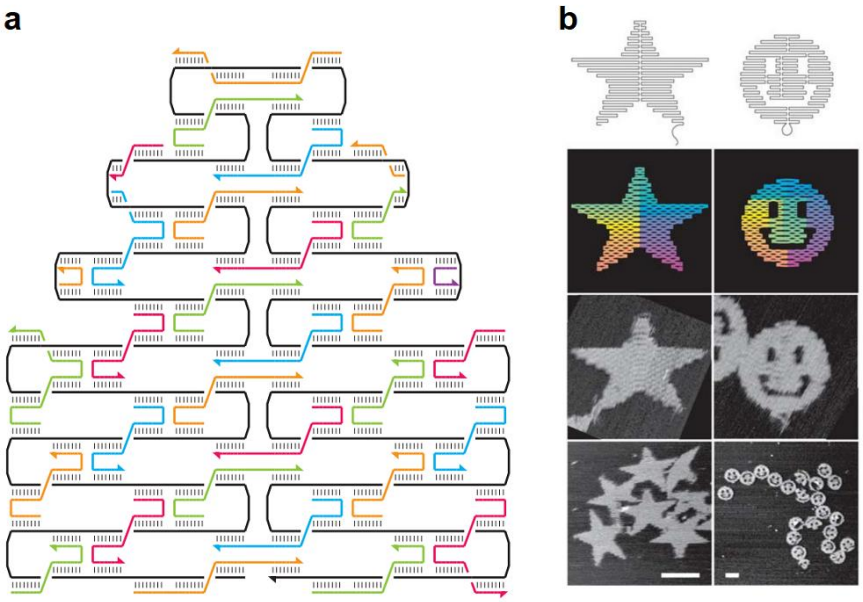

Figure 2.5: **a**) Schematic structure of a DNA origami with the scaffold strand in black and staple strands in various colors **b**) DNA origami in the shape of a star and a smiley face, displayed schematically with their folding paths (first row), as diagrams with the scaffold going from red to purple (second row) and in atomic force micrographs (third and fourth row). Scale bar: 100 nm. Reprinted from [27], with permission from Springer Nature.

The first 3-dimensional DNA origamis were subsequently developed at Harvard University and published by Douglas et al. in 2009 [3]. Based on the same principle as a 2-dimensional DNA origami, staple strands now also connect between different layers, as

shown in figure 2.6. The design makes sure that the scaffold strand in neighboring double helices always runs antiparallel, which is a requirement for DNA origami. Due to the pitch of the B-DNA, it takes 21 base pairs (bp) for the double helix to complete 2 turns. Because of this, it makes sense to arrange double helices in a honeycomb lattice, where the angles between the connections of nearest neighbors are either 0°, 120°, or 240°, because a staple crossing after 7 bp will amount to 240°, a crossover after 14 bp to 480° (120°) and a crossover after 21 bp to 720° (0°). If built in this fashion, no stress is applied between the helices, and the helix bundles can run in a straight direction. However, one can design twisted helix bundles by installing crossovers after any different number of bp, as shown by Shih and collaborators [28]. These modifications are called bp deletions, if less than 7 bp, or bp insertions if there are more than 7 bp between crossovers. They induce stress, that is either pulling or pushing the helices, respectively. If combined, one can even design a helix bundle with a curvature, which can ultimately lead to DNA origami shapes such as rings, spirals, or other designs with curves.

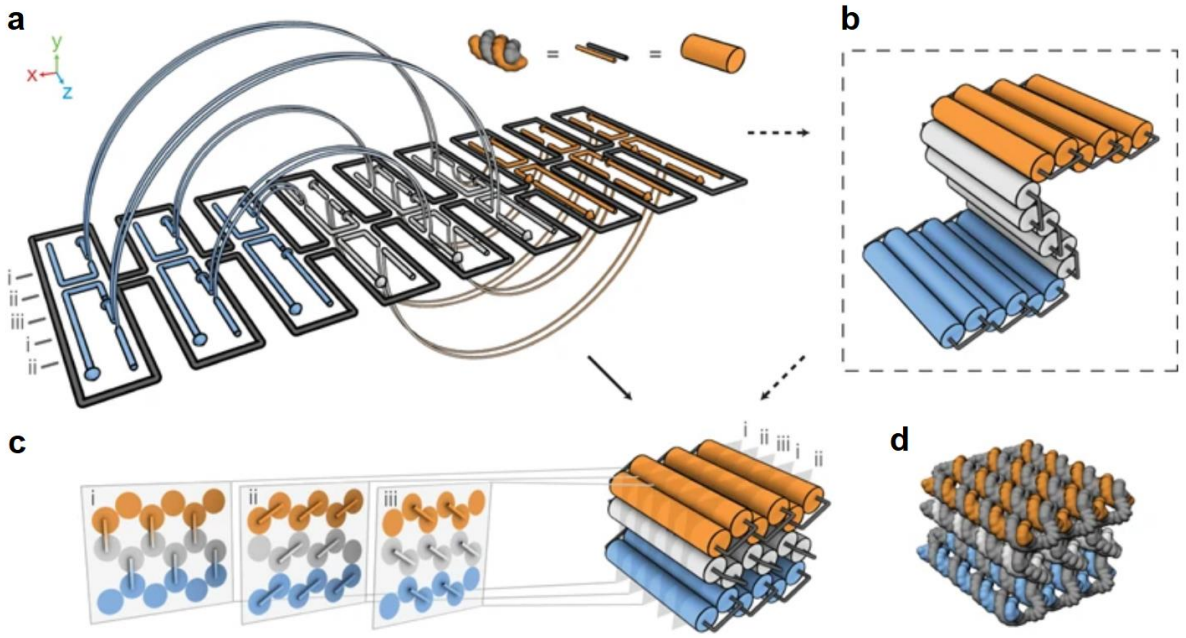

Figure 2.6: Schematic design of a 3-dimensional DNA origami with scaffold strand in grey and staple strands in orange, grey, and blue, as well as cylinders representing DNA double helices. Shown as **a**) visualization in 2 dimensions with crossovers between different layers depicted as loops, **b**) half-folded conceptual intermediate of DNA origami with unpaired scaffold loops connecting the ends of neighboring helices, **c**) cross-sections of honeycomb lattice with staple crossovers after 7, 14, and 21 bases and **d**) atomistic DNA model. Reprinted from [3], with permission from Springer Nature.

3-dimensional DNA origamis with a square lattice are also possible. However, since the number of bases between 90° angles can only be approximated, they naturally carry a twist that has to be released through periodical deletions or insertions. A different approach of expanding DNA origami sheets into 3 dimensions has been shown in the same year by Andersen et al [29]. Here, a DNA origami box was constructed by connecting 6 DNA sheets with each other. Furthermore, one of these sheets acts as a lit, which can be opened through the addition of an oligonucleotide, which acts like a key by disconnecting the lit from the box through strand displacement. Fluorophores were attached to the lit and the opposite edge of the box so that the opening and closing could be detected by FRET measurements.

Another interesting possibility to construct a DNA origami is through the use of tensegrity. Tensegrity is a structural principle that describes a system stabilized through continuous tension and integrity. This way, the structure can show high resilience and strength at low weight. This was first implemented in DNA nanotechnology in 2003 by Mao and collaborators [30]. The 2-dimensional structure consisted of 3 interconnected double helices and could also be assembled as chains and 2D arrays. The first use of tensegrity in DNA origami was published in 2010 by Liedl et al [31]. This work is based on the different rigidities that can be obtained with DNA. As mentioned, a single-stranded DNA is more flexible than a double helix. However, a helix bundle (HB) is even more rigid and becomes more stable the thicker it is designed. For a tensegrity structure, 3 bundles of 13 helices (13HB) were used, only connected by single-stranded DNA, that applies pressure on the rigid 13HB, similar to a tensegrity structure of string and wood, shown in figure 2.7. If a similar structure is built with 6HB, the tension of the single strands can visibly bend the DNA origami, as was shown in a seperate experiment in which the applied forces could also be calculated.

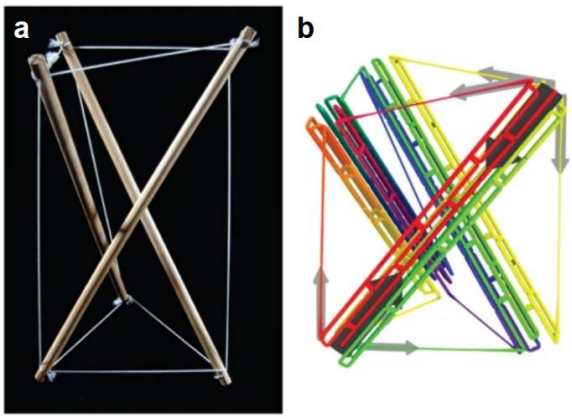

Figure 2.7: **a**) Tensegrity structure made of wood and strings and **b**) conceptual illustration of a tensegrity structure made of DNA, where 13-helix bundles act as the rigid struts and single-stranded DNA as the flexible strings exerting contractile forces, as indicated by grey arrows. Reprinted from [31], with permission from Springer Nature.

The process of constructing new DNA origami structures was radically simplified through the introduction of the design software caDNAno [32]. Its graphical user interface helps to define the correct scaffold path, crossover positions, and breaks between staples. After designing, one only needs to set the scaffold sequence, and a list of all required staple strands can be obtained. Additionally, Kim et al. developed the computational tool CanDo, which can predict the structure as well as the mechanical flexibility of a DNA origami from its caDNAno file [33, 34].

2.4 Applications

Many possible applications for DNA nanotechnology and especially DNA origami have been studied in recent years. A part of this research is concentrated on the DNA origami itself and on advanced designing possibilities, for example, the work of Dietz and collaborators. They showed that complementary base pairs are not necessarily needed to multimerize different DNA origamis with each other [35]. Since base stacking represents a stronger force within the DNA double helix in comparison to base-base pairing, so-called blunt ends are enough to multimerize structures if their shape is complementary to each other. Blunt ends describe DNA helices where both sides terminate together without leaving any unpaired bases. This was used to form more complex DNA origamis, such as switchable gears and nanorobots. Using this, they were able to design wedge-

shaped DNA origamis that can multimerize into rings, tubes, and spheres, which have masses of up to 1.2 gigadalton with precisely controllable sizes and shapes [36]. Furthermore, the group developed a mass production procedure, which allows the production of macroscopic amounts of DNA origami in specialized bioreactors [37]. A different approach to giant DNA origami formations is to design a DNA origami unit cell that can multimerize on six sides and grow into a DNA origami crystal, as shown in the work of Liedl and collaborators [38]. For this, a tensegrity triangle was designed, which multimerizes into a 3-dimensional lattice that consists of 90% empty space. In this way, it leaves enough space within the crystal to incorporate guest molecules, which was shown with gold particles of 20 nm diameter. This marks a step towards Ned Seeman's original idea of using DNA lattices to orient molecules for crystallographic studies.

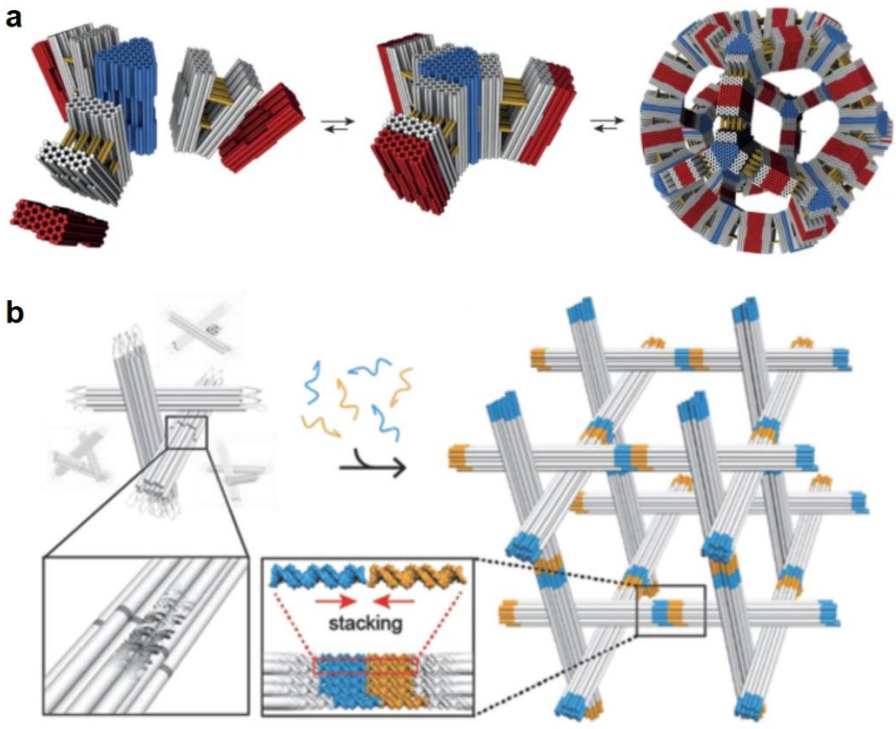

Figure 2.8: **a**) Schematic illustration of a DNA origami modules hybridizing through the use of blunt ends into a 1.2 GDa structure and **b**) tensegrity triangle multimerizing into a rhombohedral 3D lattice. Reprinted from [36] and [38], with permission from Springer Nature and John Wiley and Sons.

Since DNA is a biomolecule, it seems obvious to try to design a DNA nanostructure that can interact with biological systems. For example, DNA origamis can be designed to

function as immunostimulants, which was tested by Schüller et al. in 2011 [39]. In this work, DNA origami tubes are coated with multiple cytosine-phosphate-guanine sequences around the structure, which can trigger an immune response in spleen cells. This was proof that DNA origami can be used as a non-toxic and effective delivery system within cells. Advances such as these paved the way for DNA nanotechnology applications in medicine, where DNA origamis were tested as carrier systems for drug delivery, in particular the cancer medicine doxorubicin. Due to their low solubility and cytotoxicity, cancer drugs can be harmful and ineffective. DNA origami represents a suitable candidate for a carrier molecule that can deliver the drug to specific target cells and circumvent cellular drug resistance. Among many different approaches, Jiang et al. have designed a tube as well as a flat triangle, intercalated with doxorubicin, to release the drug in vitro in human breast cancer cells [40]. Similar to this, Högberg and collaborators have published a twisted DNA origami tube and shown that the release rate of the drug depends on the tension caused by the twist of the helix bundles within the structure and is therefore fully tunable [41]. Soon after this, the triangle design was tested by Zhang et al. *in vivo* on mice bearing breast tumors [42].

The feasibility of such applications depends largely on the stability of DNA nanostructures in biological systems. Although DNA origami structures are stable for 12 hours in cell lysate [43], in vitro tissue cultures can inherit several factors that can cause denaturation in DNA origami, most prominently, low magnesium concentrations [44]. Because of this, different approaches to protecting DNA nanostructures have been tested. One possible method is the encapsulation in a protective membrane, as shown by Shih and coworkers in 2014 [45]. Inspired by viruses, a lipid bilayer was formed around a DNA origami in the shape of an octahedron. The structure was subsequently released into the bloodstream of a mouse, where it showed significantly higher stability in comparison to the unencapsulated structure. To strengthen a DNA origami even further, silica encapsulation was recently found to be a promising possibility. A silica shell around a DNA origami bestows the structure with a powerful protection in terms of chemical resistance, structural integrity, and heat sensitivity. Paunescu et al. first published a protocol describing the encapsulation of DNA into amorphous silica using sol-gel chemistry in 2013 [46]. The concept was inspired by biomineralization, which can protect DNA for millennia in fossils. This technique was first applied to DNA origami in 2018 by Fan and collaborators [47]. Their work shows a variety of 2-dimensional and 3-

dimensional DNA origami designs coated with a silica layer on a surface, which increased their size and Young's modulus. Heuer-Jungemann and collaborators applied this approach to DNA origamis in solution and large DNA crystals [48]. Furthermore, they provided proof that these silica-coated DNA origamis could withstand temperatures of up to 100° C.

An especially interesting feature of DNA origami is its molecular functionality. The field of nanorobotics leads to countless possibilities of nanostructures carrying out tasks in biological systems or elsewhere. Douglas et al. published a transport system where molecules can be loaded inside a DNA origami and released by a logic gate [49]. This nanorobot in the shape of a hexagonal tube consists of two halves, connected by a scaffold hinge on one side and two aptamer lock mechanisms on the other. These aptamers are short DNA strands that can hybridize with a complementary strand to keep the structure closed. However, if an antigen binds through protein displacement, the structure opens and releases the cargo, which is attached to the inside of the structure, as shown in figure 2.9. Although many different cargos are possible, the system was tested with gold nanoparticles and fluorescently labeled antibody fragments that bind to cells expressing a specific antigen. Another DNA robot was developed by Qian and collaborators [50]. This work shows a nanomachine that can sort molecular cargos. The single-stranded DNA robots consists of a foot domain, with which it can perform random walks on a DNA origami platform, and arm domain that allows it to grab and deliver cargo. Another fundamental advancement in this field was shown by Kopperger et al. in 2018 [51]. Here, a 55x55 nm DNA origami platform was designed with a free rotatable robotic arm that can be extended from 25 nm to 400 nm. This machine was used to study DNA duplex and precisely move nano-objects over tens of nanometers. This was not realized with slow working strand displacement but external electric fields, allowing the arm to switch positions within milliseconds, as was proven by FRET experiments.

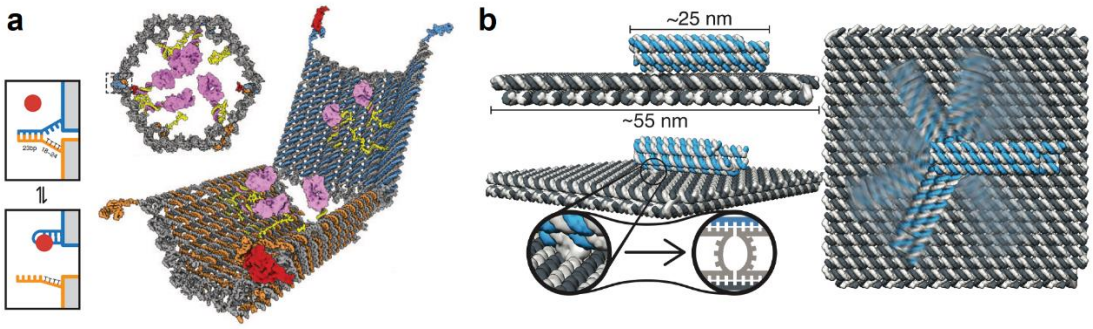

Figure 2.9: **a**) Schematic illustration of a nanorobot that can release its cargo (pink) using two lock systems, which can be opened with a key molecule and **b**) a DNA origami platform with a rotatable robotic arm that can move nano objects. Reprinted from [49] and [51], with permission from AAAS.

A field that is especially relevant for this thesis is the exploration of optical effects in the nano-regime through the use of DNA origami. Since Mirkin and collaborators have published a protocol for an effective functionalization of nanoparticles with DNA oligonucleotides [52], DNA nanotechnology became a viable tool for designing metal nanostructure assemblies in a bottom-up approach, which can surpass the limitations of top-down approaches such as lithography. The first attachment of gold nanoparticles to a DNA origami was realized by Ding et al. in 2010 [53]. They demonstrated that nanoparticles of sizes 5, 10, and 15 nm could be placed on a triangular DNA origami platform on precise locations with less than 10 nm spacing between them. This is of particular importance because metal nanoparticles in such proximities to each other show an unusual optical effect called plasmon coupling, which leads to a blue shift in their absorbance spectrum. More details on plasmonics will be offered in the next chapter. Kuyzk et al. expanded on this design by synthesizing a 24-helix bundle DNA origami with gold nanoparticles attached in a more sophisticated arrangement, a helix [54]. As shown in figure 2.10a, the 9 nanoparticles of each 10 nm diameter can be arranged in a left-handed or right-handed chirality around the DNA. With this, they were able to prove that chiral nanostructures made of metal express circular dichroism, meaning they absorb left-handed and right-handed polarized light differently, which has only been predicted by theory before this [55]. Following this, they were also able to align the gold helices either parallel or perpendicular to the direction of the light beam [56]. These alignments resulted in different circular dichroism spectra, which they could switch back and forth, giving further insights into the circular dichroism spectra of such nanostructures. Soon

afterwards a more effective approach for a nanostructure with a switchable circular dichroism signal was shown by Kuyzk et al [57]. This design uses 2 elongated gold nanorods attached to 2 DNA origami bundles, which are only connected in their center and can therefore rotate in relation to each other, as seen in figure 2.10b. The circular dichroism signal of this structure depends on the relative angle between the nanorods and, therefore, the angle between the 2 helix bundles, which can be controlled by 2 lock systems that can be opened and closed by toehold-mediated strand displacement reactions. The switch is therefore triggered by a specific nucleic acid sequence, for example, an RNA sequence from the genome of the hepatitis C virus, making the structure a sensing device, as published by Funck et al. in 2018 [58]. Through the change in circular dichroism, a concentration of only 100 pM of RNA sequence could be detected. Nguyen et al. recently showed that the signal output of such a sensing device could be drastically increased through the use of silver-coated gold nanorods, which can easily be synthesized using a new protocol provided in their work [59].

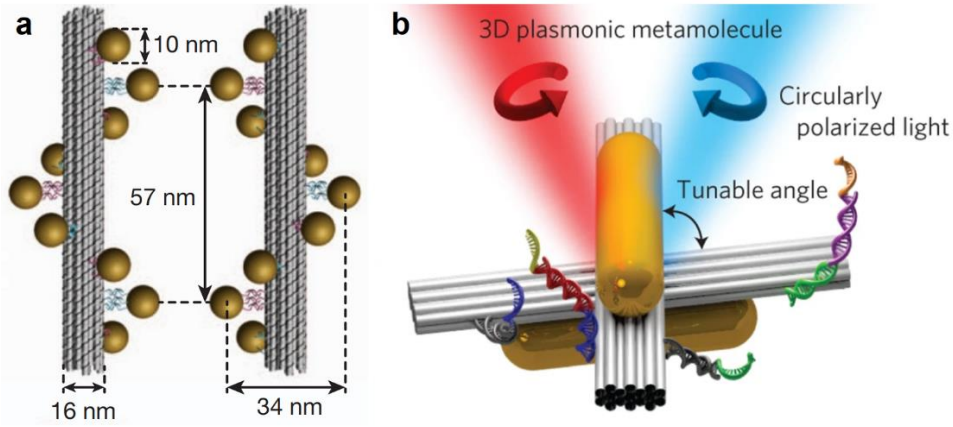

Figure 2.10: **a**) Schematic illustration of a left-handed and right-handed gold nanohelix consisting of 10 nm nanoparticles around a 24-helix bundle DNA origami and **b**) gold nanorods on DNA origami with rotatable elements and lock mechanisms to switch plasmonic chirality. Reprinted from [54] and [57], with permission from Springer Nature.

Chapter 3

Plasmonics

3.1 The Drude Model

In the field of classical electrodynamics, an electromagnetic wave describes a synchronized oscillation of an electric field and a magnetic field with oscillation planes perpendicular to each other as well as to the propagation direction. It can be characterized by either its frequency, which gives the number of oscillations per second, or its wavelength, which gives the distance between oscillations. The wavelength can be derived from the propagation speed of the wave, which is the speed of light divided by its frequency. The behavior of electromagnetic waves is determined by the Maxwell equations, derived by James Clerk Maxwell in 1861.

$$\vec{\nabla} \cdot \vec{E} = \frac{\rho}{\epsilon_0}$$

$$\vec{\nabla} \cdot \vec{B} = 0$$

$$\vec{\nabla} \times \vec{E} = -\frac{\partial \vec{B}}{\partial t}$$

$$\vec{\nabla} \times \vec{B} = \mu_0(\vec{J} + \epsilon_0 \frac{\partial \vec{E}}{\partial t})$$

in these equations, $\vec{E}$ is the electric field, $\vec{B}$ is the magnetic field, $\vec{\nabla}$ is the 3-dimensional gradient operator, also called del or nabla, ρ is the electric charge density, ϵ_0 is the vacuum permittivity, μ_0 is the vacuum permeability, j is the electric current density, and t is time.

To solve Maxwell's equations, one can formulate a superposition of monochromatic waves. If we assume for an instantaneous response time of the medium to the wave, ϵ is

a constant in Maxwell's equations. If we account for the finite response time, however, ϵ becomes a function of the wavelength ω, which leads to the superposition solution. This approach gives a complete representation of optical responses of any material in the classical picture. In the case of metal nanoparticles, we have to find a model for the dielectric function to obtain a working model.

We use the Drude free-electron model, as this is a simple way to model the dielectric function in metals. In this model, all quantum mechanical effects are left out, and the electrons within the metal are regarded as free and non-interacting particles. This electron gas is allowed to freely move against a background of positive ions and can therefore be described with the following formula:

$$m\frac{d^2x}{dt^2} = -\frac{m\gamma dx}{dt} - qE_{tot}(t)$$

in this formula, m is the effective electron mass, q is the electron charge, γ is the frequency of collisions, which accounts for electron scattering, and $E_{tot}(t)$ is the total electric field, this includes the external field as well as internal fields, which are generated by electron motion. Using this model, the resulting dielectric function is [60]

$$\epsilon(\omega) = 1 - \frac{\omega_p^2}{\omega^2 + i\gamma\omega}$$

where ω_p is the plasma frequency of the free electron gas and i denotes the imaginary number. The dielectric function is therefore a complex function and can be divided into a real component and an imaginary one

$$\epsilon(\omega) = Re\big(\epsilon(\omega)\big) + i\, Im(\epsilon(\omega))$$

3.2 Nanoplasmonics

In this particular area of solid state physics, the optical phenomena of metal nanosystems can be described on the nanoscale. In this work, a brief description of the theory underlying nanosystems will be presented; a more detailed explanation can be found in

[61], [62], and [63]. The wavelength is the limiting factor for the concentration of electromagnetic energy. Even in ideal conditions, a Fabry-Perot resonator with perfect mirrors, it is still impossible to confine the light to a smaller length than $\lambda/2$ or analogous to a smaller volume than $\lambda 2/8$. If we want to achieve confinement of optical energy in the nanoscale, we have to abandon these two assumptions:

1. Optical energy is equivalent to electromagnetic energy
2. Ideal mirrors can achieve the best possible confinement

The depth to which an electric field can enter a substrate is called the skin depth l_s and is given by

$$l_s = \lambda_v \left[\left(\frac{-\epsilon_m^2}{\epsilon_m + \epsilon_d} \right)^{1/2} \right]^{-1}$$

λ_v denotes the reduced vacuum wavelength, which is given by $\lambda_v = \lambda/2\pi = \omega/c$. For precious metals such as gold and silver, the skin depth is roughly 25 nm. If we consider a nanosystem of length a with $a \leq l_s$ the electric field can penetrate the entire system and cause the electrons to oscillate. For this, we ignore retardation effects; this way, we can approximate the incident field to be constant. We call this the quasi-static approach. We now consider a spherical particle and solve the Maxwell equations. If we define an electric potential Φ, the electric field can be written as $E = -\nabla\Phi$. Considering a driving field in z-direction gives us $\Phi = -Ez = -Er\cos\Phi$. With this, the potential inside the particle can be formulated as

$$\Phi_{in}(r, \Phi) = \sum_{l=1}^{\infty} A_l r^l P_l(cos\Phi)$$

While the potential outside of the particle is

$$\Phi_{out}(r, \Phi) = \sum_{l=1}^{\infty} B_l r^{l+1} P_l(cos\Phi) - Er(cos\Phi)$$

With the boundary condition that the potential must be continuous at r=a:

$$l = 0: A_0 = B_0 = 0$$

$$l = 1: A_1 = \frac{-3\epsilon_{out}E}{\epsilon_{in} + 2\epsilon_{out}}, B_1 = \frac{(\epsilon_{in} - \epsilon_{out})Ea^3}{\epsilon_{in} - 2\epsilon_{out}}$$

$$l > 1: -\frac{\epsilon_{out}(l+1)}{\epsilon_{in}l} = 1, A_l = \frac{B_l}{a^{2l+1}}$$

In the case that there is no constant term (l = 0), there is also no net charge. For l = 1, one can obtain a response for every frequency. In the case of l > 1, the response is independent of E, meaning that higher modes cannot be excited by a constant field [62]. Since the potential of the particle dipole is

$$\Phi = \frac{\mu z}{\epsilon_{out} r^3}$$

where μ is the dipole moment, the polarizability of the particle is

$$Re(\epsilon(\omega)) = -2\epsilon_{out}$$

which is called the Fröhlich condition, named after German-born British physicist Herbert Fröhlich. The related mode is the dipole surface plasmon of the particle, which emphasizes how important the dielectric environment is to the resonance frequency. It shows that an increase of ϵ_{out} causes a redshift of the resonance, which is very useful for optically sensing small changes in the particle environment [63].

To measure the particles' interaction with light, the absorption and scattering cross-section has to be used. This cross-section can be derived from the absorbed or scattered light energy by dividing it by the incident optical flux. Taking the polarizability into account, the expression for the cross-sections is

$$\delta_{abs} = \frac{4\pi k}{\epsilon_{out}} Im(\alpha) = 4\pi k a^3 Im\left[\frac{(\epsilon_{in} - \epsilon_{out})}{\epsilon_{in} + 2\epsilon_{out}}\right]$$

$$\delta_{scat} = \frac{8\pi\omega^4}{3c^4}|\alpha|^2 = \frac{8}{3}\pi k^4 a^6 |\frac{(\epsilon_{in} - \epsilon_{out})}{\epsilon_{in} + 2\epsilon_{out}}|^2$$

which shows the size dependencies of scattering and absorption. While the absorption cross-section scales with $a^3 = V$, the scattering cross-section scales with $a^6 = V^2$. This means, that absorption is stronger than scattering for small particles but scattering becomes more dominant with increasing particle size.

The quasi-static approach cannot be used for particles with radius $a > l_s$, because retardation effects have to be taken into account. In this case, we use the expansion of the first TM mode of Mie theory for the polarizability of a sphere, which leads to the expression:

$$\alpha_{sphere} = \frac{1 - \frac{1}{10}(\epsilon + \epsilon_m)x^2 + O(x^4)}{(\frac{1}{3} + \frac{\epsilon_m}{\epsilon - \epsilon_m}) - \frac{1}{30}(\epsilon + 10\epsilon_m)x^2 - i\frac{4\pi^2\epsilon_m^{3/2}V}{3\lambda_0^3} + O(x^4)}V$$

$$with\ x = \frac{\pi a}{\lambda_0}$$

Several additional terms account for physical differences in bigger particles [64]. The quadratic term in the numerator shows retardation effects, which lead to a shift of the plasmon resonance for particles with increasing volume, whereas the quadratic term in the denominator analogously accounts for retardation effects leading to a shift of the depolarization field inside the particle. In total, the size increase in gold particles leads to higher wavelengths, which is called redshift. Along with the particle volume the distance between the charges increases, therefore the restoring force lowers and the resonance frequency decreases. The imaginary term in the denominator accounts for radiation damping, which is caused by the decay of electron oscillations into photons. This represents the main contribution for weaker dipole resonances in the case of larger particle sizes. The intrinsic losses due to interband transitions are also accounted for in

the quadratic term in the denominator. This effect becomes more dominant as the particle sizes decrease to smaller than 5 nm.

The next step towards understanding plasmonics is to consider the case of several particles in close proximity. When two particles are close enough to each other that their plasmon resonances overlap spectrally, their resonances can couple to each other. This effect can enhance the electric field and even lead to new modes. This coupling is possible in the near-field as well as in the far-field. Far-field coupling occurs through scattered fields and takes place at distances longer than the optical wavelengths. In this work, only near-field coupling will be considered. If two particles are separated by a distance comparable to the evanescent field on the particle surface, one can observe Coulomb interaction of the surface charges. These interactions can create large, strong charge dipoles along the two particles. These lead to a strong enhancement of the local fields in the gap between the particles. The resulting field is now much stronger than the sum of the local fields of the individual particles. The closer the particles are together, the stronger the plasmon coupling. These high electric fields in the gap between the particles are called “hot spots” and provide strong coupling to a molecule located in the gap.

To use a simple model for plasmon coupling we consider each particle as a simple dipole. If we know use the plasmon-hybridization model [62] for two spheres, we obtain the following two solutions for the coupling modes:

$$\omega_{\pm} = \omega_1^2 \pm \frac{|U_{1m,1m}|}{2}$$

Here ω_1 is the dipole frequency, and U denotes the interaction energy. Its indices originate from the indices of the spherical harmonics Y_{lm}. Since we only consider l = 1, four different modes evolve. Hybridized longitudinal modes are represented by m = 0 and show two different solutions. One that corresponds to the dipoles being in phase, this is the lower frequency solution, and the other one with the dipoles out of phase, this is the higher frequency solution. As shown in figure 3.1, the plasmons that are coupled in phase can be excited by incident light and are therefore called bright mode. In contrast, the out-of-phase bonding or dark mode cannot be excited by light. The same goes for the corresponding transverse modes, where bright mode and dark mode also exist.

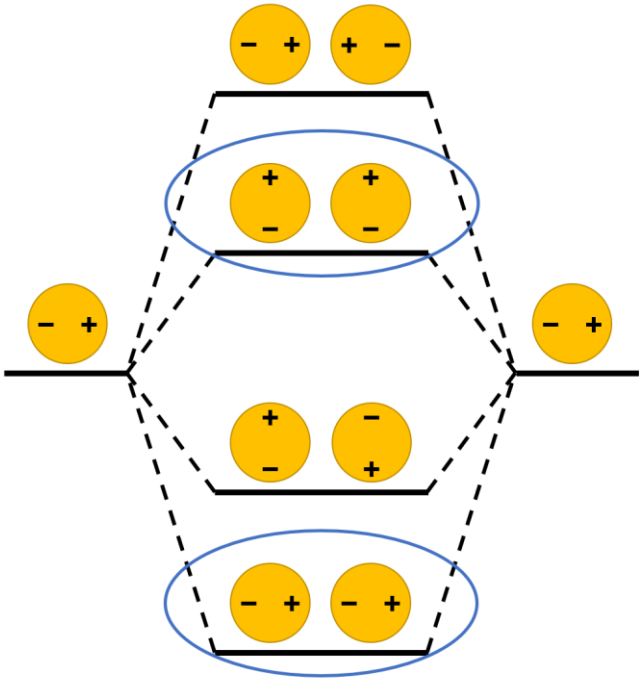

Figure 3.1: Graphic representation of the hybridization model for a quasi-static approximation of 2 plasmonic particles. The states highlighted by blue circles are the bright modes. They can be excited by an external electric field. The dark modes, in contrast, can only be excited under special requirements.

Bonding and antibonding modes do not couple if we are considering symmetric pairs of particles. If we consider two particles of different sizes, however, it is impossible for the two-particle dipoles to cancel each other out; therefore all hybridization modes are bright modes in this case. In reality, no dipole cancellation is ever perfect, even for symmetric particles. Dark modes can be excited by the Fano effect or other special ways like incident fields that rapidly vary in space, such as highly focused laser beams.

3.3 Plasmonic Circular Dichroism

Chirality plays a vital role in nature in various reactions and phenomena, including optical effects, as so-called optical active molecules can rotate the oscillation plane of incoming polarized light. Light is an electromagnetic wave combining an electric field and a magnetic field, which oscillates in planes orthogonal to each other. In two special cases, the light is called polarized. For linear polarized light, the oscillating plane rests in space. If the planes rotate, however, it is circularly polarized light. Depending on the rotational direction of the planes, we speak of right-handed polarized or left-handed polarized light,

respectively. If these different kinds of polarized light are absorbed differently, it is called circular dichroism (CD). If we want to measure the optical activity of a molecule, meaning how much incoming linear polarized light is rotated, we consider the optical rotational strength. Its formulation was first derived in 1928 by Léon Rosenfeld [65].

$$R = -Im(\mu^{if} \cdot m^{if})$$

In this expression, μ^{if} is the electrical and m^{if} the magnetic transition dipole moment from the initial (i) to the final (f) state. The Rosenfeld formula provides two main findings:

1. The rotational strength is directly depending on the geometrical structure because the charge density and, therefore, the transition moment depends on the structure.
2. Due to the scalar product, the rotational strength has a value as well as a sign. This means the value of R depends on the transition moments and the angle between them.

Because of these dependencies, CD spectroscopy has an extraordinary sensitivity to small changes in molecular structures [66]. The CD is measured by illuminating the sample with left-handed and right-handed circular polarized light of the same wavelength. The absorbed left-handed polarized light (A_L), as well as the absorbed right-handed polarized light (A_R), is detected, and their difference (ΔA) is determined. This CD value is measured for multiple wavelengths, which results in the CD spectrum, which characterizes the sample. CD can additionally be measured in ellipticity θ with the following conversion.

$$\theta = 32980 \cdot \Delta A = 32980 \cdot (A_L - A_R)$$

The prefactor $32980 = \frac{ln10}{4} \cdot \frac{180}{\pi}$ comes from a series expansion of the rotational strength around the term ΔT = 0. Instead of the ellipticity, sometimes the molar circular dichroism ϵ is used, which is given by:

$$\epsilon = \frac{\Delta A}{concentration \cdot optical\ pathlength}$$

To analyze a high number of randomly oriented molecules or microscopic objects, a high homogeneity is necessary to yield a non-zero CD signal. Biomolecules usually offer this homogeneity if they are of the same species and chirality; artificial nanostructures, however, have to be carefully designed and selected to achieve this. Coulomb interactions within chiral metallic nanoparticle assemblies lead to plasmonic CD. This has to be differentiated from the excitonic CD, as exhibited by chiral biomolecules for example.

A plasmonic CD signal of a nanostructure includes [67]:

1. CD effects of metal nanoclusters with chiral atomic structures, chiral molecules on the surface of nanoparticles, or chiral environments around a cluster
2. Coulomb interactions between chiral molecules and metal nanoparticles
3. Plasmon-plasmon interactions between non-chiral particles, which are arranged in a chiral geometry

The first point depends on a chiral atomic structure of the molecules. The other two points, however, rely on the concept of forming chiral optical active structures from building blocks, which can be chiral or non-chiral. While changing the atomic structure of molecules is difficult, chiral geometries can be formed with several methods, including lithography [68-71] or DNA nanotechnology [54, 57].

In this work, we focus on the possibilities of DNA nanotechnology for designing chiral nanostructures, which have the advantage of complete freedom for three-dimensional arrangement in comparison to lithography. While natural molecules typically express CD signals in the UV range, chiral metal nanostructures can be tuned to express a CD signal in the visual range, therefore opening the gate to novel materials with unique optical properties [72]. These CD spectra can be theoretically predicted with a model of interacting dipoles [73]. More details on this will be presented in chapter 6.

Chapter 4

Methods

4.1 Introduction to Microscopy

Microscopy is a crucial tool for gaining information when working with particles and molecules that are too small to be visible to the naked eye. Since this work highly relies on microscopic devices, we will take a short digression into the principles and the different types of microscopes that were used in this work.

The first microscopes were already used in the 17th century. The most basic design of a simple microscope relies on nothing else, but a convex lens, which is used as a magnifying glass, as shown in figure 4.1a. Higher magnification can be achieved with the use of a compound microscope where two lenses are implemented, called the objective lens and the eyepiece lens. The objective is located closer to the object and projects an image onto a point within the microscope, labelled image 1 in the schematic representation in figure 4.1b. This mage is then magnified by the eyepiece; therefore, the viewer sees an inverted and enlarged image of the object (image 2). The position of the objective lens must be adjusted for the distance between object and eyepiece in order to focus the image correctly onto a point within the microscope.

In this so-called bright-field microscopy, the sample is illuminated from a light source below, and the sample contrast is caused by attenuation of the transmitted light. This technique is therefore limited to dark objects or at least strongly reflecting objects. Another issue is the diffraction limit of a microscope, which was found in 1873 by Ernst Karl Abbe. It states that the minimum resolvable feature size d can be calculated from the wavelength λ of the source of illumination divided by twice the refraction index n of the medium being imaged in and the sinus of the half-angle θ subtended by the optical objective lens.

$$d = \frac{\lambda}{2n\,sin\theta} = \frac{\lambda}{2NA}$$

The term "n·sinθ" can be optimized in modern optics to a value of 1.4 and is called the numerical aperture NA. Therefore, we obtain the Abbe limit d = λ/2.8, which yields a distance of roughly 140 nm for light with the shortest visible wavelength of 400 nm. This resolvable distance is sufficient for the imaging of biological cells but not for the imaging of nanostructures.

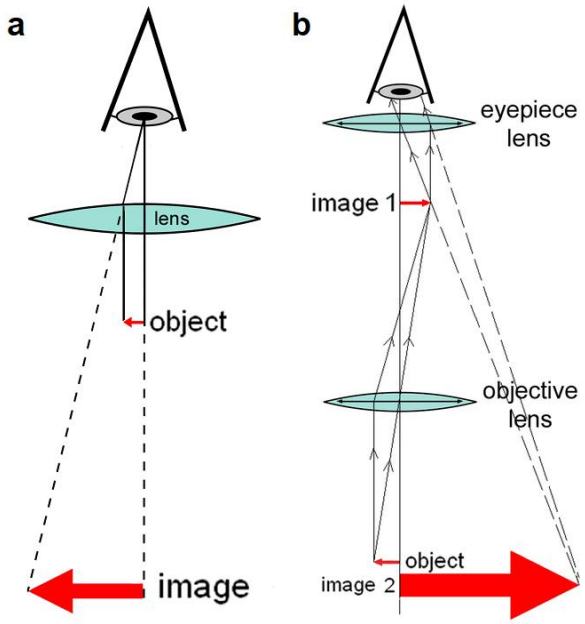

Figure 4.1: Schematic representation of **a**) a simple microscope with a single lens and **b**) a compound microscope with a objective lens projecting an image into the microscope which is magnified by the eyepiece lense. Illustration by Fountains of Bryn Mawr, distributed under CC BY-SA 3.0 at [1].

4.2 Dark-field Microscopy

The basic principle of dark-field microscopy was already described in 1837 by Bancroft Reade [74]. He used a candle next to his microscope to illuminate his sample from certain angles. With this method, he was able to obtain images without a bright background and, therefore, achieved more brilliant colors while imaging his samples. This simple concept of leaving the light source out of the field of view and allowing only the light scattered by

the samples to enter the objective is still used today to make otherwise undetectable properties or features of samples visible.

The schematics of a modern dark-field microscope are shown in figure 4.2. It starts with a light source on the top, which emits light in different directions. The first lens, the collector, is responsible for aligning the light in a parallel fashion. The central aperture is a critical component of the setup, it blocks the light in the center, leaving only a ring of illumination to pass through. The condenser lens now focuses this ring of light onto the specimen. The light scattered by the sample can now enter the objective, while the aperture of the objective blocks the directly transmitted light. This is only one possible straightforward design of a dark-field microscopy setup, as the light can also, for example, be introduced from the side using mirrors.

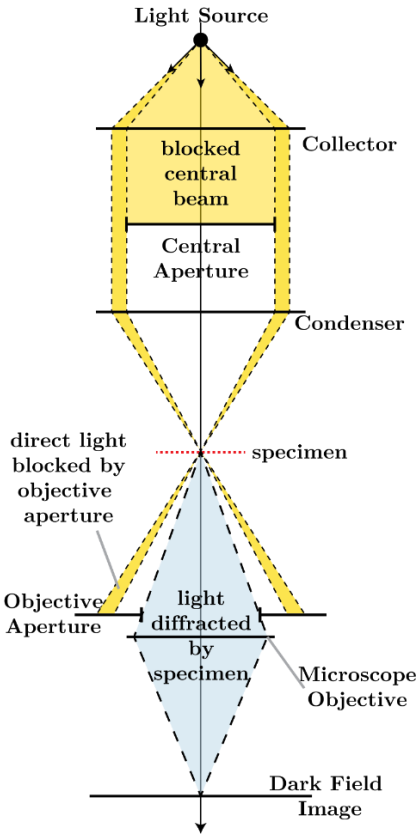

Figure 4.2: Schematic representation of a dark-field microscopy setup with a ring-shaped light beam illuminating a sample. While the light diffracted by the sample is collected, the transmitted light is blocked. Illustration by R0oland, distributed under CC BY-SA 3.0 at [1].

Dark-field microscopy has advantages compared to bright-field techniques if the samples do not form a strong contrast to a white background without prestaining. The samples must, however, be illuminated more strongly, which could potentially damage samples. Another possible application of dark-field microscopy is that even objects smaller than the diffraction limit can be imaged as long as they scatter the light strongly enough. For this, the illumination has to be especially strong, while the background has to be particularly dark. If these circumstances are given, metal nanoparticles with a 50 nm diameter or clusters and assemblies of even smaller particles can produce bright spots with a characteristic wavelength. Richard Zsigmondy first used this technique to study the properties of gold nanoparticles and received the Nobel prize in chemistry for this work in the year 1925 [75]. To identify single particles in this manner, the sample has to be appropriately diluted before imaging. Then, however, different sizes and shapes of nanoparticles can be identified by their emitted spectra, representing the plasmon resonance frequencies of the individual particles. These spectra can be spectrally resolved by a grating and subsequently recorded with a spectrograph and a charge couples device (CCD) camera. The entrance of the spectrograph can be adjusted so that the signal of a single particle can be detected in this manner.

4.3 Transmission Electron Microscopy

Because of the aforementioned Abbe limit d = $\lambda/2.8$, it is impossible to achieve a resolution on the single nanometer scale with light spectroscopy. Since this resolution is necessary to image nanostructures in detail, it is necessary to use electron microscopy. Due to the wave characteristics of electrons, a beam of electrons can be used just like a light beam in microscopy. The advantage of this is that highly energetic electrons have a much smaller wavelength than light. The electron wavelength is given by the de Broglie wavelength:

$$\lambda_e = \frac{h}{p}$$

Where h is the Planck constant and p is the electron's momentum. Since electrons in an electron microscope approach the speed of light c, it is necessary to implement relativistic

corrections. One can formulate an expression for the relativistic momentum p from the energy-momentum relationship:

$$E^2 = E_0^2 + c^2 \cdot p^2$$

$$p = \frac{\sqrt{E^2 - E_0^2}}{c}$$

Using $E = E_0 + E_{kin}$

$$p = \frac{\sqrt{(E_0 + E_{kin})^2 - E_0^2}}{c} = \frac{\sqrt{2 \cdot E_0 \cdot E_{kin} + E_{kin}^2}}{c}$$

Plugging this expression into the de Broglie wavelength, the relativistic formula for the electron wavelength can be obtained:

$$\lambda_e = \frac{hc}{\sqrt{2E_0E_{kin} + E_{kin}^2}} = \frac{hc}{\sqrt{2m_ec^2eV_a + (eV_a)^2}}$$

where m_e denotes the rest mass of an electron, e the elementary charge and V_a the acceleration voltage. This yields an electron wavelength of only 4 pm for an acceleration charge of 80 kV, roughly 100 000 times smaller than the wavelength of visible light. The limit of resolution obtainable, usually referred to as the information limit, is typically defined by the cut-off frequency q_{max} for the contrast transfer function. It is given by:

$$q_{max} = \frac{1}{0.67(C_s\lambda_e^3)^{\frac{1}{4}}}$$

In this, C_s is the spherical aberration coefficient and λ_e is still the electron wavelength. For a microscope with a C_s value of 0.5 mm and the before calculated electron wavelength, we obtain a cut-off value $1/q_{max} \approx 0.3$ nm.

The first electron microscopes were already developed in the 1930s, although their resolution was not better than those achieved in light microscopy. Through further research and the development of the transmission electron microscope (TEM) in the 1970s the resolution could be significantly improved and is still being improved to this day. Modern TEM imaging can achieve resolution below 50 pm [76] and even visualize single atoms such as carbon and even hydrogen [77].

As shown in the schematic layout of a TEM in figure 4.3, electrons are first being produced in the electron gun. The electron gun consists of a filament, a biasing circuit, a Wehnelt cap, and an extraction anode and can produce a narrow and collimated electron beam with defined kinetic energy. For the voltage difference between the cathode and the arc not to create an arc, it is essential to have a vacuum inside the microscope. In the next step, a vacuum is also needed to increase the mean free path of the electron beam. This vacuum system has to be re-evacuated every time the specimen holder is inserted into the setup, even though airlocks reduce the vacuum loss to a minimum. The specimen holder holds a thin support mesh, called TEM grid, of usually about 3 mm in diameter. The thickness of the TEM grids is only a few to 100 µm, as the electron beam has to penetrate the substrate. The higher the atomic number of the sample's atoms, the higher will be the interaction with the electrons. Biological samples therefore have to be stained with heavy metal atoms to give a higher contrast in the images. For this, solutions with heavy metal salts derived from uranium, molybdenum or tungsten can be used. During this negative staining, the salt attaches to the biomolecules, which makes the outline and cavities of the molecules visible. In the final step, the image is magnified and focused onto an imaging device. This is typically a fluorescent screen for direct viewing or a sensor such as a scintillator attached to a charge-coupled device for saving the images.

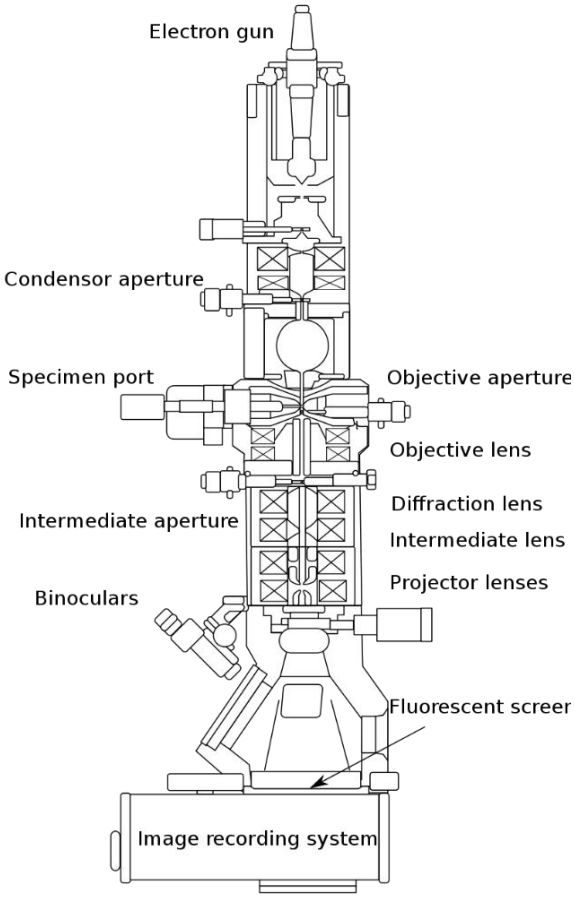

Figure 4.3: Schematic representation of a basic TEM, focusing electrons produced in the electron gun onto a thin sample, which is then projected onto a fluorescent screen. Illustration by Gringer, distributed under CC BY-SA 3.0 at [1].

II

Experiments

Chapter 5

Large Pitch and Small Pitch Helix

5.1 Introduction

This chapter is based on the research presented in [78]. Figures and text reused under the terms of the Creative Commons CC BY.

Chirality can be found in all domains of nature. It is a fundamental feature in particle physics, electromagnetism, chemistry and biology, just to name a few [79-82]. Chiral objects do not have any mirror plane or inversion symmetry, therefore they can not be spatially aligned with their mirrored counterpart, which is called their enantiomer. To characterize natural chiral molecules or artificial chiral nanostructures one can use their light-matter interaction, which is reflected in circular dichroism (CD) [83, 84]. We can assemble model meta-molecules from plasmonic nanoparticles, which represent meta-atoms [85-87], accurately positioned in space by the use of DNA origami [3, 27]. This way we can reconstruct step by step the impact of varying macromolecular geometries on their surrounding optical near fields. In this process we can demonstrate the emergence of CD signatures in the instance that we architect a third dimension and later even implement sign flipping signals through addition or removal of single particles. Furthermore, our studies and theoretical simulations reveal the hitherto unrecognized phenomenon of chiral plasmonic-dielectric coupling, which explains the intricate electromagnetic interactions within hybrid DNA-based plasmonic nanostructures.

The majority of biomolecules in nature are chiral. This feature plays an important role as many processes depend on enantiomer-selective activity, such as molecular recognition and functionality [88]. Therefore CD spectroscopy has become a viable tool for analyzing molecular compounds or proteins and is used throughout science and industry. Predicting the CD spectra of a macromolecule or deriving the molecular structure from a recorded CD spectrum, however, still remains unfeasible despite much effort [89]. Within a molecule, it is the resonances of the atomic bonds that determine its absorption while

the arrangement of the bonds relative to each other define chirality and therefore the CD signal. Molecules, both synthetic and biological, usually exhibit their optical responses in the UV range, whereas metallic nanostructures or architectures of metallic nanoparticles can be designed to express signals in the visible spectral range [54, 56, 57, 86, 90]. The optical activity in such metallic structures depends on plasmons, which are collective oscillations of electrons in metals. The surface plasmons couple to each other and create resonances that interact with the optical near field. These resonances within the metallic nanostructure, or meta-molecule, lead to characteristic absorption and CVD spectra, analogous to their molecular counterparts. We can learn to understand the optical responses of nanostructures and molecules by tailoring the electromagnetic fields. Following this approach, meta-materials with novel optical properties [72, 91], sensing devices [58, 92-94], as well as enantioselective catalysis applications [95, 96] have been studied.

Chiral nanostructures can be built from many materials, such as silica [97] or quantum dots [98-100]. Metallic nanoparticles, however, have been shown to be arguably the most suitable candidates for artificial chiral nanostructures [54, 56, 57, 86, 90]. Even though one can already measure strong CD responses from chirally shaped metal nanoparticles [101-102], the assembly of achiral nanoparticles into chiral geometries offers significantly more freedom in design. In such designs, the plasmons of the individual particles couple to each other and interact with the surrounding optical fields, which has been studied by many groups [103]. Many different approaches of synthesizing nanoparticle structures have been studied, such as ligand-protected gold and silver particle clusters [104-105] or assemblies through peptides [106], polyfluorenes [107], silica films [108], oxalamide fibers [109], proteins [110] or micelles [111]. DNA nanotechnology opens the route for specific placement of individual particles [112], which gives the possibility to design nanostructures [113] with tailored optical responses [114-117]. The DNA origami technique gives a particularly powerful tool to position nanoparticles with sub-nanometer accuracy [87, 118]. A DNA origami is made from a single-stranded scaffold strand, which is folded into any desired three-dimensional (3D) shape by numerous short DNA staple strands [119]. The resulting objects has DNA handle strands protruding from the structure. These can capture any object that is functionalized with the complementary DNA sequence, making them fully addressable for various

particles simultaneously. Due to these features, DNA origami represents a freely customizable molecular framework.

Even though helical shapes do not play a fundamental role in biology, most notably the right-handed double-stranded DNA and the alpha-helical protein units, they offer a step-by-step path to understand space and furthermore, the exact mechanisms behind chiral optical activity. Geometrical features such as pitch-length, number of particles or particles per turn can have significant influences on the CD response, as shown by many theoretical models [54, 55, 65, 86, 103, 120, 121]. In this work we present two different helical gold nanoparticle structures, assembled around a DNA origami, which serve as model meta molecules for simulating and predicting their CD responses. They are assembled particle by particle to contribute to a deeper understanding about the origins of molecular plasmonic CD. Through our findings we elucidate in this context the role of dielectric materials in the vicinity of plasmonic arrangements.

5.2 Chirality

We want to approach the concept of chirality through an arrangement of spheres in space. It is important to consider how the given number of particles determines the highest possible dimension of any geometrical configuration (Figure 1). In the simplest case, with only a single sphere (S_1), we coercively obtain a 0-dimensional assembly. Two spheres (S_1 and S_2), however, always define a line L connecting them. In such 1-dimensional geometries one can define an infinite number of mirror planes through L and an additional mirror plane half way between the spheres, perpendicular to L. When we add a third sphere S_3, there are two different possibilities. S_3 will either be placed on L, leaving the geometry 1-dimensional or it will be located anywhere else in space, making the structure 2-dimensional. In the latter case, S_1, S_2 and S_3 will define a plane P, which will automatically be a mirror plane to the structure. If the three spheres form an isosceles triangle, another mirror plane will exist perpendicular to P. In the last step a fourth sphere S_4 is added, which can make the structure 3-dimensional, if not placed on P. Such a structure has no more imperative mirror plane, meaning it can be chiral, as shown for example in Figure 1d. Note that by adding a further sphere, a previously chiral structure

can be become achiral, just like an achiral structure can become chiral by adding more spheres.

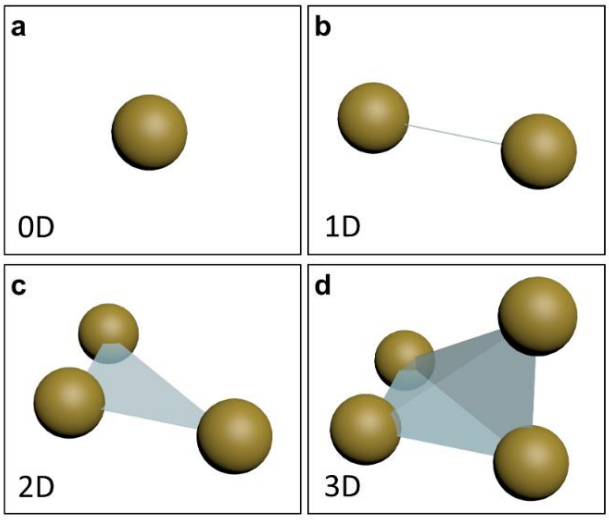

Figure 5.1: **a**) A single sphere in a 0-dimensional geometry (0D). **b**) Two spheres defining a line L in a 1D geometry. **c**) Three particles defining a plane P in 2D. **d**) Four particles in a chiral assembly in 3D.

5.3 Experiments and Discussion

We now explore the onset of chirality by assembling particle by particle two different types of gold nanoparticle helix around a DNA origami trunk. One type of helix holds up to seven 40 nm gold particles with an offset of 29 nm. This type is called Large Pitch Helix (LPH), because the pitch will become the crucial feature for understanding the various CD responses of helices assembled from 4, 5 and 5 particles. The second type is termed Small Pitch Helix (SPH), as this helix has an offset of only 11 nm per particle. It can host up to six 30 nm gold nanospheres. Its small pitch leads to the particular feature that the fifth particle is located right above the first one at a surface to surface distance of 14 nm, which is the same distance as between the first and the second particle, or second and third etc.. Both types of helices have a rotation around the helical axis of 90° per particle and a radius of 30 nm, measured from the center of the particles to the center of the helix. The particles are functionalized with thiol-modified DNA sequences, called anchors. Their DNA sequences are complementary to the sequences of the so-called handles, which are protruding from the DNA origami bundles. For the LPH a 24-helix bundle was used, in a

monomere version for 1-4 particles and in a dimere version for 5-7 particles. In case of the LPH, a 48-helix bundle was used. We synthesized samples with varying numbers of gold particles attached, always starting with a single particle at the end of the trunk, as shown in schematic drawings and transmission electron microcopy (TEM) pictures in Figure 5.2.

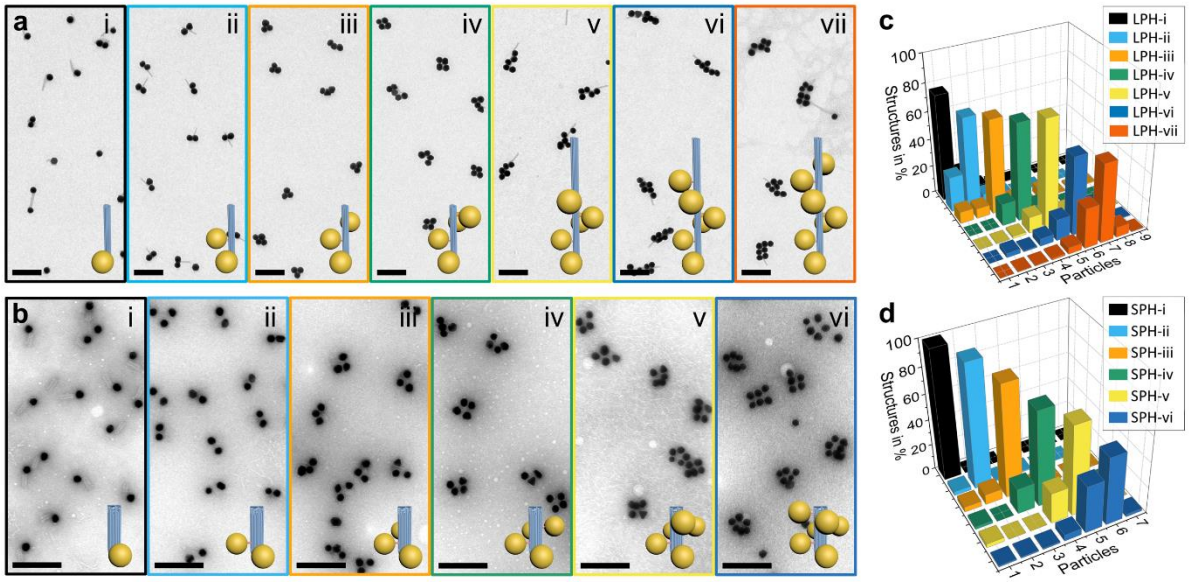

Figure 5.2: **a**) Large Pitch Helix (LPH) with up to seven 40 nm gold particles attached (LPH-i to LPH-vii) and **b**) Small Pitch Helix (SPH) with up to six 30 nm gold particles attached (SPH-i to SPH-vi), shown in TEM pictures and 3D models as inlays. Scale bar: 200 nm **c**) Synthesis yields of LPH-i to LPH-vii and **d**) SPH-i to SPH-vi. The majority of all samples show the expected number of particles. Structures with less particles then expected become increasingly more common for samples with higher particle numbers, while structures with more particles then expected are less common for LPH and even negligible for SPH. Approximately 250 individual structures were analyzed.

TEM studies produced a satisfactory yield for correctly assembled LPH-i to PLH-vii architectures of 76 %, 65 %, 68 %, 70 %, 77 %, 56 % and 56 %, respectively, as to be seen in Figure 5.2b. The majority of disarrangements are the result of nanoparticles binding non-specifically to the ends of the multi-helix DNA bundles, leading to fractions of 7 % to 18 % of the structures carrying one or more extra particles. The synthesis of SPH-i to SPH-vi, in contrast, shows successful assembly yields of 97 %, 96 %, 87 %, 74 %, 70 % and 53 %, respectively. The fraction of structures carrying more particles then intended is strikingly lower (< 3 %) then for the LPH. The reason for this is a design feature of the 48-

helix bundle of the SPH, which prevents additional gold particles to bind to the ends of the DNA helices. This is achieved by protecting the otherwise accessible DNA endings by short DNA duplexes, crossing the top and bottom of the origami trunk in a perpendicular orientation to the other DNA helices, as shown in the 3D model in Figure 5.3.

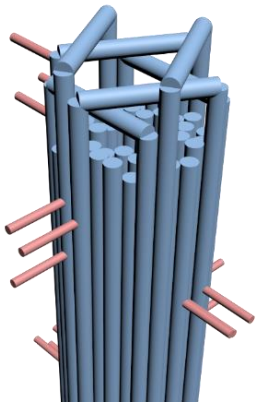

Figure 5.3: 48-helix bundle design with perpendicular DNA duplexes crossing over the DNA helix endings to prevent non-specific binding of nanoparticles.

Metallic nanoparticle-based meta-molecules are optically most active near their plasmonic resonance frequency. This is expressed in the highest absorbance as well as the strongest CD response around this frequency. For this study we designed left-handed chiral objects, which typically show bisignate peak-dips signals. We obtained such signals with peaks around 524 nm and dips around 558 nm for both helix designs carrying four particles (LPH-iv, SPH-iv), which represent our minimal chiral meta-molecules. Just as expected, we observed no or only negligible CD responses for samples with one or two particles, i.e. for LPH-i, LPH-ii, SPH-i and SPH-ii. Surprisingly, we recorded a CD signal for meta-molecules with three particles, a peak at 535 nm for SPH-iii and even a dip-peak spectrum around the same wavelength for LPH-iii. Numerical simulations for three particles do not show any CD signal, since three particles form a plane and cannot be chiral. This does not hold true, however, if we account for the DNA origami, which can be approximated as a dielectric cylinder penetrating the plane P in an oblique angle. These augmented simulations now yield a CD response for meta-molecules with three particles (LPH-iii and SPH-iii). Furthermore, structures with two particles (LPH-ii and SPH-ii) even show a CD signal, as the symmetry here is equally broken.

The striking difference between the LPH and the SPH can be seen when we consider the assemblies with five particles and more. For the LPH, each particle added to the structure represents an increase in CD response, for it augments the chiral shape of the meta-molecule, which our simulations corroborate. In the case of the SPH-v the situation is different. The distance between the first and fifth particle is so short that the plasmon-plasmon interactions between them induce a right-handed geometry within the structure, which effectively leads to annihilation of the original left-handed signal. This leads to SPH-v showing a distinctly diminished CD response in the simulations and even close to no CD signal in the experiment. Both theory and experiment show a slight increase in CD response with the addition of a sixth particle to the helix (SPH-vi). This overall trend can be seen in Figure 5.4e, where the peak CD intensities for all experimental samples and the corresponding simulations were plotted, showing excellent agreement. Additionally, the extinction peaks of the experiments match those of our simulations, showing a spectral shift into the red with increasing numbers of particles. This is typical for assemblies that exhibit plasmonic coupling.

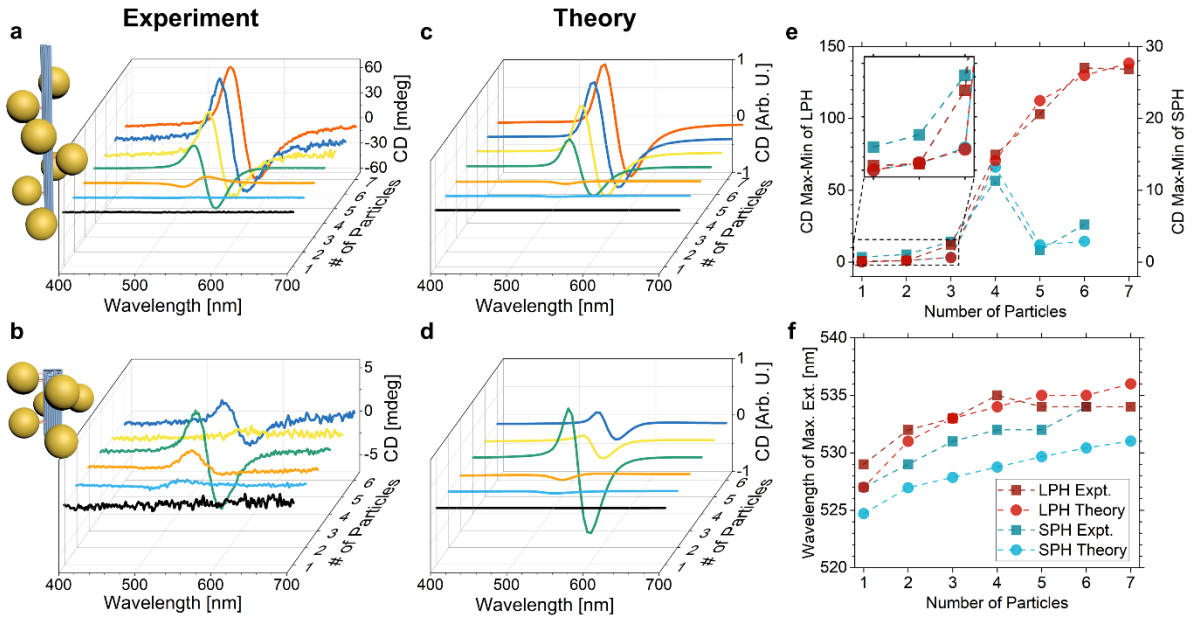

Figure 5.4: **a**) CD measurements of LPH-i to LPH-vii and **b**) SPH-i to SPH-vii, normalized by the maximum extinction value for each sample. **c**) Simulated CD spectra of LPH-i to LPH-vii and **d**) SPH-i to SPH-vii, the amplitudes were matched to the experimental values. **e**) Amplitudes of CD response and **f**) peak extinction wavelengths of LPH-i to LPH-vii (red) and SPH-i to SPH-vi in experiment (squares) and theory (circles).

5.4 Theoretical Model

For further understanding, the energy densities of the electric field u can be displayed color-coded on the surfaces of the metallic nanoparticles and the dielectric DNA cylinder, as shown in Figure 5.5. Wherever their surfaces come close enough to each other, neighboring particles can exhibit plasmonic coupling, which manifests itself as increased energy densities, or hot spots. This can also be observed on the dielectric surface, wherever the nanoparticle are close, we observe the formation of weak hot spots. This is the reason why a discernible CD signal already emerges for the cases of three nanoparticles (LPH-iii and SPH-iii). The dielectric cylinder protrudes through the nanoparticle plane in an oblique angle, leading to an overall chiral assembly. The CD responses of LPH-iii and SPH-iii do not resemble the bisignate spectra that are usually observed for helical assemblies but instead describe a single dip, that is rather typical for right-handed assemblies. Four particles define a full helical turn, thus clear, bisignate CD signals appear for LPH-iv and SPH-iv. In the case of LPH-v, no coupling between the first and fifth particle arises, as their surfaces are 76 nm apart, the structure gains chiral features and the signal therefore increases further for every added particle. Strikingly, for SPH-v a new hotspot becomes visible between the first and fifth particle. It drastically changes the near field of the incoming light and results in an almost complete breakdown of the CD response.

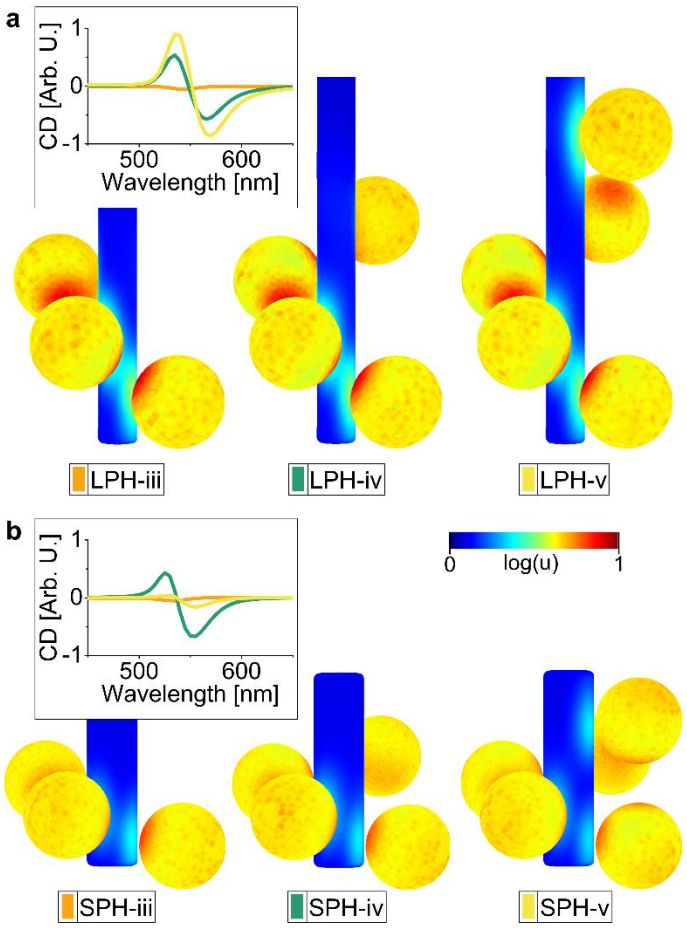

Figure 5.5: Simulated optical field density u visualized with logarithmic color-coding [a.u.] on the surfaces of gold particles and the dielectric DNA origami rod for a) LPH-iii to LPH-v and b) SPH-iii to SPH-v. Inserts show simulated CD spectra for LPH-iii to LPH-v and SPH-iii to SPH-v, respectively.

5.5 Conclusion

In this project we were able to design plasmonic meta-atoms and sculpt light matter interactions through carefully considering the geometrical features of two model systems with nanometer precision. The DNA origami technique provided us with the necessary precision in synthesizing these structures. Our simulated CD responses in multi-angle illumination settings could explain the experimentally observed spectra in great detail. In accordance with the computed near field distributions we could reveal resonant hot-spots not only between the metallic particles but also between particles and the dielectric DNA. This new model of incorporating the response of the DNA scaffold adds an additional layer of understanding to complex CD measurements and could lead to further advances in analysis of both chiral assemblies as well as natural molecules.

Chapter 6

Chirality Transfer

6.1 Introduction

This chapter is based on the research presented in [122]. Figures and text reused under the terms of the Creative Commons CC BY.

If a structure does not have any internal planar symmetry, it is called chiral. Chirality describes a geometric feature of a structure that cannot be brought to coincide with its mirror image through the geometrical transformations of rotation or translocation. This object and its mirror image of opposite handedness are called enantiomers. A right-handed molecule can have significantly different functions in biological systems in comparison to its left-handed counterpart [123]. Chirality therefore plays a decisive role in nature, as chiral molecules possess distinctive geometrical and thus chemical features. In addition to that, chiral molecules exhibit intricate optical responses upon irradiation with linearly or circularly polarized light, which are called optical rotary dispersion (ORD) and circular dichroism (CD), respectively. CD has many possible applications, such as the monitoring of protein folding processes [124] or the evaluation of the chiral quality of synthetic chemicals [125]. Chirality also enables the creation of designer architectures such as chiral photonic crystals [126-127] and chiral metamaterials [72, 91, 128]. Chiral nanoparticles (NPs) can trigger optical activity [101, 102, 129, 130] as well as clusters of several achiral NPs assembled into chiral structures, which form plasmon-plasmon interactions between the surfaces of the NPs [54-56, 90, 103, 131]. Chiral plasmonic systems that trigger CD responses show a multitude of possible applications with great potential ranging from chiral discrimination of molecules [132] and sensing [58, 92, 94], over enantiomer-selective catalysis [95] to circular polarizing devices [91].

Adding to CD signals arising from either pure organic compounds or inorganic particles and assemblies, both of these domains can be combined when interactions between them occur, which give rise to strong effects. As an example, plasmonic surfaces and particles

can strongly increase the CD signals of biomolecules in their proximity, which can enhance the sensitivity of chiroptical detection of biomolecules [93, 110, 133-137]. In this kind of experiment, the strong, plasmon-induced electromagnetic (EM) near-field couples to the chiral near-field of the biomolecules. These biomolecules usually have their maximum in the UV and extend only a weak tail into the visible spectral range. The CD transfer therefore leads to augmentation of the signal strength in the plasmonic window that predominantly occurs in the visible and near infrared (NIR).

While looking for a technique to implement complex plasmonic particle assemblies with nanometer accuracy, DNA nanotechnology [112] and in particular DNA origami [3, 27] proved itself to be a powerful tool for that [87]. By folding a long single-stranded DNA, serving as a scaffold strand, into shape by hundreds of synthetic staple oligonucleotides, DNA origami structures can be formed into any desired shape [112]. NPs can be attached by first functionalizing them with thiol-modified oligonucleotides, which then in turn hybridize at specific positions on the origami structure, making DNA origami an ideal platform for nanostructures with tailored optical functionalities [54, 56].

Chiral nanorod (NR) assemblies have been achieved in various ways by using DNA origami. Assemblies in which rods are crossing each other in an X-shape or an L-shape are predominant [138, 139]. These geometries can be synthesized in switchable configurations [57, 109, 140-141] which further allow for sensitive detection of biomolecules [58]. The distances between the nanoparticles play a crucial role in all of these assemblies, since plasmon-plasmon interactions are usually limited to a range of a few nanometers [57, 138-141]. Plasmonic energy can traverse efficiently over sufficiently small gaps between NPs forming chains [142] and plasmon transfer can even take place between NPs with different resonance frequencies by quasi-occupation of different transfer channels [143]. Transfer of chiral signatures over chains of particles has already been predicted theoretically [144], but experimental prove has so far been lacking.

In this work, we explored this new type of transfer over long distances. In our experiments, plasmon-assisted chiral interactions occurred in chiral assemblies of two nanorods with a surface-to-surface distance of over 60 nm. The presence of a third, spherical transmitter particle in between the rods efficiently coupled the near-field of the rods leading to strong signal increase of the longitudinal modes and to the evolution of new CD features in the spectral range of the spherical particle.

6.2 Experiments

The compound DNA origami platform we designed and synthesized for this project is composed of two individual structures, which are first folded individually and then attached to each other in the next step. At this point, the dimer structures overall length adds up to 100 nm. By using thiol-DNA functionalization, two gold NRs, each 54 nm long and 23 nm wide, are accommodated at the origamis ends (Figure 6.1). By design, these rods have a surface-to-surface distance of 62 nm and are tilted by 90° in respect to each other, as seen from a perspective along the axis of the origami structure (Front view). In this perspective, the ends of the two gold rods also overlap, resulting in an L-shaped object. An additional nanoparticle, a 40 nm gold nanosphere (NS) can be attached in between these overlapping ends of the NRs. It serves as a plasmonic transmitter and is spaced 12 nm from each NR.

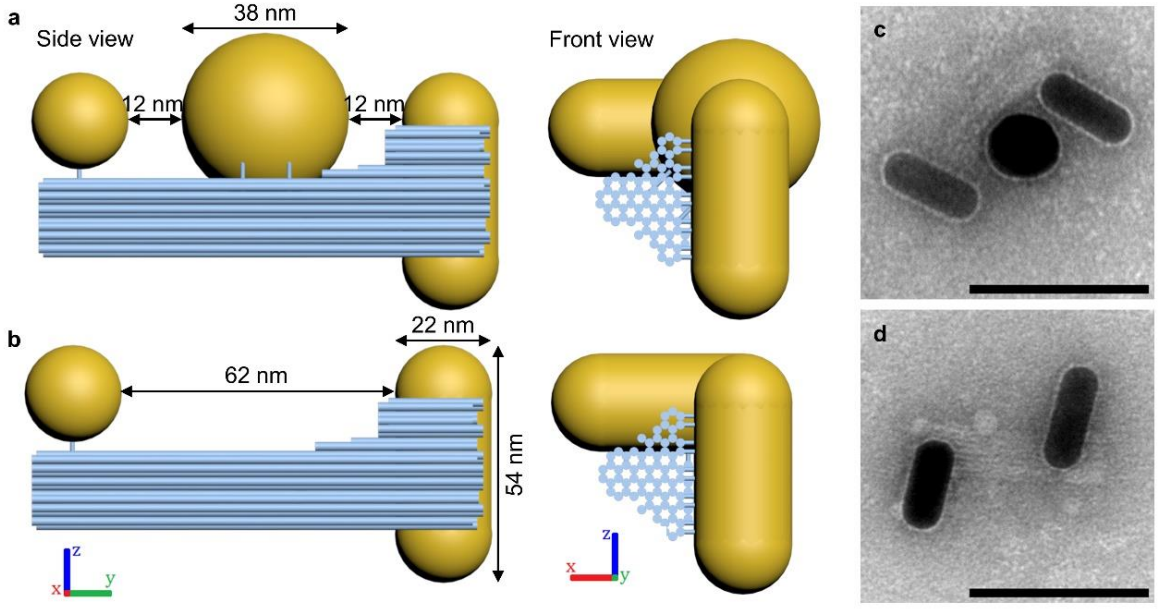

Figure 6.1: **a**) Side and front view of DNA origami assembled with nanoparticles in a NR–NS–NR arrangement and **b**) a NR– –NR arrangement. The blues cylinders represent the DNA helices of the DNA origami. The NRs and NSs are attached via thiolated DNA strands that are anchored to the origami structure. **c**) Transmission electron micrographs of structures in the NR–NS–NR arrangement and **d**) in the NR– –NR arrangement. Scale bars: 100 nm

We synthesized samples with only the NRs (NR– –NR) as well as samples with the center nanosphere present (NR–NS–NR) to investigate the effect of the transmitter particle. We confirmed the successful assembly of the structures by transmission electron microscopy. Unfortunately, the TEM micrographs are not able to depict the assemblies in solution, which is how they were synthesized and also how they will perform their task. To take TEM micrographs, they need to adsorb and dry on the TEM grids before being imaged in vacuum, due to this process any angular correlation between the particle is lost.

A study of 200 assemblies of the sample NR– –NR was conducted to investigate the quantity of correctly and incorrectly assembled structures (Figure 6.2). It revealed, that the majority (58 %) of structures was found to be in the expected arrangement. The reason for disarrangement were manifold, the most common of these, however, being a structure with an extra nanorod attached (NR– –2NR; 15 %), which occurs when 2 NRs attach to the origami handles, which are designed for a single NR. Almost as frequent (14 %) were assemblies containing a NS instead of a NR on one side (NS– –NR). This is due to the NR synthesis, which leaves spurious NSs in the mix, which cannot be completely removed from the NRs. Likewise, a study of 300 assemblies of the sample NR–NS–NR was conducted and resulted in 51 % well-assembled structures. The spurious NSs within the NRs were also a factor here, resulting in structures with a NS instead of a NR on one end, which represented the most frequent misassembly (NS–NS–NR; 18%). The next common disarrangement were assemblies lacking the spherical particle (NR– –NR), contributing to 9 % of all assemblies.

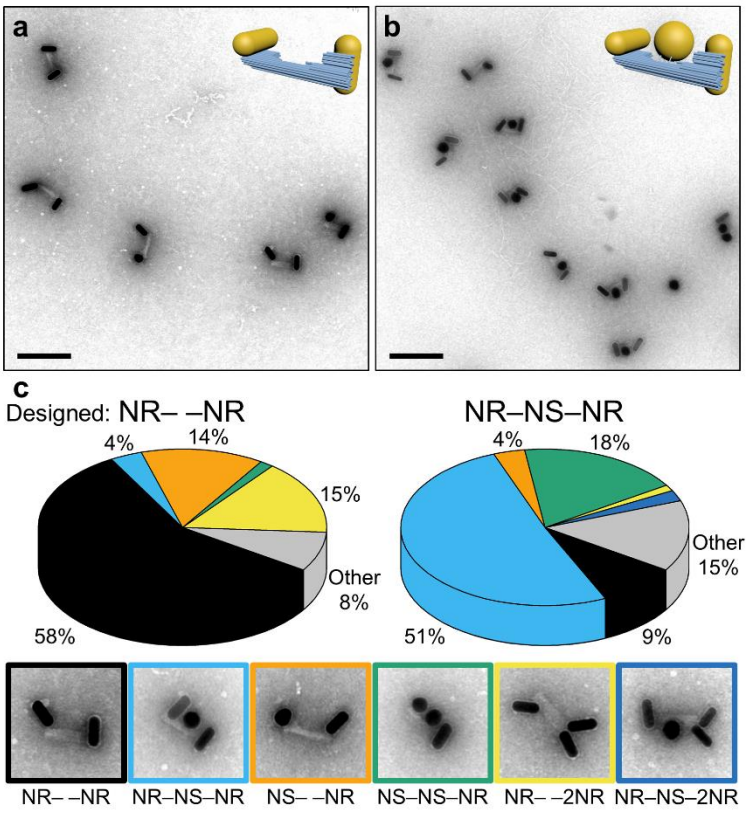

Figure 6.2: **a**) Electron micrographs of sample NR– –NR and **b**) of sample NR–NS–NR, both with inlays of 3D models of the respective structures. **c**) Percentages of assemblies found in samples NR– –NR and NR–NS–NR. Structures assembled as designed pose the majority in both samples with a variety of misassemblies occurring, shown in different colors in the pie diagram. Electron micrographs with different colored frames correspond to these various configurations. Approximately 500 assemblies were studied.

To perform CD measurements with them, the plasmonic assemblies are dispersed in an aqueous solution. Extinction values of the longitudinal mode of the NRs indicate the concentration of assemblies to ~ 0.1 nM. Since the concentration varies from sample to sample, the CD signals were normalized by the maximum extinction amplitude for each sample. In all of these measurements a multitude (~ 10^9) of individual assemblies, present in all possible orientations, are measured in the interrogating path. Therefore, no contribution of linear dichroism is to be expected in the experimental spectra. As to be seen in Figure 6.3, the CD signal for the sample NR– –NR shows a typical signal for right-handed chiral L-shaped nanostructures with a dip at 648 nm and a peak at 698 nm. This response is close to the NRs longitudinal plasmon frequency of 676 nm. The NR–NS–NR sample shows a similar dip-peak signature, the amplitude, however, is increased 3.5-fold in comparison to the assembly without transmitter particle. The peaks are also red-

shifted in comparison, the minimum to 657 nm and the maximum to 704 nm. This matches a shift in the extinction spectrum, where the peak of the NRs longitudinal mode is at a wavelength of 681 nm. Another noticeable difference in the spectra is the additional peak-dip signal around the NSs plasmonic resonance frequency at ~530 nm. A slight positive deflection can be observed at around 512 nm, followed by a pronounced negative deflection a 557 nm, with the signal crossing the zero-line at 530 nm.

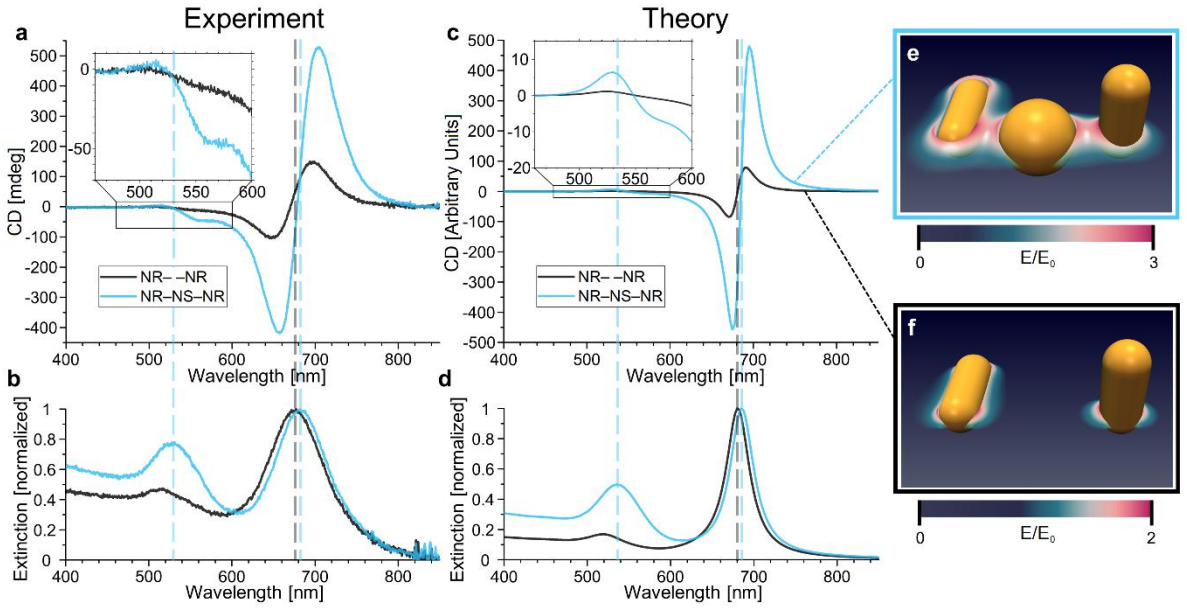

Figure 6.3: **a**) CD and **b**) extinction measurements of samples NR– –NR and NR–NS–NR, all normalized by the maximum extinction value. **c**) Simulated CD and **d**) extinction spectra of samples NR– –NR and NR–NS–NR. Signal strength was roughly matched to the experimental CD amplitude. **e**) 3D models with heat map of electric near-field intensity around the plasmonic particles for NR–NS–NR and **f**) NR– –NR arrangements.

6.3 Numerical Simulations

The numerical simulations for this project were done by Sven Burger and his group at the Zuse Institute Berlin. They are based on the premise, that two metallic rods which are arranged in a chiral fashion can be treated as a coupled electron oscillator system. Its electronic response is therefore equivalent to the mechanical Born-Kuhn model leading to analytical solutions in the dipolar limit of large distances [145-148]. In this case, the complex interplay of multipolar electromagnetic fields around two rods and a transmitter particle give rise to the optical response. To compute these CD spectra of the various

nanoparticle arrangements we were constrained to numerically solve the Maxwell's equations. The gap regions in our trimer structures host so-called hot spots, which represent a particular challenge for an analytical theory. A higher-order finite-element method (FEM) was used for solving Maxwell's equations, implemented in the solver JCMsuite [149]. To discretize the geometry a tetrahedral mesh with curvilinear mesh elements along the curved surfaces of the NPs was used. High numerical accuracy was ensured by employing a conservative setting of the numerical parameters. We used tabulated data for Au [150], the material of the NPs, and a constant refractive index of 1.4 for the background material. For the excitation, circularly polarized plane waves of various wavelength and incidence directions were used. The electromagnetic field, that is absorbed, as well as the energy that is scattered outwards, corresponding to each circularly polarized source term with left-handed and right-handed circular polarization (LCP and RCP), are obtained in post-processes. The sum of absorption and scattering for both LCP and RCP and for all six directions of incidence results in the extinction. The difference between absorption and scattering for both polarization directions, normalized by the extinction maximum of the respective wavelength spectrum, yields the CD (g-factor). The simulated spectra are shown in Figure 3c and 3d. Heat maps visualizing the coupling via near-field around the particles are shown as well (Figure 3e and 3f).

6.4 Discussion

Comparing the simulations to the recorded data, one can see many consistencies as well as some noticeable differences. The first discrepancy between theory and experiment is the less pronounced enhancement factor as well as the broadened peaks in the experimental data. This can be explained by the inhomogeneity of the samples, as the samples include small fractions of aggregates or particles with slightly irregular sizes. These can manifest themselves in spectral broadening, which in turn causes a reduced signal in case of the transmitter particle present. Notably. a large part of the disarrangements in the sample NR–NS–NR are achiral (NS–NS–NR and NS– –NR) and can therefore not be a source of the increased signal strength observed for the NR–NS–NR sample. The principle reason for NSs binding to positions on the DNA structure where NRs are supposed to bind can be found in the NR purification process. NSs are a side product of the NR synthesis, after purification 12 ±3 % of NSs still remain among the NRs,

as deducted from TEM analysis of the sample NR– –NR. Therefore, the proportion of NS in the sample NR–NS–NR is also increased from 33 % to 41 ±3 %. This is reflected in the extinction spectrum for both samples by a stronger peak at the NS resonance frequency range.

The exact positioning of the rods in our simulations also turned out to be a very important factor for the strength of the calculated CD response (Figure 4). To understand the general behavior, it is best to think about the extreme arrangement of two NRs crossing each other in their midpoints. This arrangement would resemble an achiral + and hence no CD would be observable. From there we moved the NRs in our simulations outwards in 2 nm steps, towards an L-shape. In the first nanorod position (NRP 1) only a weak CD response is generated, but the further the ends of the NRs are moved outwards (NRP 2-7), the stronger the CD response around the NRs longitudinal mode as well as the signal around the NSs resonance wavelength grows. We hypothesize that the almost matching resonance wavelength between the NSs (530 nm) and the NRs transversal plasmon mode (516 nm) is a factor for such a strong dependency. Furthermore, we also found nanorod positions for maximum CD intensity, which are also expected to be tolerant to fluctuations of the particle assemblies and sizes.

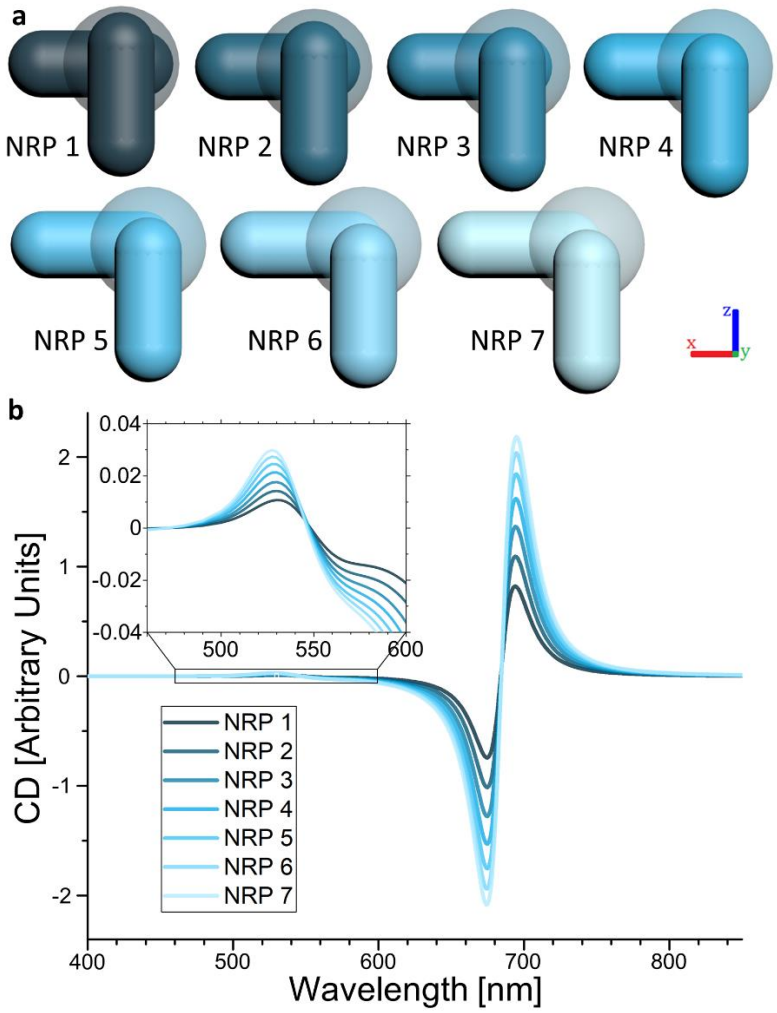

Figure 6.4: **a**) Varying nanorod positions (NRP) of the NR–NS–NR arrangement as 3D models. In each step the horizontal NR is shifted 2 nm in x-direction and the perpendicular NR is shifted 2 nm in negative z-direction. **b**) Simulated CD spectra of NR–NS–NR assemblies in NRP 1-7, starting with the weakest signal for NRP 1 and gradually increasing towards the strongest signal at NRP 7.

6.5 Conclusion

In this project, we studied the effect of a spherical transmitter particle in between a chiral structure made of two NRs in experiment and simulation. The DNA origami technique allowed us to obtain excellent control over the sample geometry, we were therefore able to synthesize chiral transfer structures with high yields and precision. The chirality response of the NRs can be coupled strongly to a spherical particle, acting as a plasmonic transmitter, located between the NRs. Computational simulations were made, which corroborate our understanding of the system. All features of the CD can be explained through the near-field around the particles and specifically through the coupling via the

hotspots. The assembled nanostructures could potentially be used as a new type of plasmonic chiral sensors for biomolecules or as transmitter elements for chiral spin locking in optical circuits. Lifting the degeneracy of chiral photons could lead to spin-dependent selection rules of optical transitions in such systems.

Chapter 7

Towards the Nanowheel

7.1 Introduction

DNA nanotechnology inherits countless possibilities for future development, one particular interesting direction being the field of nanorobotics. The design and control of synthetic nanomachines with high spatio-temporal resolution is one of the key challenges in nanoscience and technology. Many challenges have yet to be overcome to develop nanomachines that can carry out dynamic functions in biological systems, one of them being programable controlled motion in nanosystems.

Many different approaches to develop DNA based nanodevices have been investigated in recent years [151, 152]. A multitude of these ideas are based on the elementary features arising from Watson-Crick base pairing, which enable the use of single stranded extensions, so-called toeholds, and the process of strand displacement. For this, the toeholds act as a point of attachment for so-called fuel strands, which can bind to the structure and remove other single DNA strands in the process. This mechanism was used to achieve conformational changes in these DNA machines, making them early versions of DNA motors [21, 153, 154].

Using this progress and taking molecular walkers in nature as an inspiration, artificial walkers have been developed which mimic aspects of biological dynamics by utilizing DNA nanotechnology [155, 156]. These walkers can either be made of a single DNA strand [157-160] or DNA bipeds [161-163], walking along DNA tracks like the motor protein kinesin moves along a microtubule. The motion of these walkers is typically fueled by DNA strands, which trigger the strand displacement processes that, combined with Brownian motion, achieve steps along a predetermined path on a DNA track. This concept has been developed into numerous variations. H^+/OH^- and Hg^{2+}/cysteine triggers have been used as fuel instead of DNA strands [164], walkers have been synthesized into more

complex structures incorporating DNAzymes [165] or streptavidin cores [166] and DNA origami tiles have been used as tracks instead of simple DNA strands [167, 168].

Various applications can be found, from straight forward ones such as a fluorescence signal amplifier [169], or the control of chemical reactions [170] to more ambitious ones such as a nanoscale assembly line [171]. The latter depends on cargo transport, which has been shown by delivering nanoparticles along carbon nanotubes [172, 173]. However, articles can be more than just cargo, as they can also be developed into rolling motors [174, 175] that can move along a DNA-coated microparticle surface [174] or a functionalized gold film [175].

Even though all these approaches have many distinctions, they also have one crucial point in common. All of these methods rely on chemical fuel, which limits speed as well as the feasibility of motion over longer distances. In this work, we represent a novel kind of rolling DNA walker, called the nanowheel, which is able to perform a progressive, step-wise motion over large distances upon irradiation with light. This new strategy for turning light into controlled motion could open the door for transport and guiding of single nano-objects.

7.2 Design

For constructing a rotatable DNA origami nanoparticle structure we developed a design based on a 120 nm long DNA origami bundle. 12 helix bundles extend over the entire length of the origami (depicted in red in figure 7.1). 6 helix bundles, each 40 nm in length are located in the core and offer the sides additional stability (green). Lastly, a 20 nm long middle section is covered with 36 further helices (blue), making this part considerably thicker than the sides. The middle section of the origami features DNA anchor strands to attach four nanoparticles around the origami, forming 90° angles between each set of anchors. The nanoparticles attached are two spherical gold and two silver particles, all 20 nm in diameter.

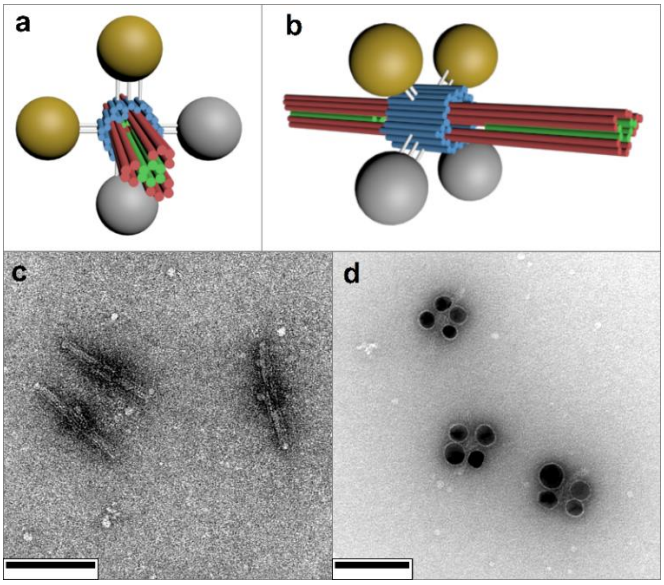

Figure 7.1: **a**) Nanowheel design as 3D model in front view and **b**) side view. The cylinders represent the DNA helices of the DNA origami. The inner helices which are one only located on the sides are depicted in green, the red helices extend over the entire length of the origami and the blues helices are the outer part of the mid section. **c**) Transmission electron micrographs of the nanowheel structure without particles attached and **d**) with two gold and two silver particles attached, each 20 nm in diameter.

The particles were simultaneously functionalized with two different DNA handles, all handles are listed in table 7.1. On the one hand, four different random sequences were used (Rnd1-4) to bind all particles to a specific position on the DNA bundle. On the other hand, one gold and silver particle each is functionalized with RT8 or RT12 handles (Figure 7.2), which are random handles with 8 thiol bases or 12 thiol bases, respectively. These handles will later bind to a glass surface functionalized with A19 anchors. Both gold and silver particles were functionalized with Rnd1-4 handles and RT8/RT12 handles in a ratio of 100:3.

Name	Sequence
Rnd1	CTC TAC CAC CTA CAT
Rnd2	CTA CTC TGC TGT CGT
Rnd3	TGC CGT CAT CAA CTC
Rnd4	CCT GTT TGC GAG ATT
RT8	ACA CAC ACA CCT TTT TTT T
RT12	ACA CAC CTT TTT TTT TTT T

Table 7.1: List of all handles and their base sequences used for functionalizing the gold and silver particles.

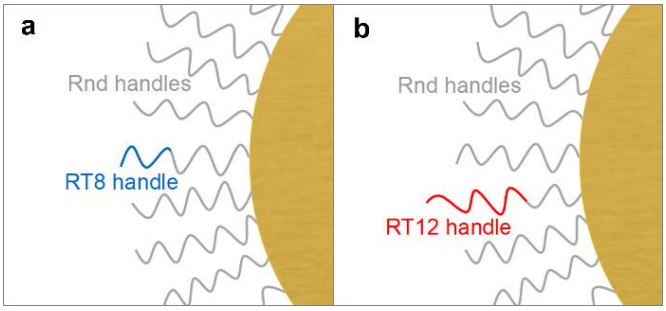

Figure 7.2: **a**) Schematic visualization of a particle functionalized with RT8 (blue) and Rnd (grey) handles and **b**) with RT12 (red) and Rnd (grey) handles.

As shown in Figure 7.3, the complete structure now has four particles attached. A gold particle with RT8 handles (Au8), a gold particle with RT12 handles (Au12), a silver particle with RT8 handles (Ag8), and a silver particle with RT12 handles (Ag12). This finished structure is placed on a glass surface, which is functionalized with A19 anchors (green), which are made of 19 adenine bases. Due to the elongated shape of the DNA origami, only two particles can touch the glass surface at a time. Independent of which particles have contact to the glass surface, the cycle of movement can be triggered from any position.

Let us assume, for example, the two gold particles bind to the A19 anchors of the surface. The nanowheel is fueled by a coherent light source that can be set to two specific wavelengths, the plasmonic resonance wavelength of the gold particles (λ(ResonAu)) and the plasmonic resonance wavelength of the silver particles (λ(ResonAg)). Electromagnetic radiation on these frequencies can couple to the plasmons of certain particles, triggering plasmonic resonance which causes them to heat up. A laser set on λ(ResonAu) would start the cycle in our example. If set to the right intensity, the heating of Au8 will cause the bonds between the RT8 handles and the anchor strands to break free, while the RT12 handles, in contrast, stay stable due to the higher melting temperature of longer DNA double strands. Au12 will therefore remain attached to the surface while Au8 will detach, giving Ag8, the next silver particle in line, the possibility to bind to the surface due to Brownian motion. The silver particles are not heated as effectively as the gold particles in this moment because their plasmons do not get excited as strongly by the radiation on λ(ResonAu). Therefore, Ag8 can attach to the surface while Au8 cannot. In the next step, the intensity of the laser is increased, causing Au12 to release

from the surface, which in turn allows Ag12 to bind to the surface. Now the laser is switched to λ(ResonAg) and the same two step release mechanism can be performed with the silver particles. Subsequently the laser can be switched back to the λ(ResonAu), starting the cycle over. Since this step-wise motion can be repeated indefinitely, the nanowheel can move as far as desired with this principle, only fueled by interchanging light.

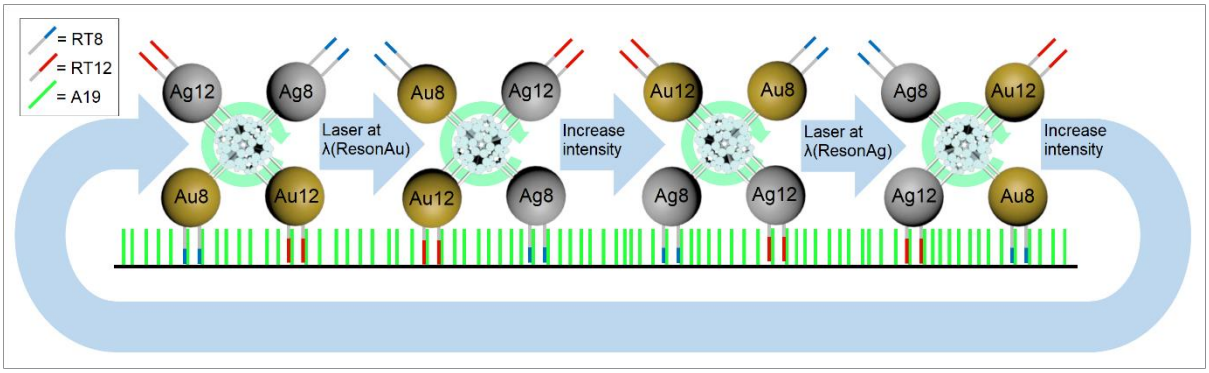

Figure 7.3: Schematic visualization of the mechanism that forces the nanowheel to rotate under illumination in the form of a laser, alternating between the resonance wavelengths of gold (λ(ResonAu)) and silver ((λ(ResonAg)), as well as between stronger and weaker intensities.

7.3 Experiments

A crucial step in this sequence of motion is the release of the particles with RT8 handles at a light intensity, which lets the particles with RT12 handles remain stable. Due to the higher melting temperature of a 12 base pair binding in comparison to only 8 base pair binding, this appears to be a straight forward requirement. The situation is, however, more complex, considering that a multitude of handles can bind simultaneously to the anchors on the glass surface.

To test this, a glass substrate was covered with a flow chamber and functionalized with A19 DNA anchor strands. For this, the surface was first coated with Biotin-BSA, which allowed Streptavidin to bind, which in turn binds to the DNA anchors that are modified with Biotin on the 3'-end. The flow chamber was then flooded with 50 nm gold nanoparticles, as particles in this size can be easily visualized using dark-field microscopy. The particles are functionalized with Rnd handles and either RT8, RT10, or

RT12 handles in a ratio of 100:3. The flow chambers were subsequently heated by flushing with buffer of stepwise increasing temperatures. After each 5°C step the substrate was analyzed with dark-field microscopy to measure the number of gold particles attached. As shown in figure 7.4, a striking difference can be seen for the temperature level of 40°C. While particles with RT8 and RT10 handles show a clear decrease of attached particles, the particles with RT12 still appear stable. This changes at a temperature of 50°C, where a strong detachment of particles with RT12 can be observed.

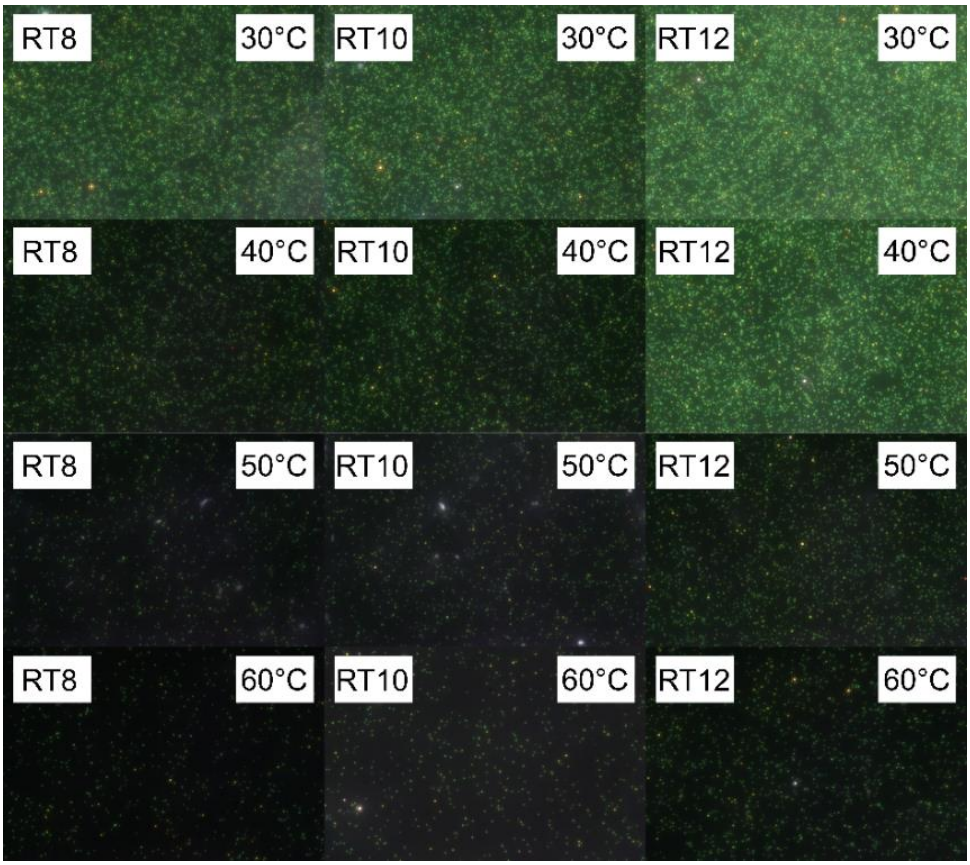

Figure 7.4: Dark-field micrographs of 50 nm gold nanoparticles attached to a glass substrate by DNA handles of different binding lengths (RT8, RT10, RT12). After being heated to different temperatures (30°C - 60°C) the gold particles detach from the substrate due to the melting of the DNA double helices. The particles with the longest DNA binding length (RT12) remain more stable than the other particles at a temperature of 40°C, due to a higher melting temperature of their DNA linkers.

The number of attached particles was measured through the mean green brightness value of the dark-field micrographs and plotted against the temperatures of different

heating levels, as shown in figure 7.5. Due to their characteristic absorbance, gold particles appear green in dark-field micrographs, their number is therefore directly proportional to the green brightness value of dark-field micrographs. The graph confirms that the largest difference between attached particles with RT8 and particles with RT12 can be found at 40°C. At this temperature, however, only 50% of the particles with RT8 are detached from the surface. A 50% chance of detachment will not be sufficient for the rotation mechanism of the nanowheel as the cycle will need to be able to repeat several times to achieve a significant movement. Even at higher temperatures a percentage of approximately 35% remains attached to the surface. The reason for that is the number of handles binding to the substrate. Although one RT8 handle has a low melting temperature, two or three RT8 handles that bind simultaneously to the substrate have a much higher melting temperature, even higher than a single RT12 handle. That is why it is impossible to precisely control functionalized nanoparticles' binding on a surface covered with DNA anchors by temperature alone.

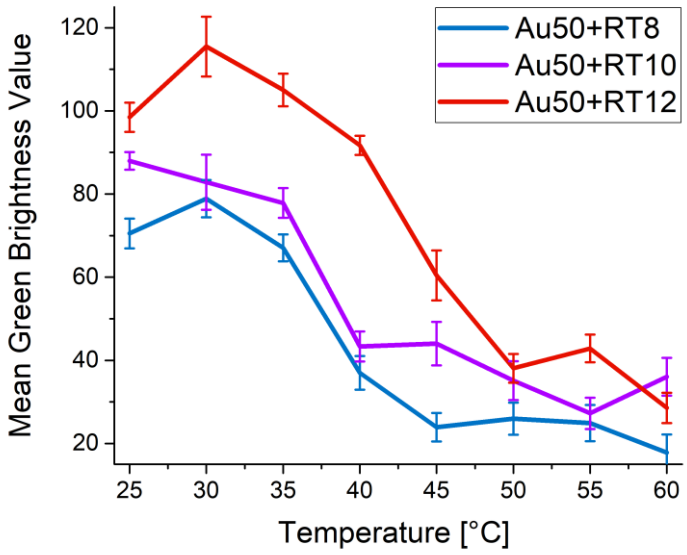

Figure 7.5: The amount of 50 nm gold particles attached to glass substrate after being flushed with buffer of increasing temperatures, presented by the mean green brightness value of dark-field micrographs. The particles are bound to the surface by DNA handles with different numbers of binding base pairs (RT8, RT10 and RT12).

7.4 Conclusion

The light-fueled plasmonic nanowheel represents a promising concept for a novel type of nanowalker. Since it is independent of any slow-working strand displacement processes, it has the potential to move on a substrate much faster than any of the previous approaches on nanowalkers. To achieve a stable cycle of operations, however, one needs to precisely define all details of the system, including the surface. The random dispersion of DNA anchors on the substrate causes restricted functionality, therefore a track system will need to be developed to offer a predefined number of anchors at precise locations. DNA nanotechnology offers several options for constructing such a track system, from elongated DNA origamis to 2-dimensional lattices. This approach would enable the particles to bind to a predefined number of DNA anchor strands, which would lead to precisely controllable detachment temperatures for particles with DNA strands of different binding lengths. Further experiments on this will have to be conducted in the future.

Chapter 8

Conclusion

DNA nanotechnology and especially DNA origami offer numerous possibilities for various applications in the field of nanophysics. In combination with metal nanoparticles they can be used to design plasmonic model-systems with freely designable geometries on the nanoscale. With these, advanced plasmonic effects such as circular dichroism can be observed and studied in great detail. This research can lead to novel optical materials with unique properties or applications in the field of nanorobotics.

In this thesis, two different approaches to further investigate plasmonic circular dichroism effects in gold nanostructures were shown. The first one exemplified how building a nanohelix out of gold particles with one particle at a time gives us a deeper understanding of chirality and how different geometries lead to different plasmonic signals. For this, a nanohelix with a large pitch and a short pitch were compared to each other by measuring their circular dichroism signals with different numbers of particles attached. This revealed how the distance between the particles can determine whether an added particle contributes to the chiral signal or causes a sign flipping signal.

The second project showed how a spherical nanoparticle can be used as a transmitter particle between two nanorods in a chiral arrangement. This does not only increase the circular dichroism response and causes a redshift of the longitudinal plasmonic resonance frequency of the nanorods but even creates a complete new chiral signal within the achiral nanosphere. Both of these effects could be fully explained by computational simulations of the near-field effects around the particles and their coupling via hotspots.

In the final project a possible application for plasmonic heating effects was given. Through specific heating of gold and silver nanoparticles a cycle of motion can be triggered that results in a rolling motion of a nanostructure on a DNA-coated glass surface. This so-called nanowheel could potentially reach higher velocities than any other

previously shown nanowalker, as the movement does not depend on time consuming strand displacement processes. Instead of having to add DNA material as a fuel, this nanowheel would only be fueled by electromagnetic waves in the form of light. Experiments have shown, however, that precise control over the entire system will be necessary, including the surface. A DNA track system could be used to precisely determine the number of DNA handles attaching the nanowheel to the surface and the temperatures needed for detachment and attachment during the rolling process. This will need to be tested in further studies.

III

Appendix

Appendix

A.1 Materials

DNA scaffold strands (p8064) were prepared following previously described procedures. [3, 176] Unmodified staple strands (purification: desalting) were purchased from Eurofins MWG. Thiol-modified strands (purification: HPLC) were purchased from Biomers. Uranyl formate for negative TEM staining was purchased from Polysciences, Inc.. Spherical gold nanoparticles were purchased from BBI Solutions. Other chemicals were purchased from CarlRoth and Sigma-Aldrich.

A.2 DNA Origami Design

Large Pitch and Small Pitch Helix

The Large Pitch Helix (LPH) was formed around a 24 helix bundle (24 HB) DNA origami trunk. This origami was synthesized with a 8064 base pair (bp) scaffold strand and 156 core staple strands. For a monomer 24 HB, used for LPH-i through LPH-iv, C4 endcap strands were added to each side (45 in total), which prevent any further attachment by leaving 4 cytosine bases protruding from the origami structure. For the larger gold helices (LPH-v through LPH-vii) a dimer 24 HB was synthesized. For this only one side is folded with C4 endcap strands while the other side uses dimerization staples which leave gaps and protruding strands that can attach to the complementary dimerization staples of another 24 HB origami (See Figure A.3). Gold nanoparticles can be attached to protruding handle strands depicted in red.

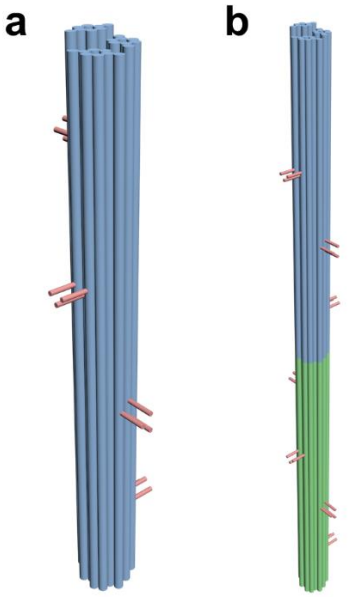

Figure A.1: 3D Model of the DNA 24 HB origami structure as a **a**) monomer structure and **b**) dimer structure with individual halfs depicted in blue and green (cylinders represent DNA helices) and handles for nanoparticle attachment depicted in red.

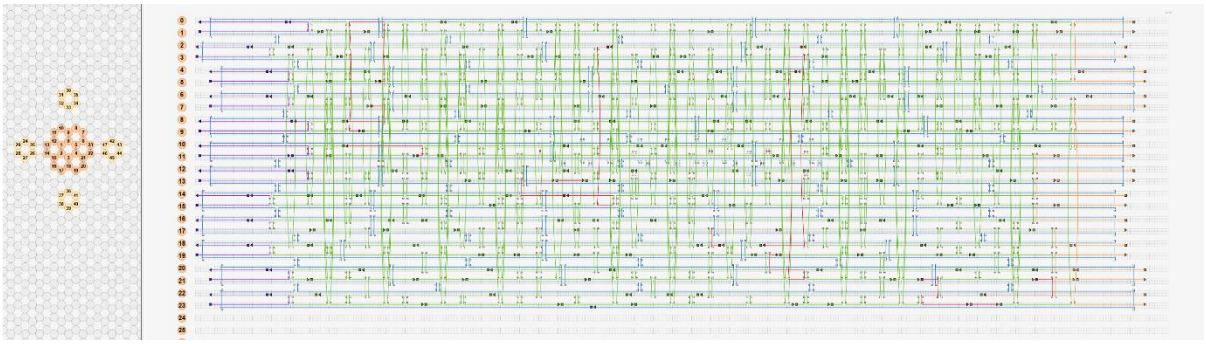

Figure A.2: Cadnano design of the 24 HB monomer. The scaffold strand is depicted in blue, C4 endcaps are depicted in purple (left) and orange (right). Core staples are depicted in green as well as the handle strands for the NPs in red.

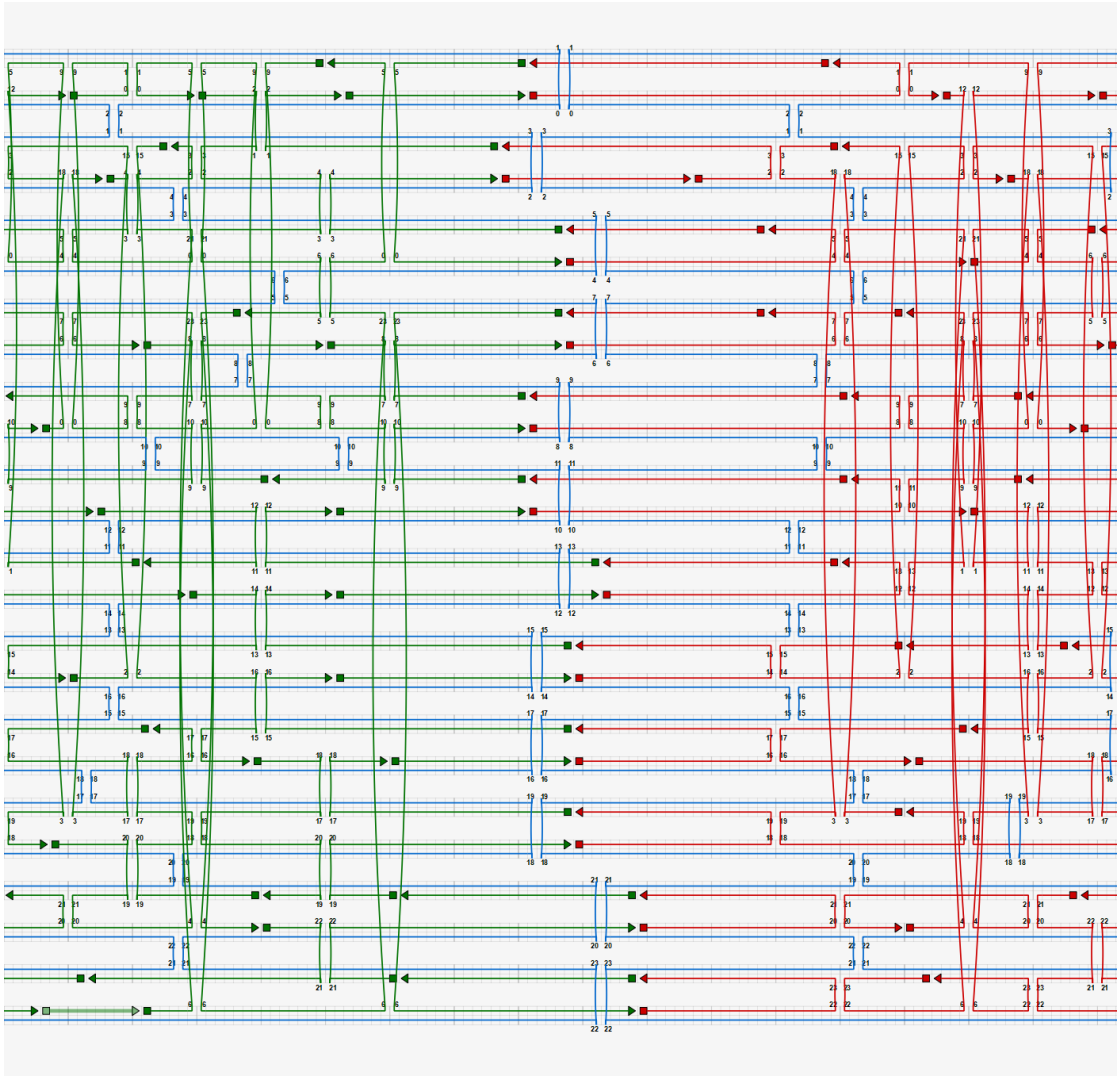

Figure A.3: Cadnano design of 24 HB dimerization mechanism, where the dimerization technique depicted with the individual halfs in green and red.

The Small Pitch Helix (SPH) was formed around a 48 helix bundle (48 HB) DNA origami trunk. This origami was synthesized with a 8064 base pair (bp) scaffold strand and 205 staple strands. To prevent unintentional binding of NPs to the origamis ends, each side has 6 crossbar staple strands that connect helices in a horizontally fashion across the origami end. Gold nanoparticles can be attached to protruding handle strands depicted in red.

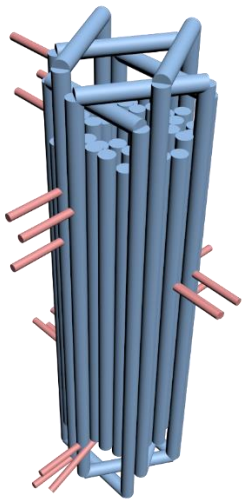

Figure A.4: 3D Model of the DNA origami structure 48 HB with crossbar strands (cylinders represent DNA helices) and handles for nanoparticle attachment depicted in red.

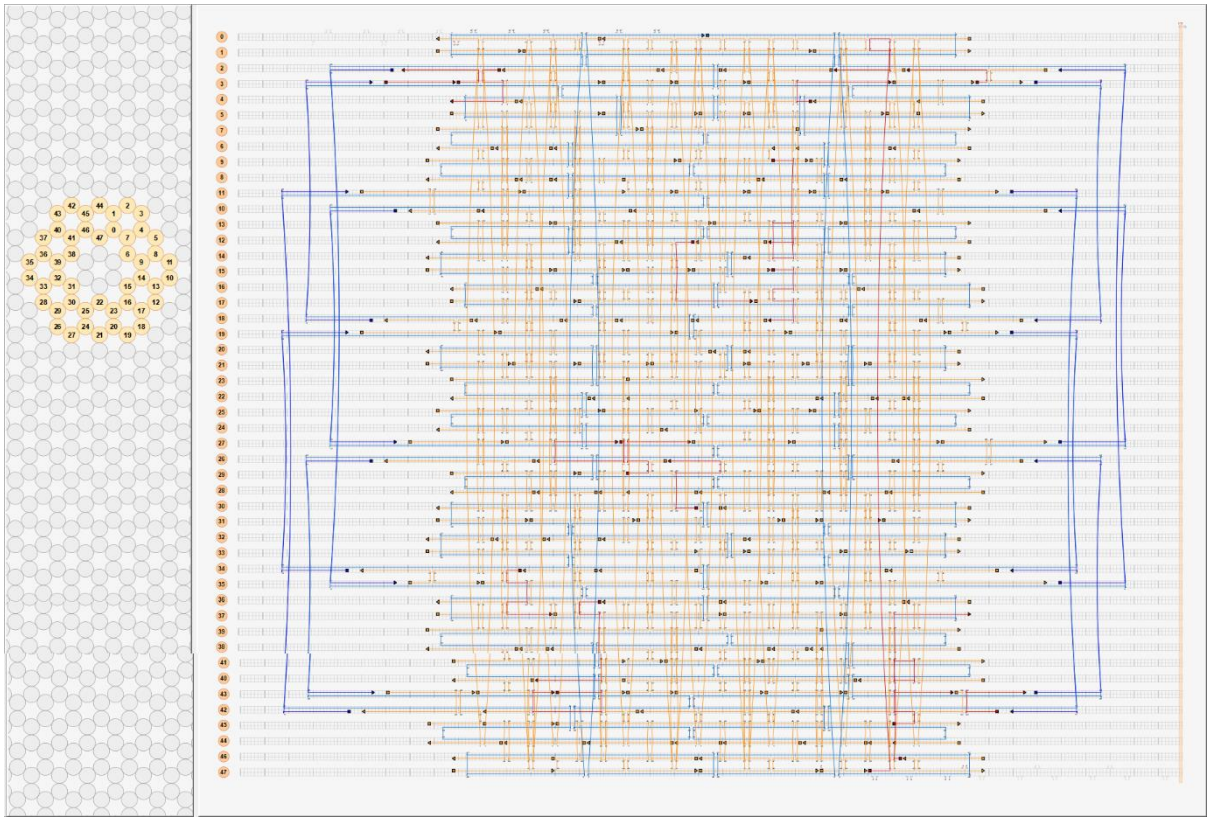

Figure A.5: Cadnano design of the 48 HB monomer, where the scaffold strand is depicted in blue, crossbar staples strands are depicted in purple. Core staples are depicted in orange as well as the handle strands for the NPs in red.

After attachment of 40 nm spherical gold particles to the 24HB the LPH forms a lefthanded helix with an offset of 29 nm and a rotation around the helical axis of 90° per particle. The radius of the helix amounts to 30 nm if measured from the center of particles to the center of the helix. The SPH also forms a lefthanded helix, however, with important geometric differences. The attached gold particles have a diameter of 30 nm, the offset per particle amounts to 11 nm and the radius, measured from the center of the particles to the center of the helix, is 30 nm.

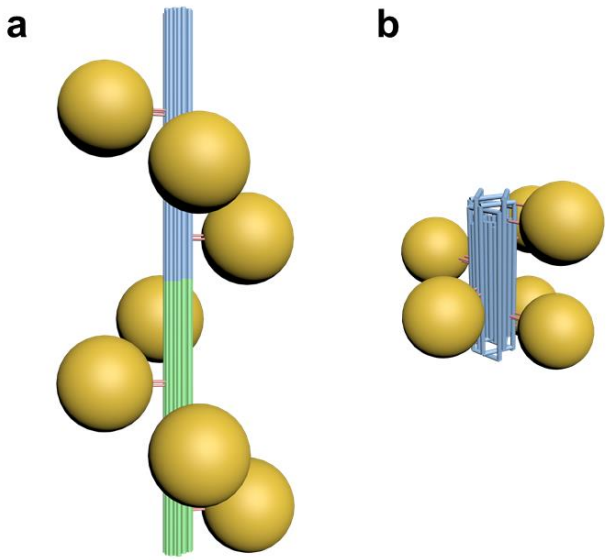

Figure A.6: 3D Model of the complete nanohelix structures. **a**) LPH dimer structure with individual halfs depicted in blue and green and handles for nanoparticle attachment depicted in red. Gold spheres represent 40 nm spherical gold nanoparticles. **b**) SPH structure with 30 nm spherical gold nanoparticles.

Chirality Transfer

The left half of the dimeric origami structure (yellow part in Figure A.7) was folded with an 8064 base pair (bp) scaffold strand and 126 core staple strands as well as 62 “C4 endcap” staples, 22 staples for dimerization and 12 “handle” strands for NP assembly. The right half of the origami structure (blue part in Figure A.7) was folded separately but with the same 8064 bp scaffold strand and a different set of 123 core staple strands as well as 70 C4 endcap staples, 25 staples for dimerization and 11 handle strands for NP assembly.

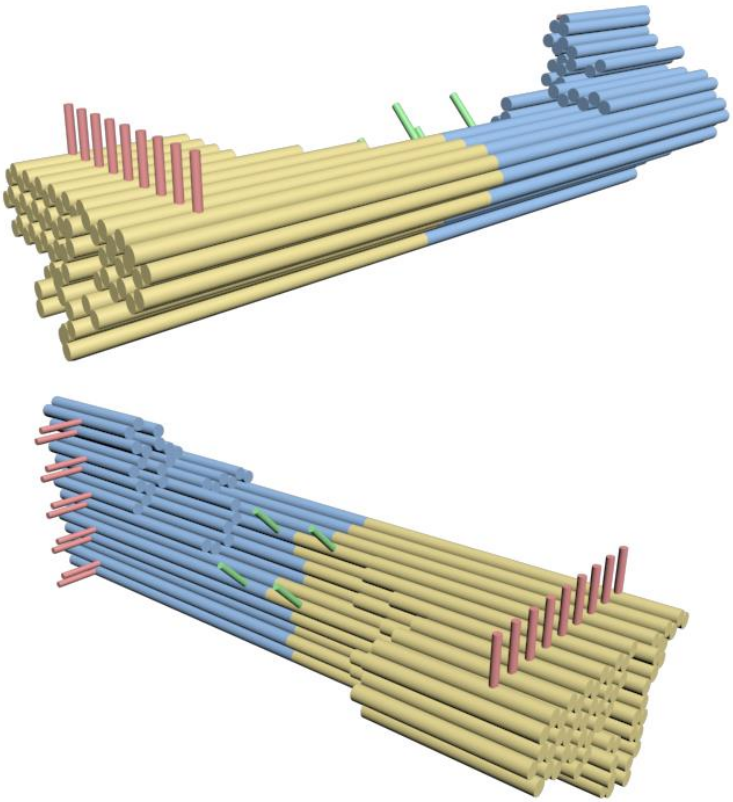

Figure A.7: 3D Model of the Chirality Transfer DNA origami structure, depicting the individual halfs in blue and yellow (cylinders represent DNA helices). The handles for the NS are depicted in green as well as the handles for the NRs in red.

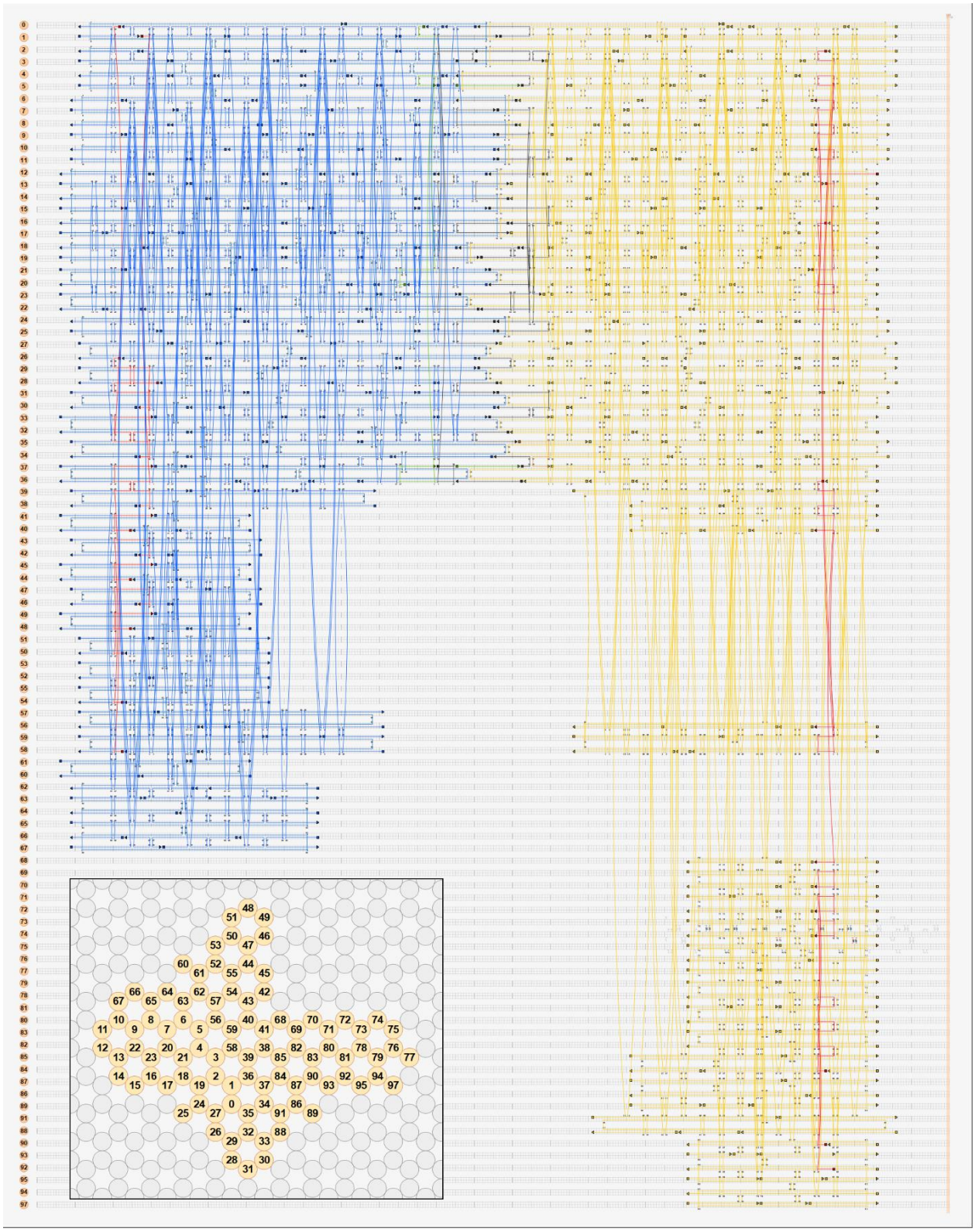

Figure A.8: Cadnano design of the Chirality Transfer DNA origami structure, depicting the individual halves in blue and yellow as well as the handles for the NS in green and the handles for the NRs in red. The staples that connect the individual sides are depicted in black.

Nanowheel

The Nanowheel origami structure was folded with an 8064 base pair (bp) scaffold strand and 185 core staple strands as well as 10 handle strands for NP assembly. C4 endcap strands were added to each side (36 in total), which prevent any further attachment by leaving 4 cytosine bases protruding from the origami structure.

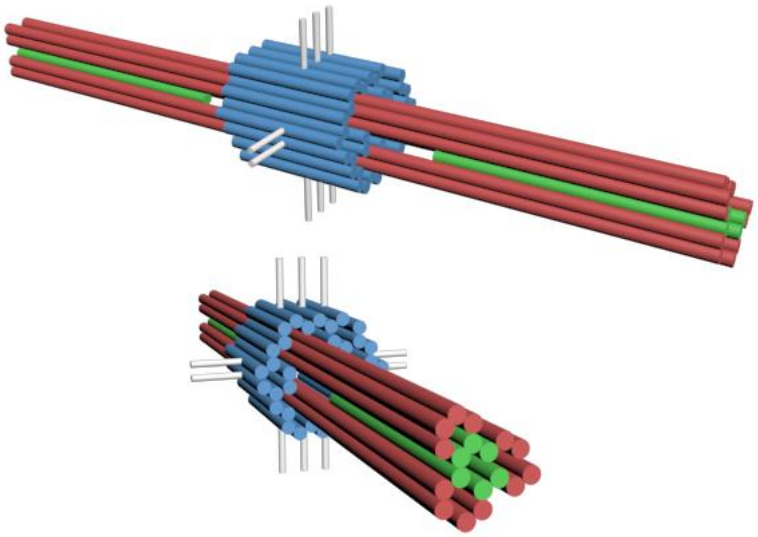

Figure A.9: 3D Model of the Nanowheel DNA origami structure, depicting the long helices in red, the core helices in green and the middle helices in blue (cylinders represent DNA helices). The handles for the NPs are depicted in white.

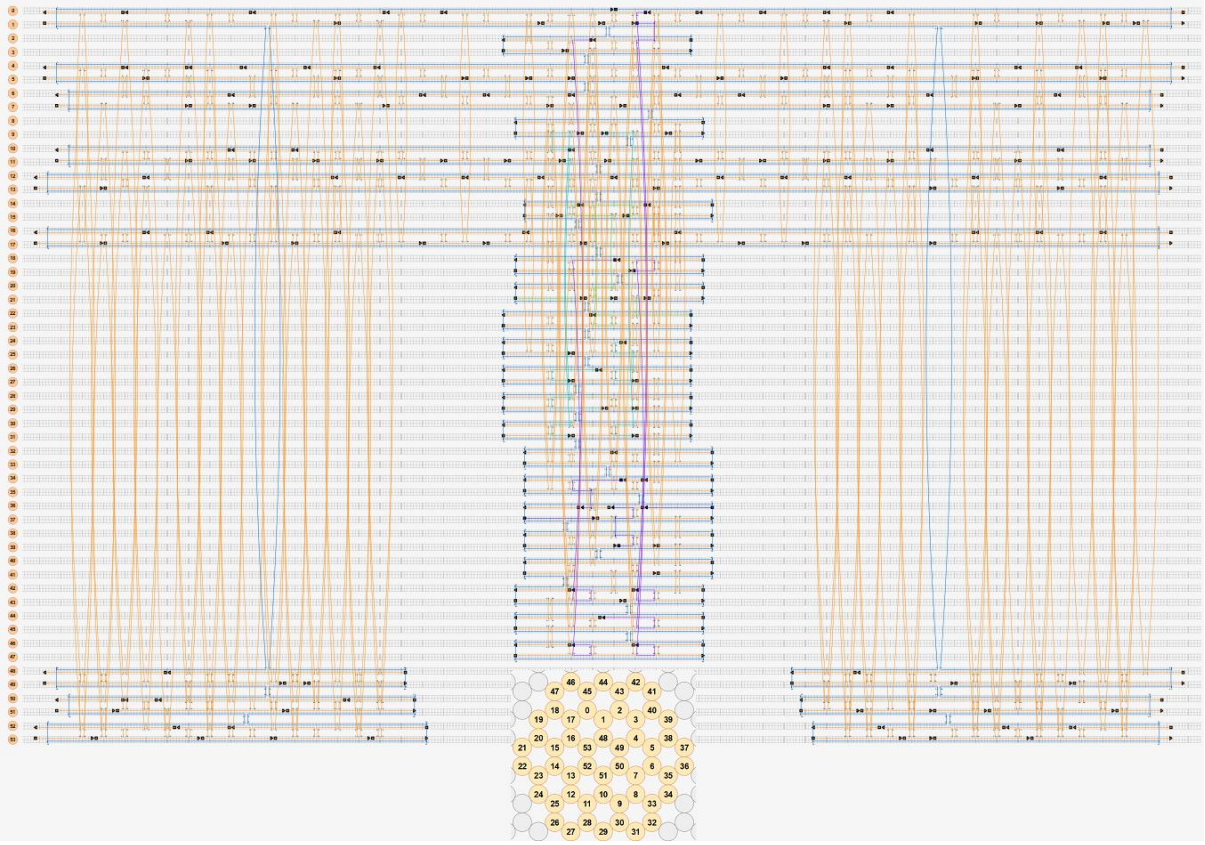

Figure A.10: Cadnano design of the Nanowheel DNA origami structure, depicting the scaffoldin blue and the core staples in yellow. The handles for the NPs are green, blue, purple and turquoise.

A.3 DNA Origami Synthesis

Large Pitch and Small Pitch Helix

The 24 HB for the LPH was folded with a scaffold concentration of 16 nM and 160 nM core and endcap staples as well as 333 nM handle staples. For the dimer version 200 nM dimer staples were used. 1X TE and 24 mM MgCl2 were added as buffer solution. The 48 HB for SPH was folded with a scaffold concentration of 12 nM and 120 nM core staples (including endcaps) as well as 600 nM handle staples. 1X TE and 26 mM MgCl2 were added as buffer solution. Handles were added according to the desired number of gold nanoparticles to be attached in the next step.

The solutions containing the mixtures were heated up to 65°C and then cooled down to room temperature over the course of 24 h. Origamis were purified using gel electrophoresis with 0.7% agarose gel in a buffer of 1X TAE, 11 mM MgCl2 and 0.05‰ Roti Stain as intercalating dye. The gel was run for 2.5 h at 70 V, before the origami dimer band was cut out under UV light and afterwards squeezed to redisperse the sample in buffer. For the dimer version, the left side of the origami and the right side were combined in equal amounts and left to dimerize over 24 h.

For TEM analysis, samples were incubated for 15 min on copper grids (Ted Pella Inc., Redding, USA) before being dabbed off with a filter paper and subsequently stained with 2% uranyl format in two steps. In the first step the uranyl format solution only quickly washes the grid, in the second step it is left to incubate for 15 s before being dabbed off. Images were taken with a JEOL JEM 1011 electron microscope at 80 kV.

Table A.1: Monomer 24 HB DNA origami protocol

Component	Concentration	Amount	End Concentration
Scaffold 8064	100 nM	16 µL	16 nM
Core Staples	320.5 nM	49.9 µL	160 nM
Endcap Staples L	2083.3 nM	9.6 µL	160 nM
Endcap Staples R	2380.9 nM	8.4 µL	160 nM
Handles	16 666.7 nM	2 µL each	333 nM
TE	20X	5 µL	1 X
MgCl2	1 M	2.4 µL	24 mM
H2O	-	0.7-6.7 µL	-
Total		100 µL	16 nM

Table A.2: Left side dimer 24 HB DNA origami protocol

Component	Concentration	Amount	End Concentration
Scaffold 8064	100 nM	16 µL	16 nM
Core Staples	320.5 nM	49.9 µL	160 nM
Endcap Staples L	2083.3 nM	9.6 µL	160 nM
Dimer Staples	2631.6 nM	7.6 µL	200 nM
Handles	16666.7 nM	2 µL each	333 nM
TE	20X	5 µL	1 X
MgCl2	1 M	2.4 µL	24 mM
H2O	-	1.5-7.5 µL	-
Total		100 µL	16 nM

Table A.3: Right side dimere 24 HB DNA origami protocol

Component	Concentration	Amount	End Concentration
Scaffold 8064	100 nM	16 µL	16 nM
Core Staples	320.5 nM	49.9 µL	160 nM
Endcap Staples R	2380.9 nM	8.4 µL	160 nM
Dimer Staples	2631.6 nM	7.6 µL	200 nM
Handles	16666.7 nM	2 µL each	333 nM
TE	20X	5 µL	1 X
MgCl2	1 M	2.4 µL	24 mM
H2O	-	2.7-8.7 µL	-
Total		100 µL	16 nM

Table A.4: Monomer 48 HB DNA origami protocol

Component	Concentration	Amount	End Concentration
Scaffold 8064	100 nM	12 µL	12 nM
Staples	244 nM	49.2 µL	120 nM
Handles	16666.7 nM	3.6 µL each	600 nM
TE	20X	5 µL	1 X
MgCl2	1 M	2.6 µL	26 mM
H2O	-	9.6-27.6 µL	-
Total		100 µL	12 nM

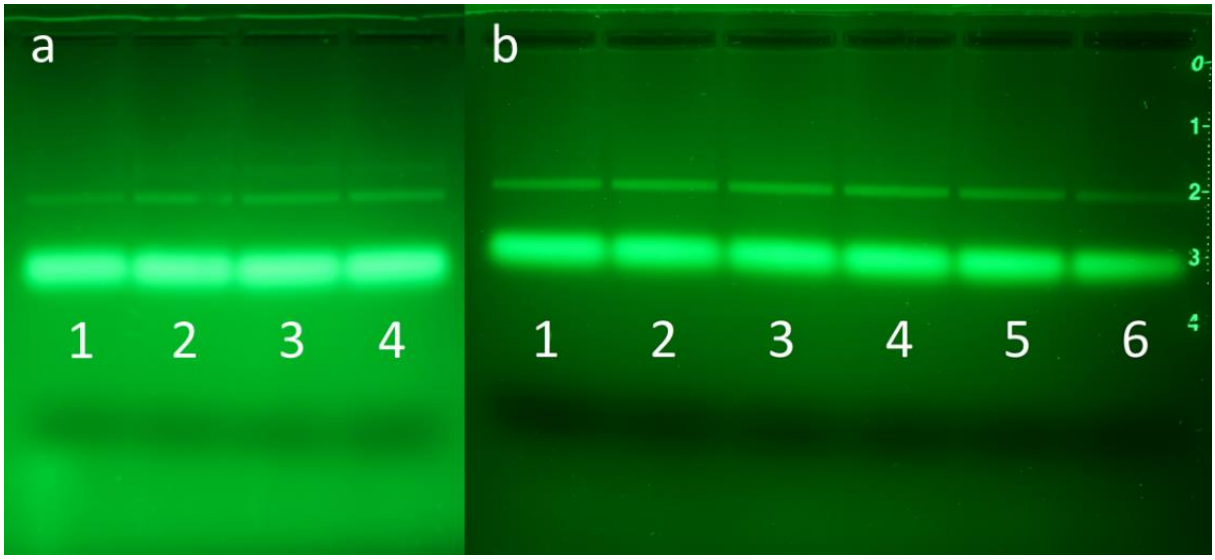

Figure A.11: DNA origami gel electrophoresis bands showing **a**) 24 HB monomers and **b**) 48 HB monomers with different numbers of handles for nanoparticles (1-4 for 24 HB and 1-6 for 48 HB). Gel electrophoresis was performed for 2.5 hours at 70 V, showing a band of DNA origami structure after folding (upper band) and a band of excessive staples (lower band).

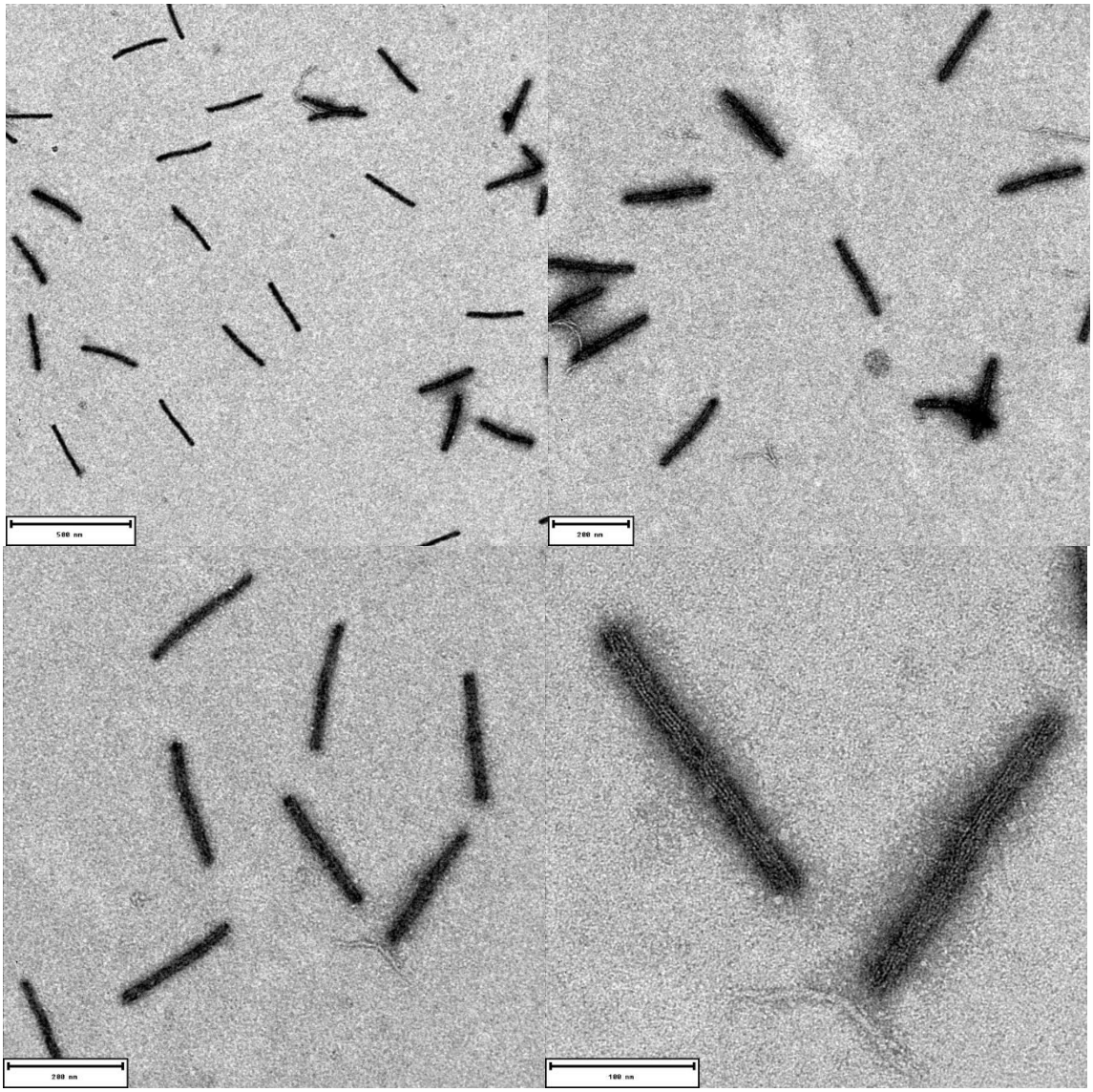

Figure A.12: Electron micrographs of 24 HB dimers. The DNA origami were purified using gel electrophoresis purification and imaged with transmission electron microscopy using uranyl format for staining. Scale bars: 500 nm, 200 nm, 200 nm and 100 nm

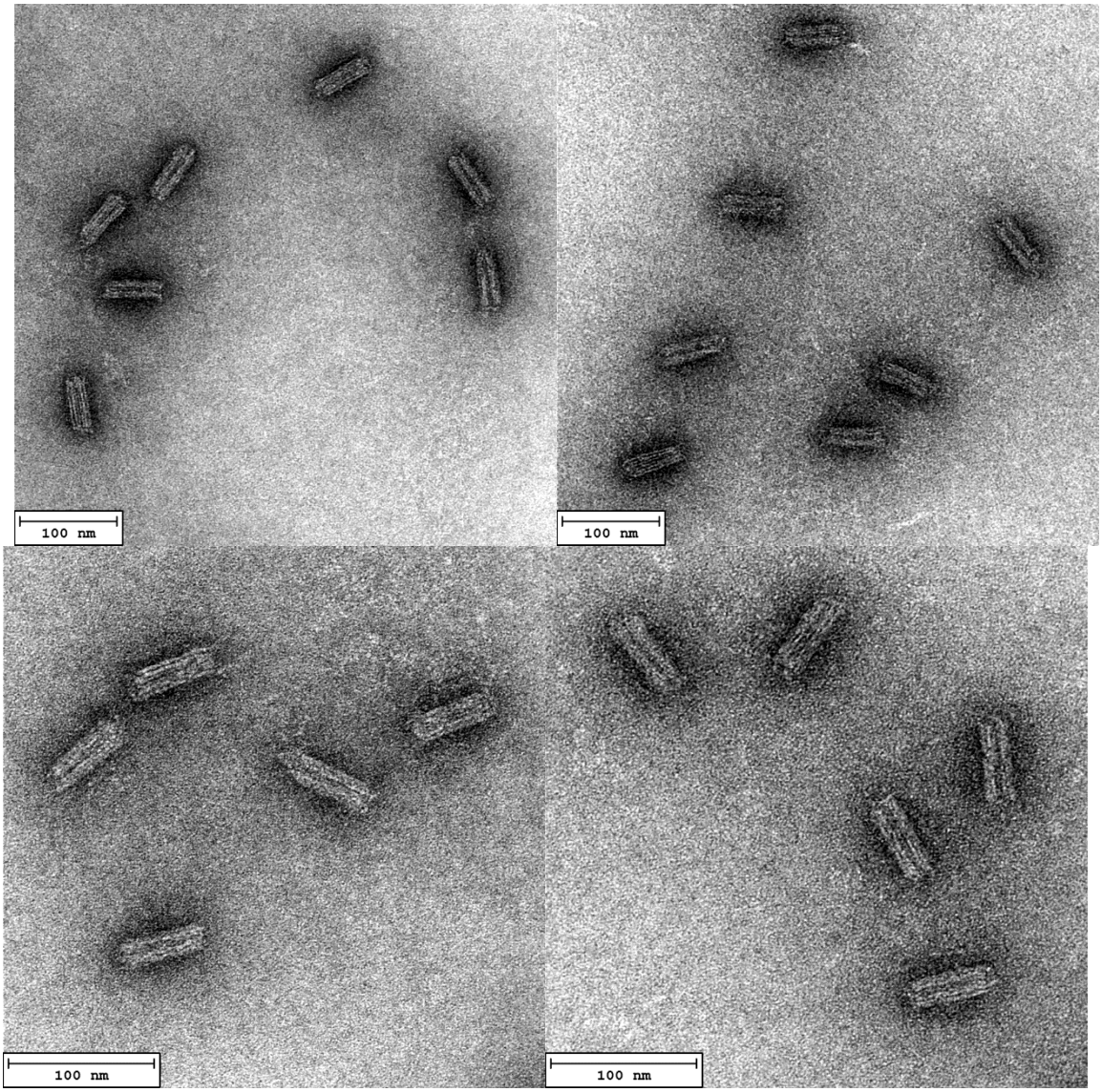

Figure A.13: Electron micrographs of 48 HB monomers. The DNA origami were purified using gel electrophoresis purification and imaged with transmission electron microscopy using uranyl format for staining. Scale bar: 100 nm.

Chirality Transfer

The scaffold was used during folding at a concentration of 16 nM with 160 nM core and endcap staples plus 200 nM dimer and handle staples. 1X TE and 28 mM MgCl2 were added as buffer solution. The two solutions containing the two mixtures were heated up to 65°C and then cooled down to room temperature over the course of 24 h. Subsequently the left side of the origami and the right side were combined in equal amounts and left to dimerize over 48 h. Dimer origamis were purified using gel electrophoresis with 0.7% agarose gel in a buffer of 1X TAE, 11 mM MgCl2 and 0.05‰ Roti Stain as intercalating dye. The gel was run for 2.5 h at 70 V, before the origami dimer band was cut out under UV light and afterwards squeezed to redisperse the sample in buffer.

Table A.5: Left half DNA origami protocol.

Component	Concentration	Amount	End Concentration
Scaffold 8064	100 nM	16 µL	16 nM
Core Staples	397 nM	40.3 µL	160 nM
Endcap Staples	806 nM	19.9 µL	160 nM
Dimere Staples	2273 nM	8.8 µL	200 nM
Handles	4167 nM	4.8 µL	200 nM
TE	20X	5 µL	1X
MgCl2	1 M	2.8 µL	28 mM
H2O	-	2.4 µL	-
Total		100 µL	16 nM

Table A.6: Right half DNA origami protocol.

Component	Concentration	Amount	End Concentration
Scaffold 8064	100 nM	16 µL	16 nM
Core Staples	407 nM	39.3 µL	160 nM
Endcap Staples	714 nM	22.4 µL	160 nM
Dimere Staples	2000 nM	10 µL	200 nM
Handles	4545 nM	4.4 µL	200 nM
TE	20X	5 µL	1X
MgCl2	1 M	2.8 µL	28 mM
H2O	-	0.1 µL	-
Total		100 µL	16 nM

For TEM analysis, samples were incubated for 15 min on copper grids (Ted Pella Inc., Redding, USA) before being dabbed off with a filter paper and subsequently stained with 2% uranyl format in two steps. In the first step the uranyl format solution only quickly washes the grid, in the second step it is left to incubate for 15 s before being dabbed off. Images were taken with a JEOL JEM 1011 electron microscope at 80 kV.

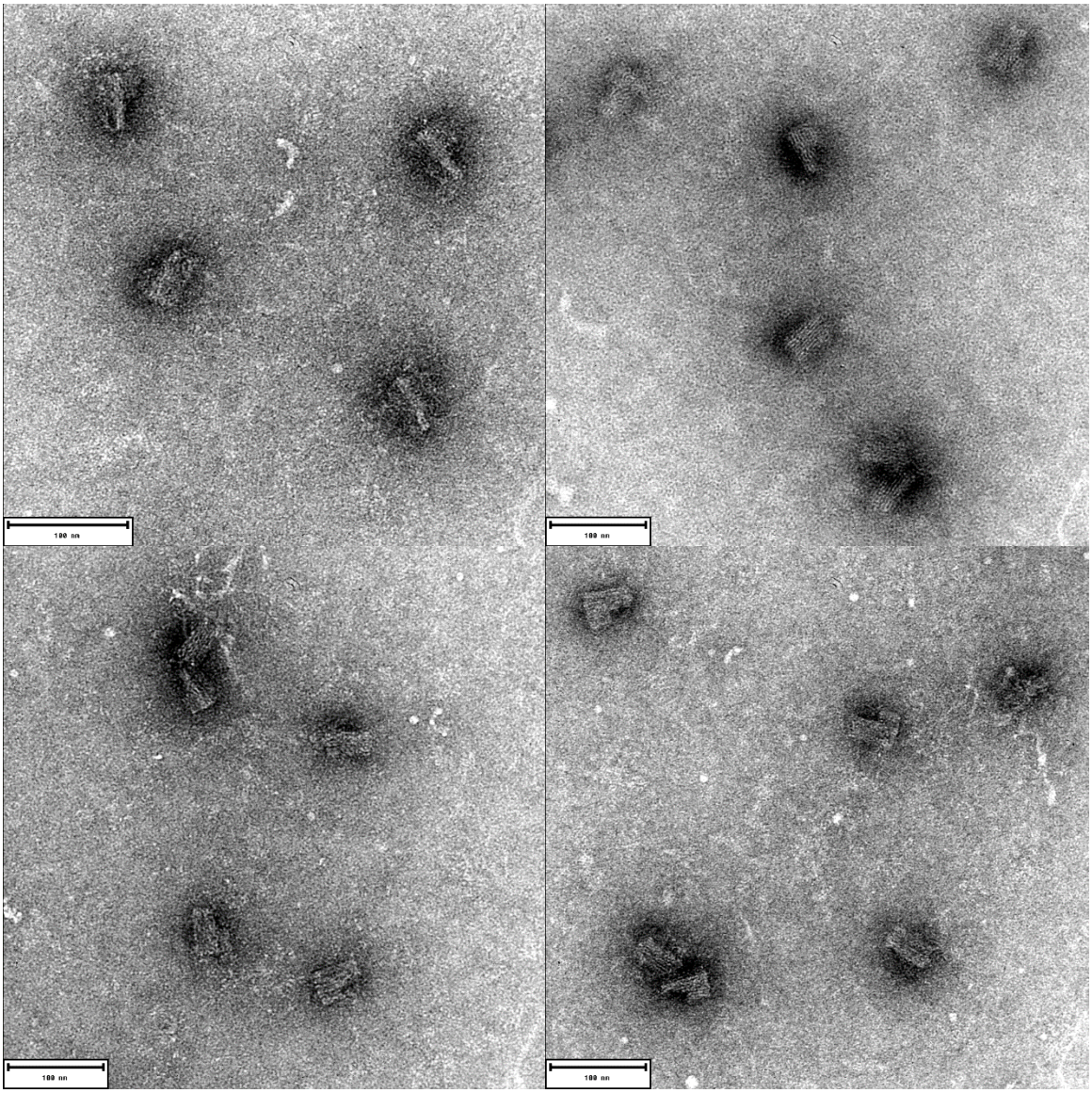

Figure A.14: Electron micrographs of the left half of the Chirality Transfer DNA origami after gel electrophoresis purification. Scale bar: 100 nm.

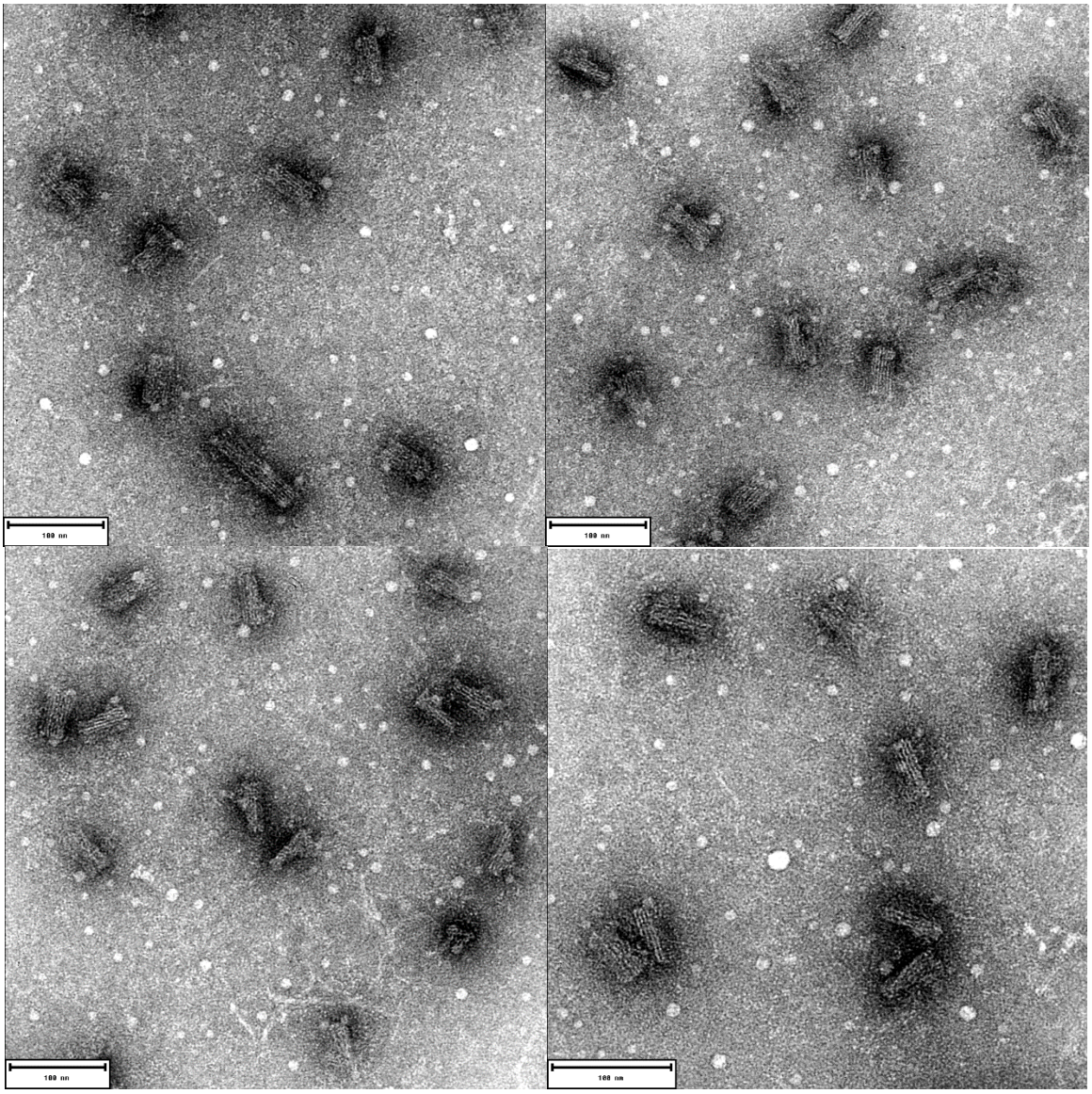

Figure A.15: Electron micrographs of the right half of the Chirality Transfer DNA origami after gel electrophoresis purification. Scale bar: 100 nm.

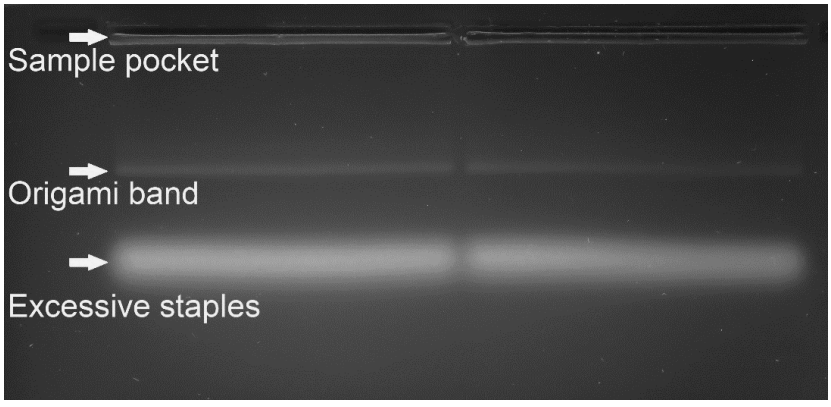

Figure A.16: Gel electrophoresis band of the Chirality Transfer DNA origami structure after dimerization

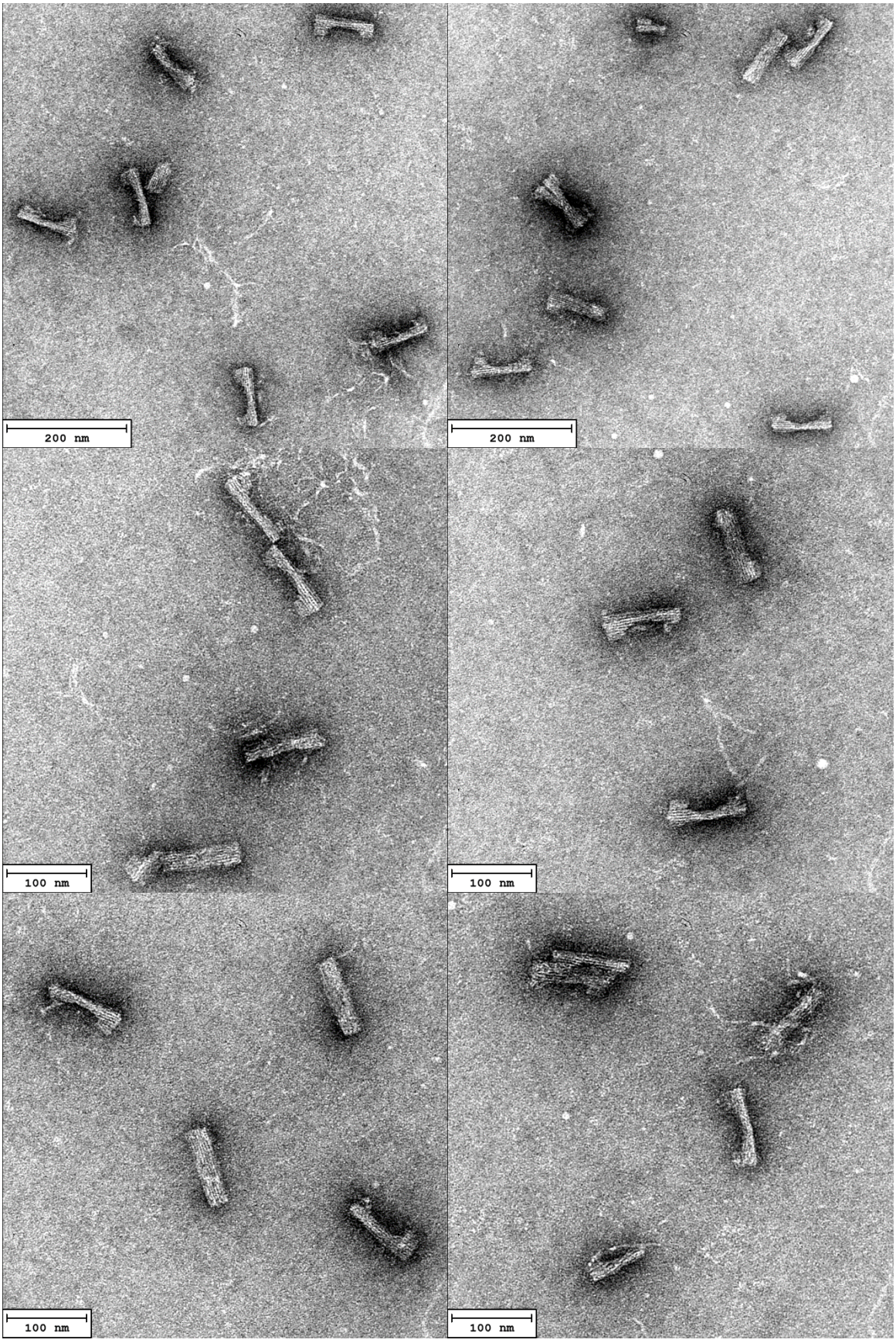

Figure A.17: Electron micrographs of the complete Chirality Transfer DNA origami structure (purified)

Nanowheel

The scaffold was used during folding at a concentration of 15.8 nM with 156 nM core and endcap staples. 1X TE and 18 mM MgCl2 were added as buffer solution. The two solutions containing the two mixtures were heated up to 65°C and then cooled down to room temperature over the course of 24 h. The origamis were purified using gel electrophoresis with 0.7% agarose gel in a buffer of 1X TAE, 11 mM MgCl2 and 0.05‰ Roti Stain as intercalating dye. The gel was run for 2.5 h at 70 V, before the origami dimer band was cut out under UV light and afterwards squeezed to redisperse the sample in buffer.

Table A.7: Nanowheel DNA origami protocol.

Component	Concentration	Amount	End Concentration
Scaffold 8064	100 nM	15.8 µL	15.8 nM
Core Staples	216 nM	72.4 µL	156 nM
TE	10X	10 µL	1X
MgCl2	1 M	1.8 µL	18 mM
Total		100 µL	15.8 nM

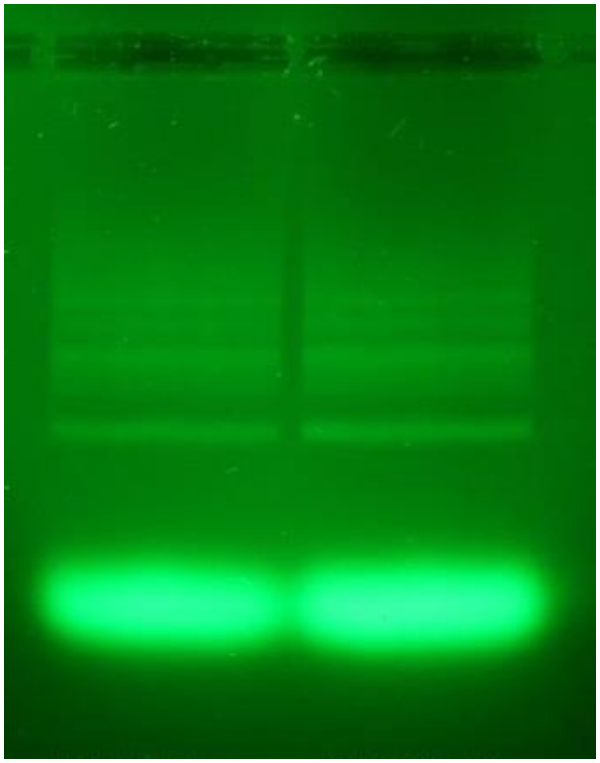

Figure A.18: Gel electrophoresis band of the Nanowheel DNA origami structure after dimerization

For TEM analysis, samples were incubated for 15 min on copper grids (Ted Pella Inc., Redding, USA) before being dabbed off with a filter paper and subsequently stained with 2% uranyl format in two steps. In the first step the uranyl format solution only quickly washes the grid, in the second step it is left to incubate for 15 s before being dabbed off. Images were taken with a JEOL JEM 1011 electron microscope at 80 kV.

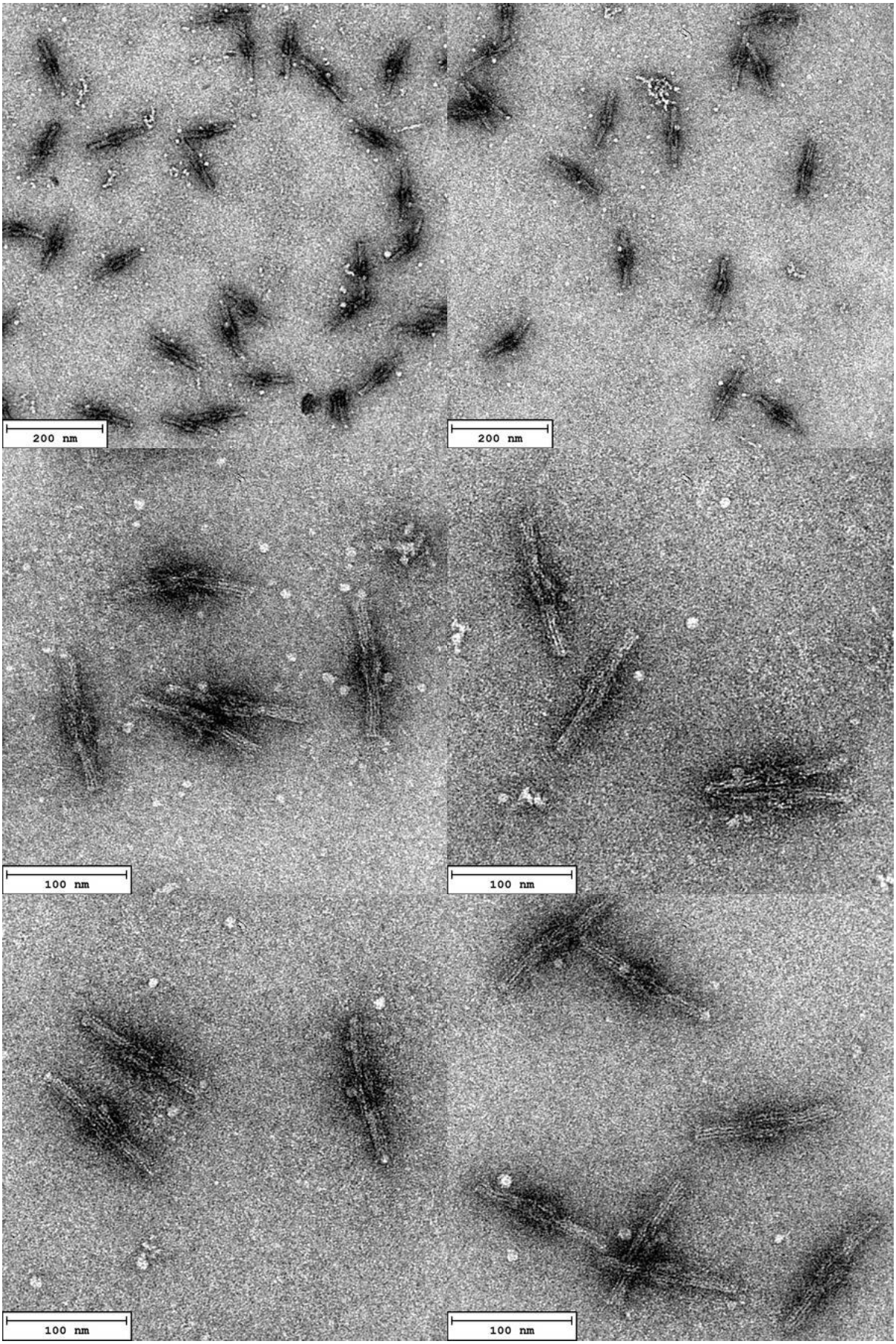

Figure A.19: Electron micrographs of Nanowheel DNA origami structure (purified)

A.4 DNA Origami Nanoparticles Assembly Sythesis

Large Pitch and Small Pitch Helix

30 nm (SPH) and 40 nm (LPH) gold nanoparticles were incubated at an optical density (OD) of 4 with 10 mM thiol-modified DNA oligonucleotides, previously activated with TCEP, and 0.02% SDS. Samples were frozen, thawed and purified using gel electrophoresis with a 0.7% agarose gel in a buffer of 1X TAE, 11 mM MgCl2, run for 1.5 h at 120 V. Subsequently the correct monomer bands were cut and squeezed to redisperse in buffer.

For the synthesis of the LPH and SPH samples, gold nanoparticles were added to the origami structures in a ratio of 5:1 for each particle in a buffer of 1X TAE, 11 mM MgCl2 plus 500 mM NaCl and incubated for between 1 and 24 h. The samples were purified using gel electrophoresis with a 1.5% agarose gel in a buffer of 1X TAE, 11 mM MgCl2, run for 4-6 h at 70 V. The different bands of fully formed structures were cut out and squeezed and analyzed by TEM.

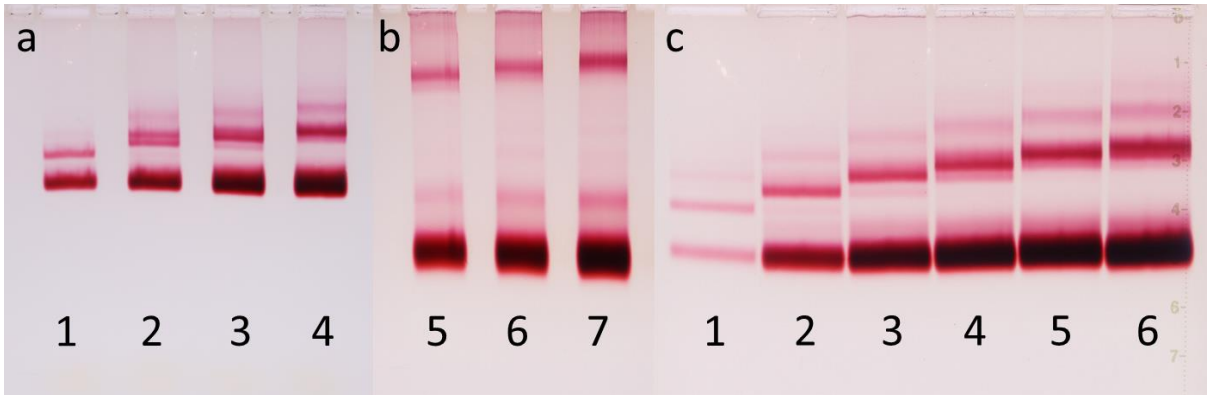

Figure A.20: Nanostructure gel electrophoresis bands showing **a**) LPH-i to LPH-iv **b**) LPH-v to LPH-vii and **c**) SPH-i to SPH-vi. Gel electrophoresis was performed for 3 hours (a), 6 hours (b) and 3 hours (c) at 70 V, showing bands of origami structures with different numbers of gold nanoparticles attached (upper bands) and a thicker band of excessive gold nanoparticles (lower band).

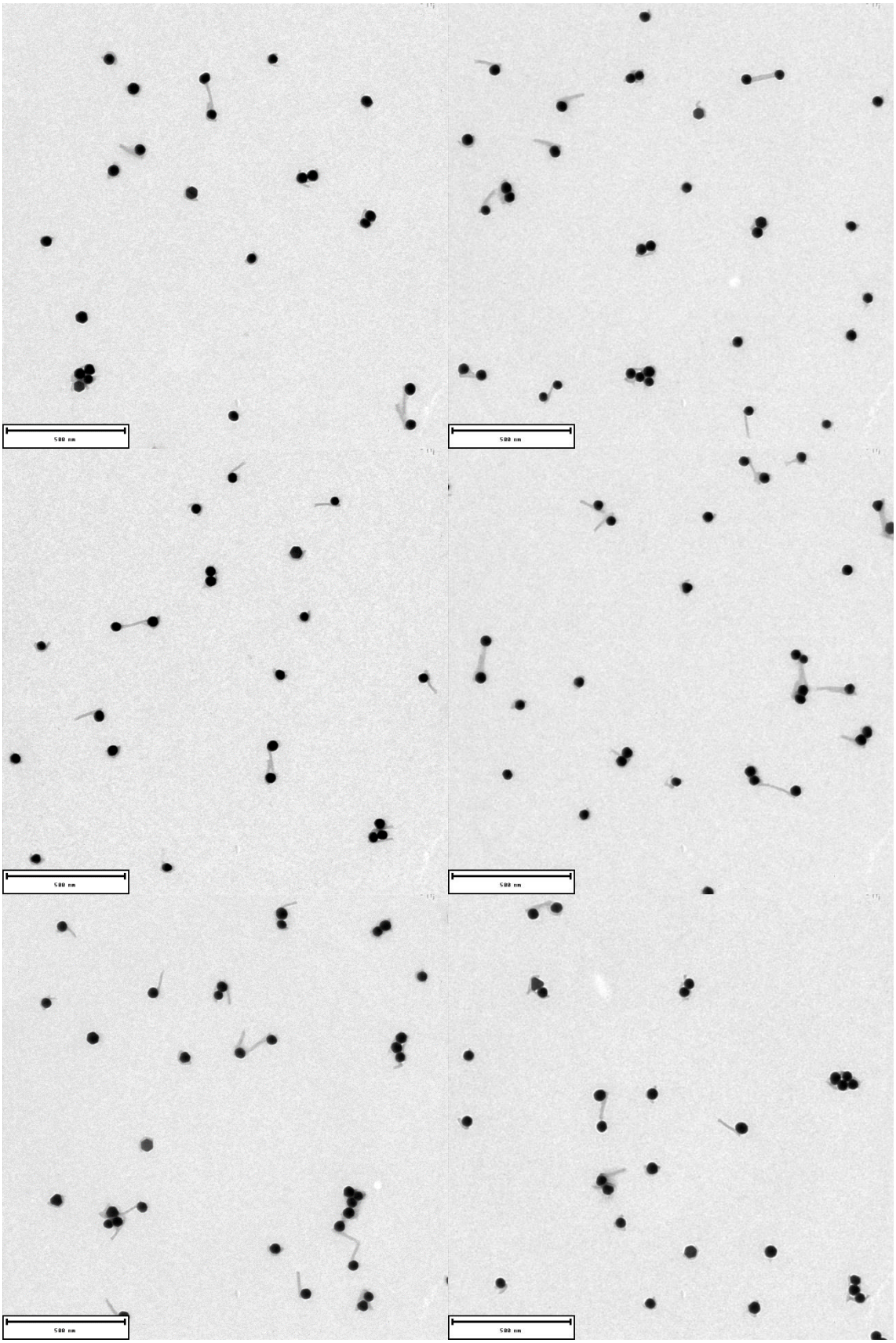

Figure A.21: Electron micrographs of LPH-i. The structures were purified using gel electrophoresis purification and imaged with transmission electron microscopy using uranyl format for staining. Scale bar: 500nm.

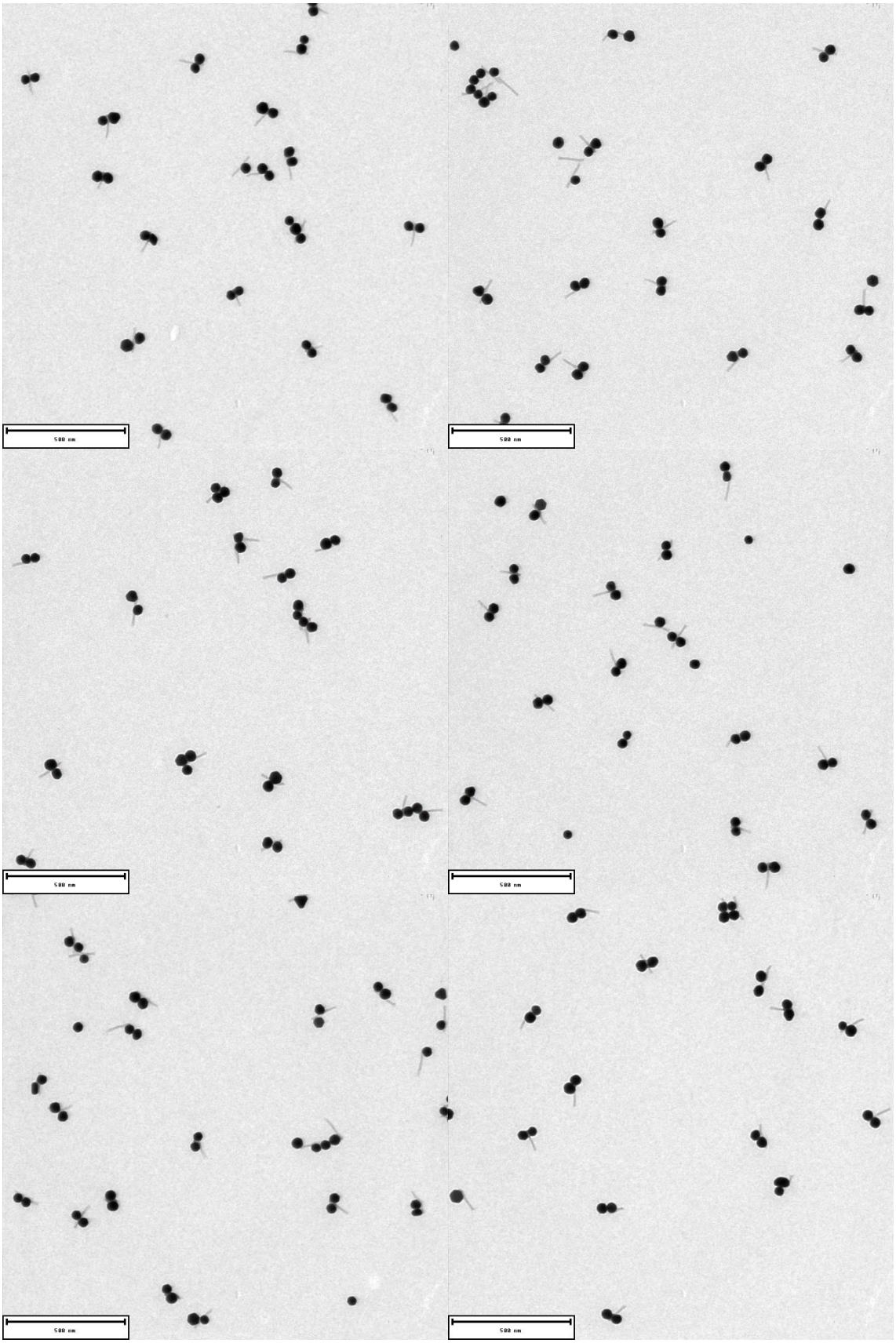

Figure A.22: Electron micrographs of LPH-ii. The structures were purified using gel electrophoresis purification and imaged with transmission electron microscopy using uranyl format for staining. Scale bar: 500nm.

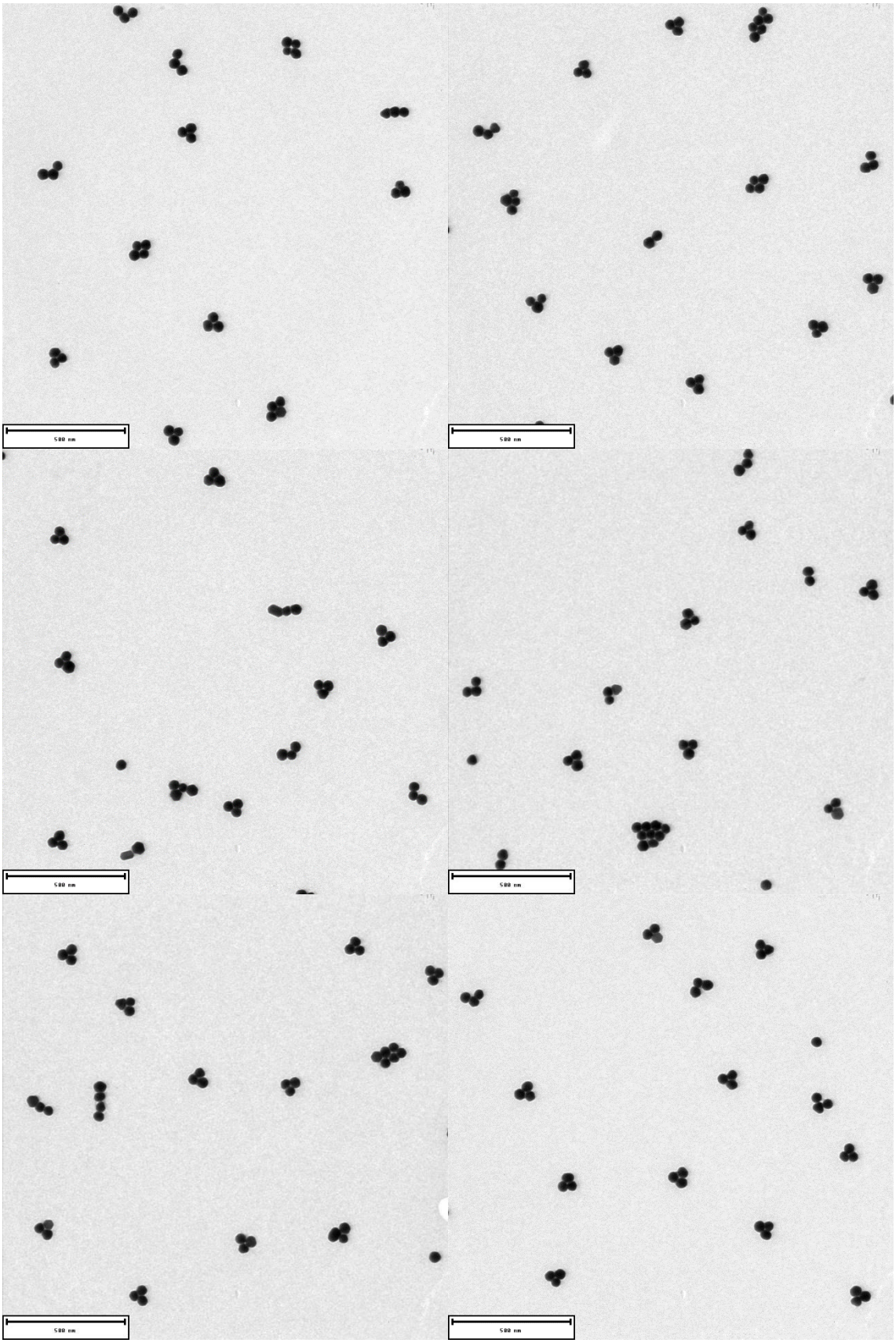

Figure A.23: Electron micrographs of LPH-iii. The structures were purified using gel electrophoresis purification and imaged with transmission electron microscopy using uranyl format for staining. Scale bar: 500nm.

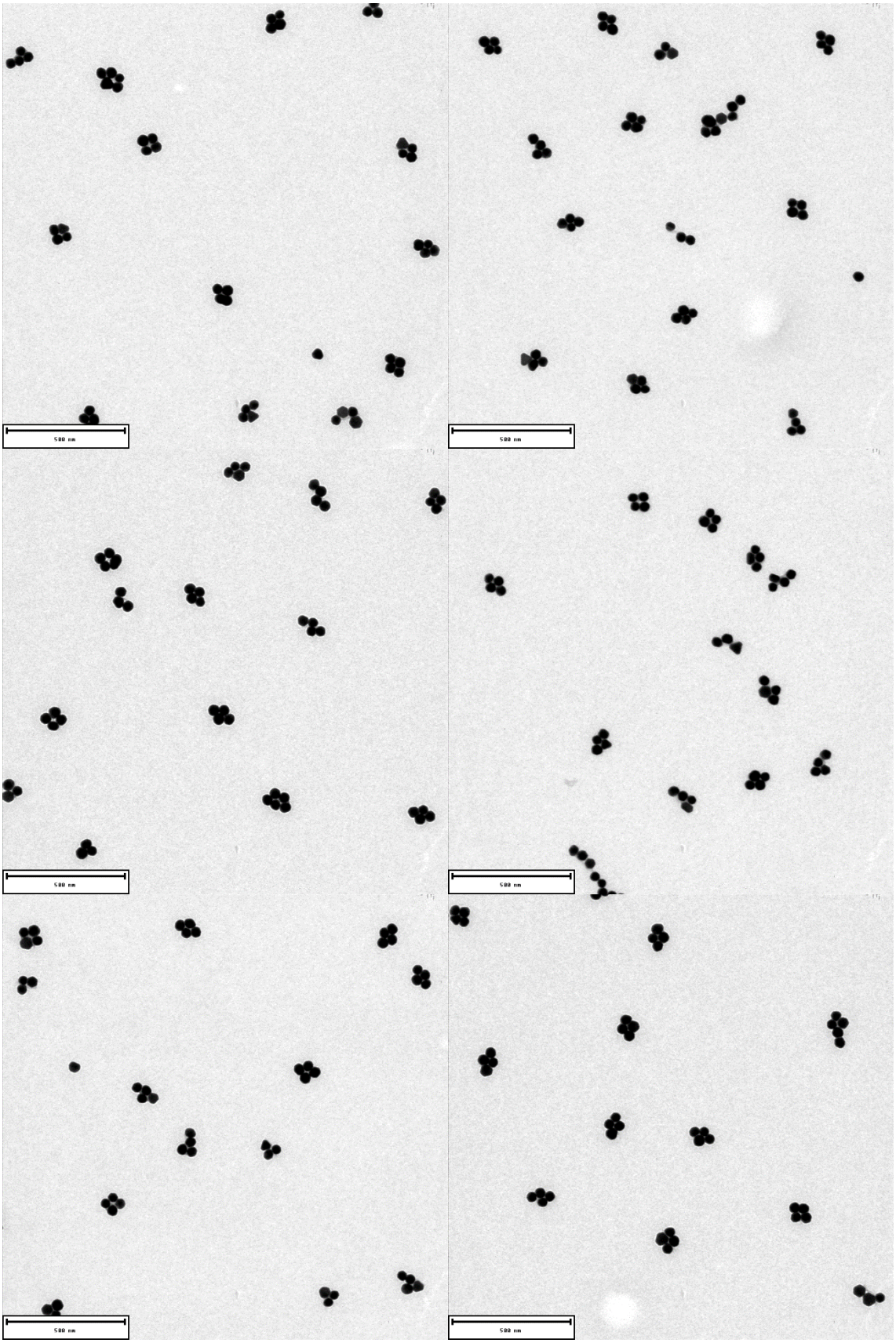

Figure A.24: Electron micrographs of LPH-iv. The structures were purified using gel electrophoresis purification and imaged with transmission electron microscopy using uranyl format for staining. Scale bar: 500nm.

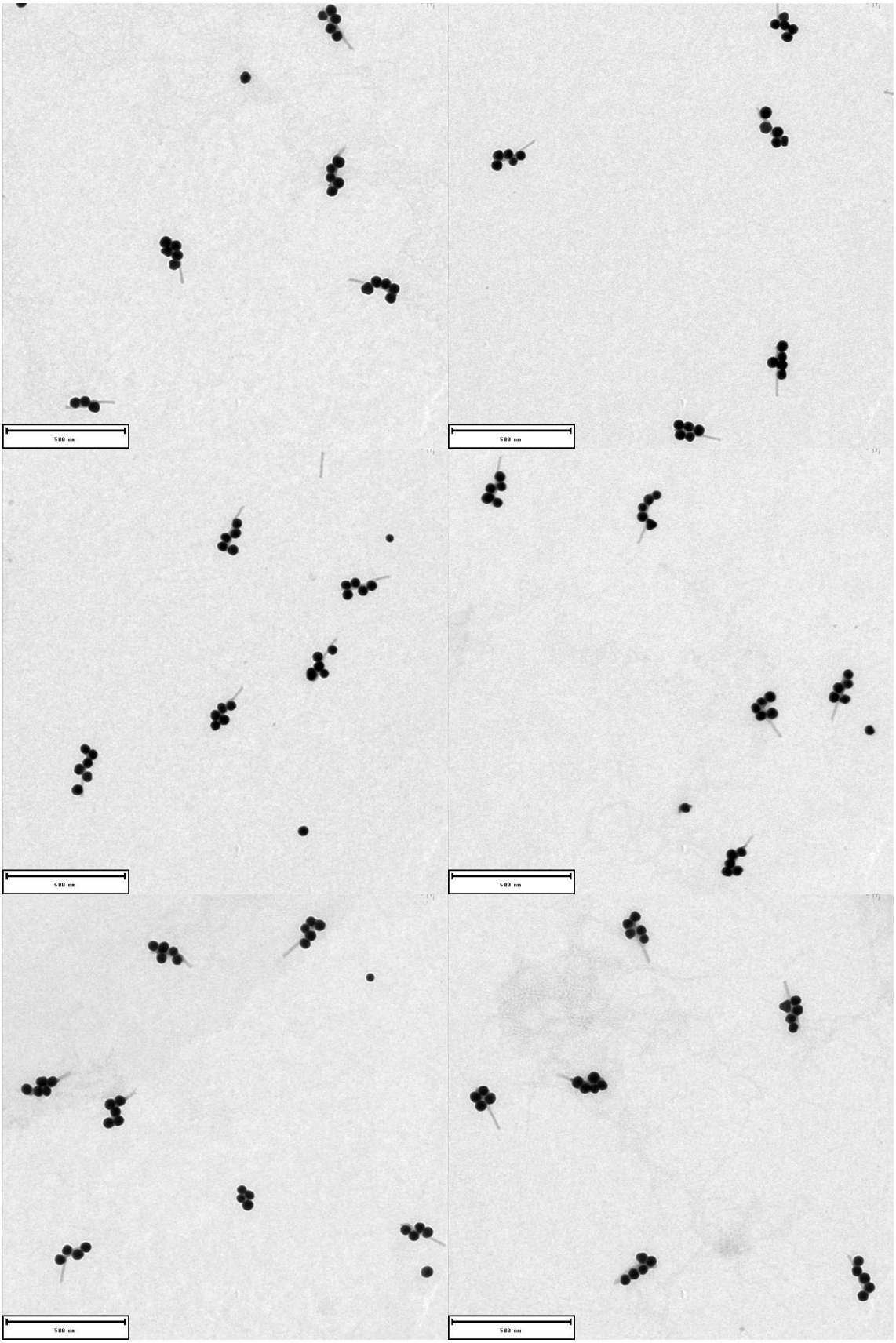

Figure A.25: Electron micrographs of LPH-v. The structures were purified using gel electrophoresis purification and imaged with transmission electron microscopy using uranyl format for staining. Scale bar: 500nm.

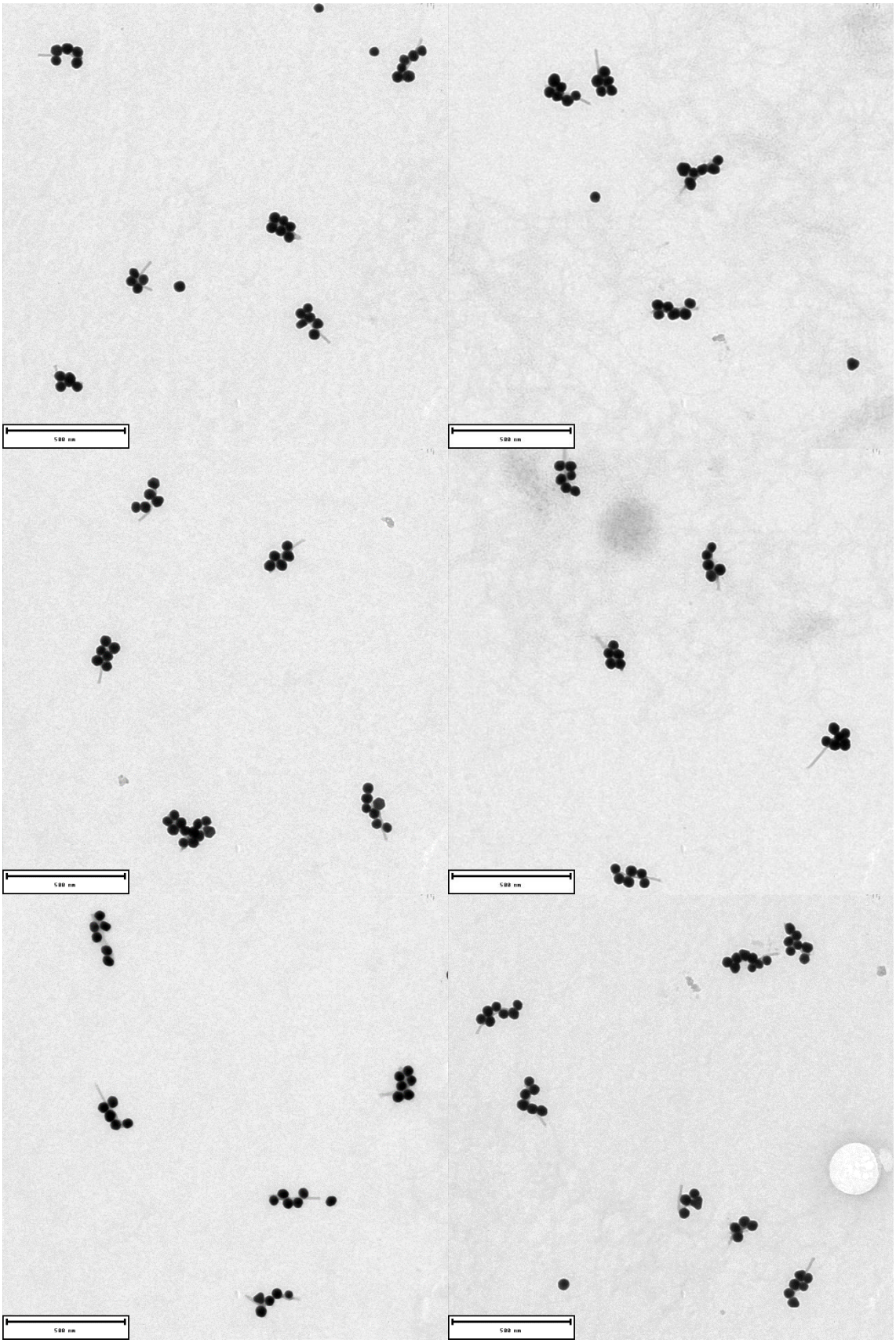

Figure A.26: Electron micrographs of LPH-vi. The structures were purified using gel electrophoresis purification and imaged with transmission electron microscopy using uranyl format for staining. Scale bar: 500nm.

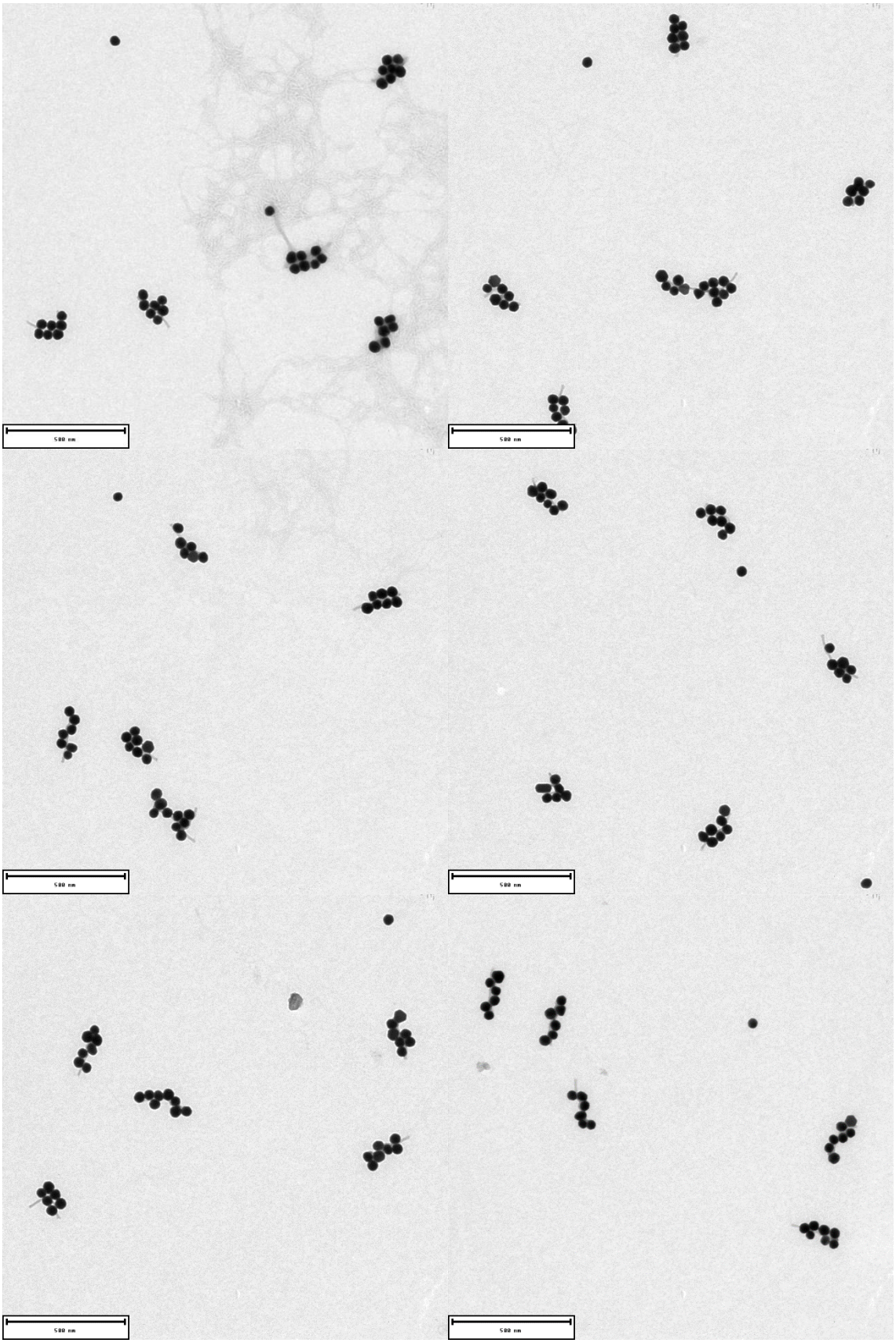

Figure A.27: Electron micrographs of LPH-vii. The structures were purified using gel electrophoresis purification and imaged with transmission electron microscopy using uranyl format for staining. Scale bar: 500nm.

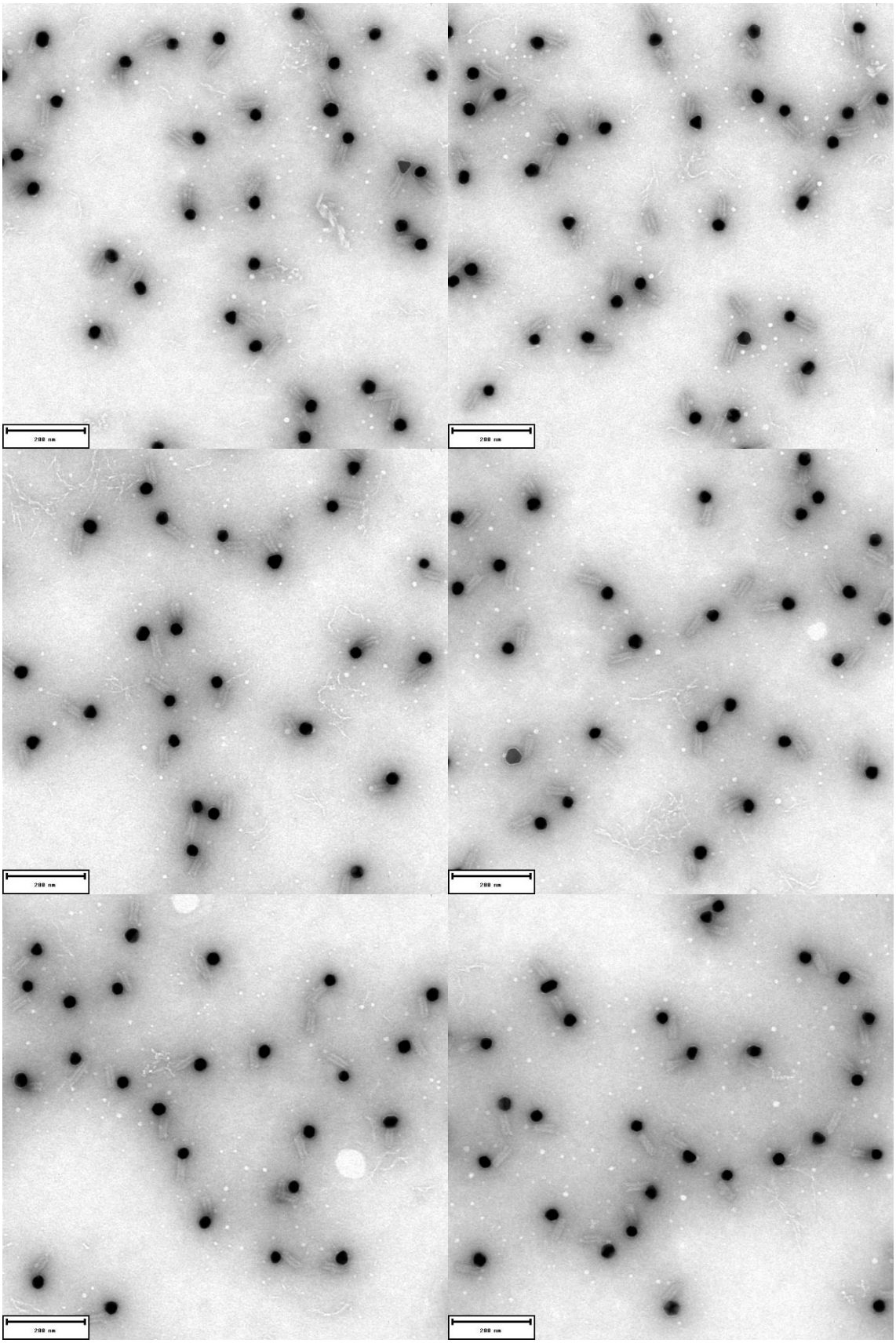

Figure A.28: Electron micrographs of SPH-i. The structures were purified using gel electrophoresis purification and imaged with transmission electron microscopy using uranyl format for staining. Scale bar: 200 nm.

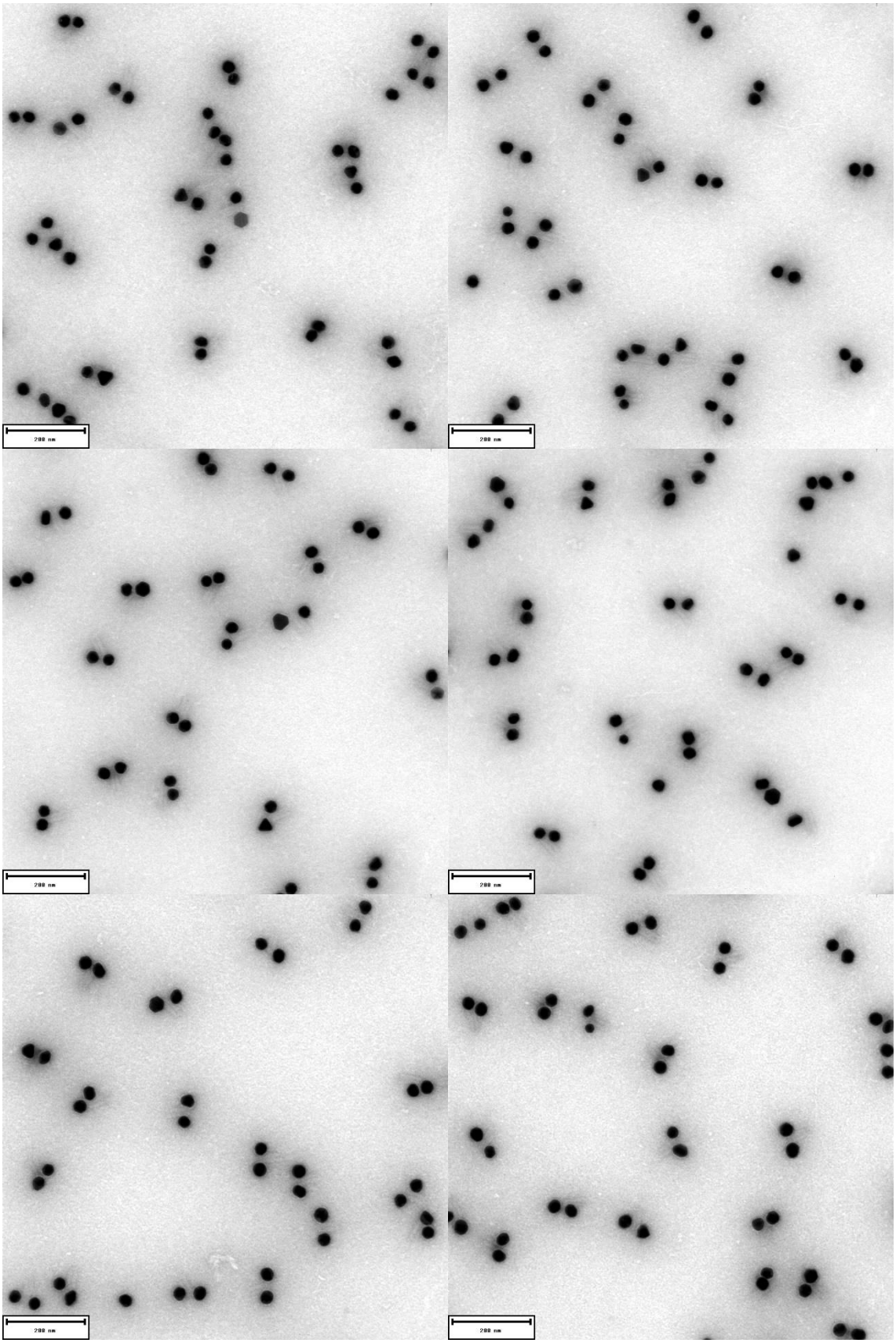

Figure A.29: Electron micrographs of SPH-ii. The structures were purified using gel electrophoresis purification and imaged with transmission electron microscopy using uranyl format for staining. Scale bar: 200 nm.

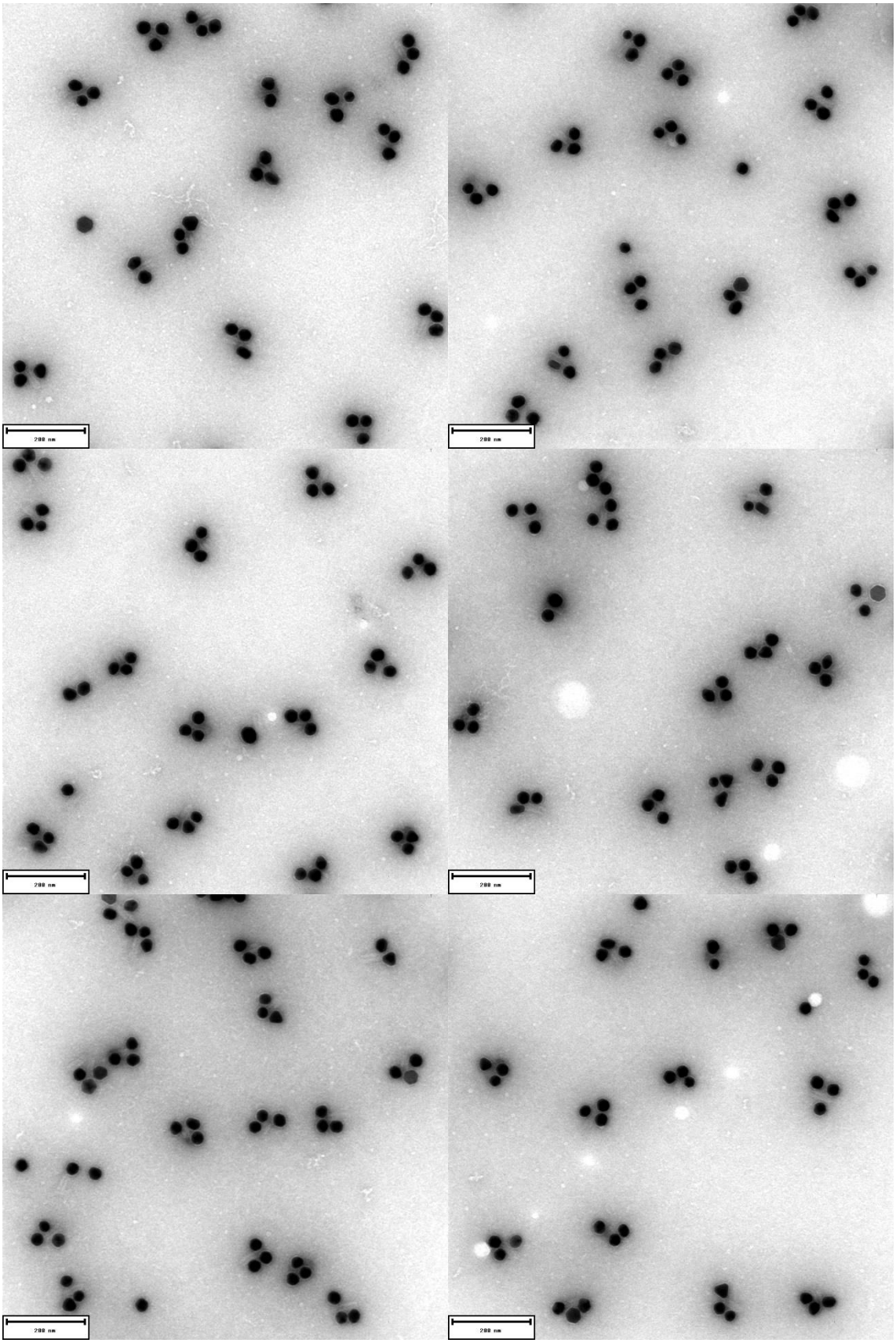

Figure A.30: Electron micrographs of SPH-iii. The structures were purified using gel electrophoresis purification and imaged with transmission electron microscopy using uranyl format for staining. Scale bar: 200 nm.

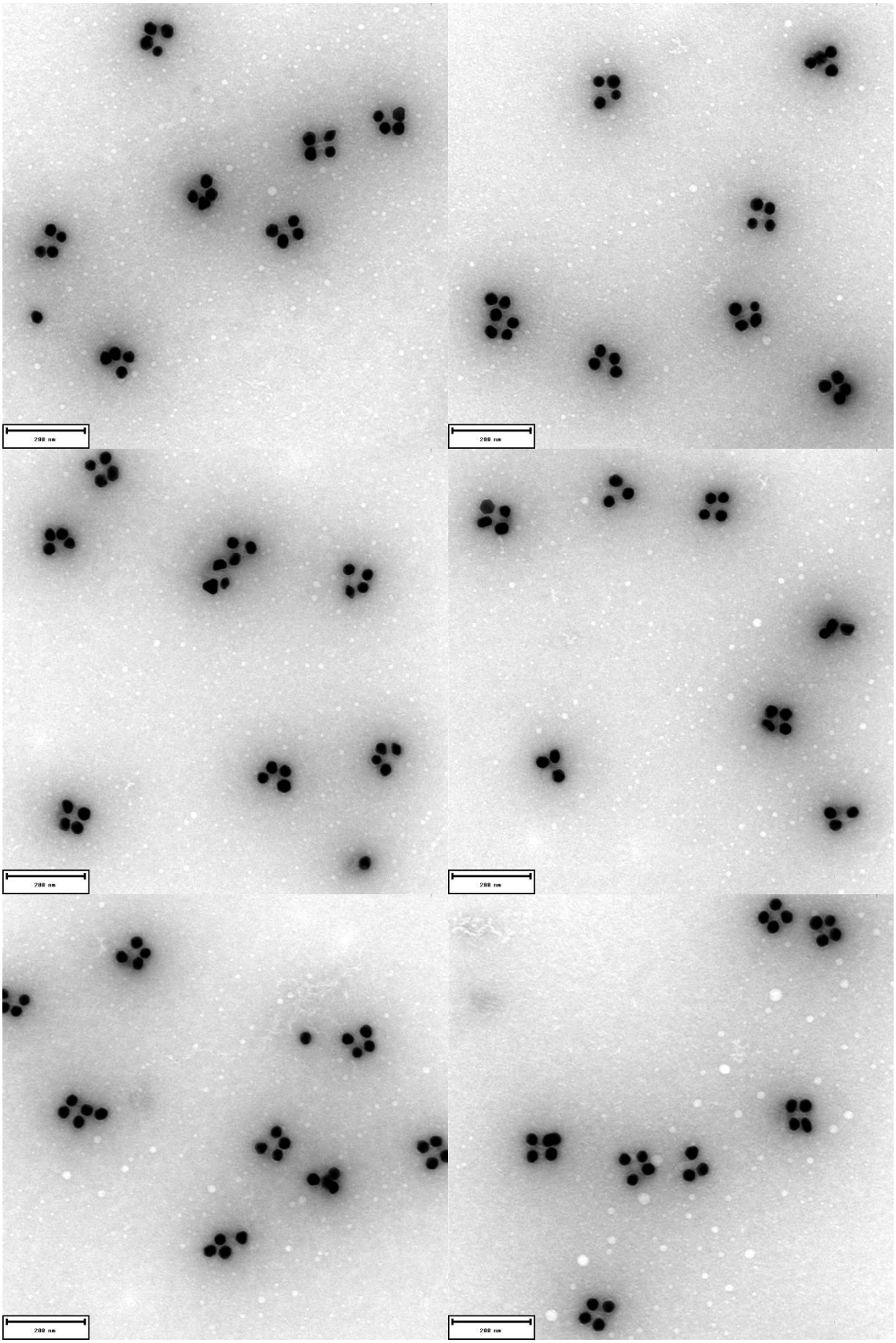

Figure A.31: Electron micrographs of SPH-iv. The structures were purified using gel electrophoresis purification and imaged with transmission electron microscopy using uranyl format for staining. Scale bar: 200 nm.

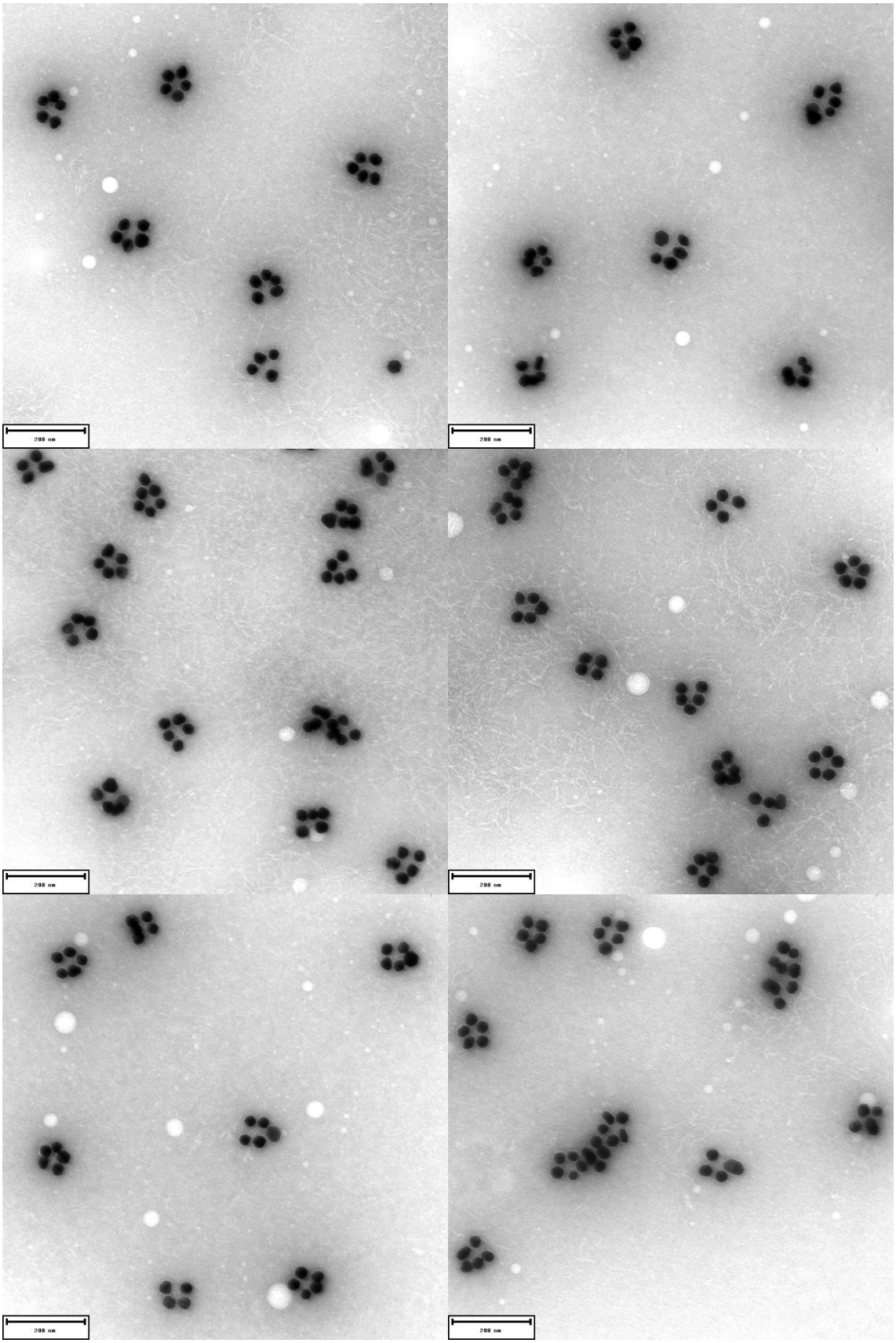

Figure A.32: Electron micrographs of SPH-v. The structures were purified using gel electrophoresis purification and imaged with transmission electron microscopy using uranyl format for staining. Scale bar: 200 nm.

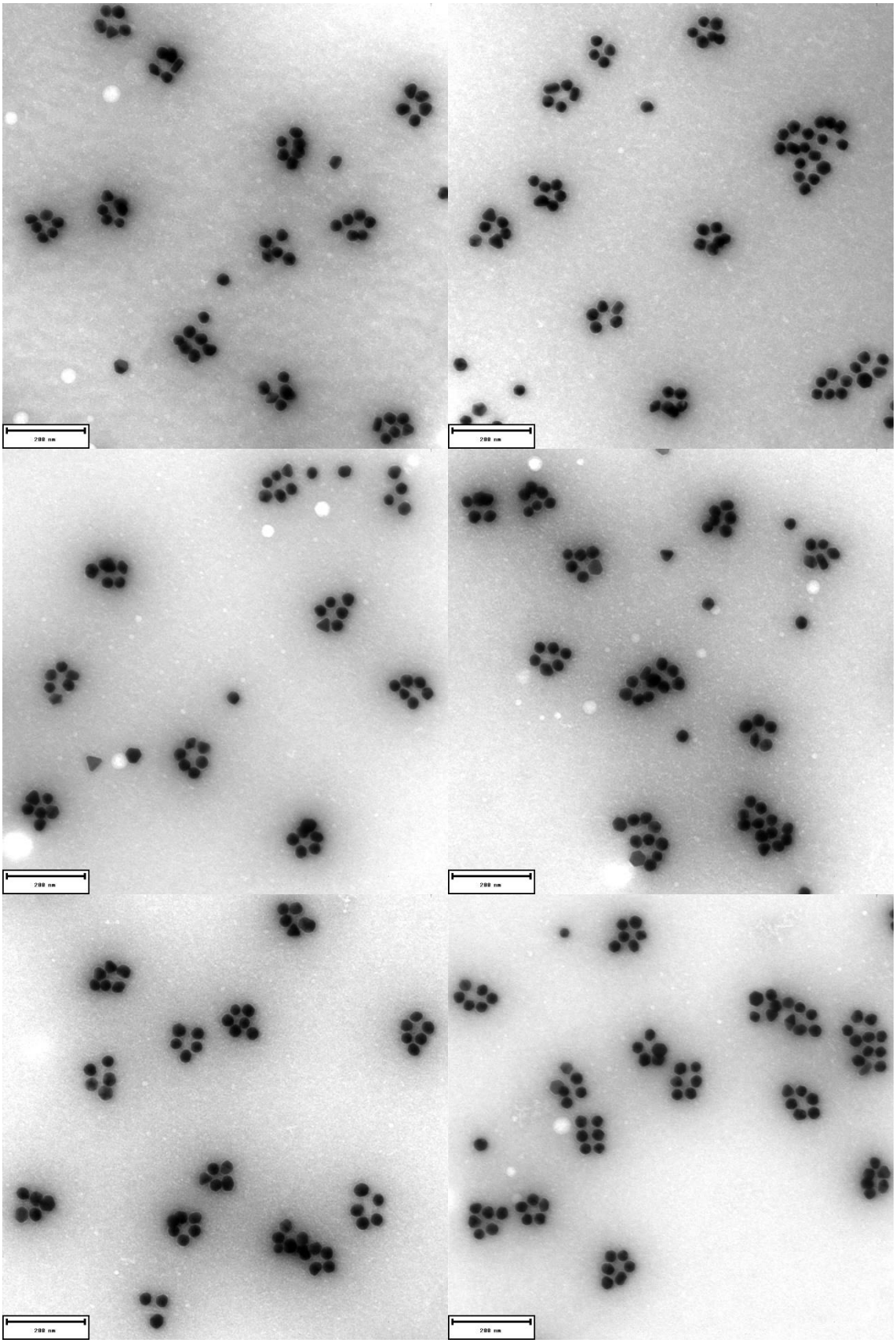

Figure A.33: Electron micrographs of SPH-vi. The structures were purified using gel electrophoresis purification and imaged with transmission electron microscopy using uranyl format for staining. Scale bar: 200 nm.

Table A.8: LPH Synthesis Assembly Statistics

Number of particles	LPH-i	LPH-ii	LPH-iii	LPH-iv	LPH-v	LPH-vi	LPH-vii
1	240	85	20	24	34	63	36
2	56	218	17	-	1	7	1
3	11	19	161	44	3	2	1
4	6	9	16	194	23	12	3
5	1	1	1	21	153	34	11
6	-	1	16	3	17	125	67
7	-	1	-	6	-	40	131
8	-	-	3	9	-	1	17
9	-	-	2	-	1	1	1
Total	314	334	236	277	196	222	232

Table A.9: SPH Synthesis Assembly Statistics

Number of particles	SPH-i	SPH-ii	SPH-iii	SPH-iv	SPH-v	SPH-vi
1	251	8	12	4	6	3
2	-	300	25	1	1	2
3	-	3	278	48	1	4
4	-	2	4	179	55	14
5	-	1	1	6	164	99
6	-	-	-	2	6	143
7	-	-	-	2	-	5
Total	251	314	320	242	233	270

Chirality Transfer

40 nm NSs were incubated at an optical density (OD) of 4 with 10 mM thiol-modified DNA oligonucleotides, previously activated with TCEP, and 0.02% SDS. NR synthesis was performed following the protocol of Ye et al. [177] 60 nm x 23 nm NRs were incubated at OD 1.4 with 5 mM thiol-modified DNA oligonucleotides and 0.1% SDS. Samples were frozen, thawed and purified using gel electrophoresis with a 0.7% agarose gel in a buffer of 1X TAE, 11 mM MgCl2, run for 1.5 h at 120 V. Subsequently the correct monomer bands were cut and squeezed to redisperse in buffer.

For the synthesis of the NR– –NR sample, NRs were added to the origami structures in a ratio of 10:1 in a buffer of 1X TAE, 11 mM MgCl2 plus 500 mM NaCl and incubated for 24 h. For the NR–NS–NR sample, first NSs were incubated with the DNA origami in a ratio of 5:1 in a buffer of 1X TAE, 11 mM MgCl2 plus 500 mM NaCl for 24 h. Afterwards NRs were added in a ratio of 10:1 to the origami, and incubated in the same buffer for 24 h. Both (NR– –NR and NR–NS–NR) samples were purified using gel electrophoresis with a 0.7% agarose gel in a buffer of 1X TAE, 11 mM MgCl2, run for 1.5 h at 70 V. The structure bands were cut out, squeezed and identified by TEM.

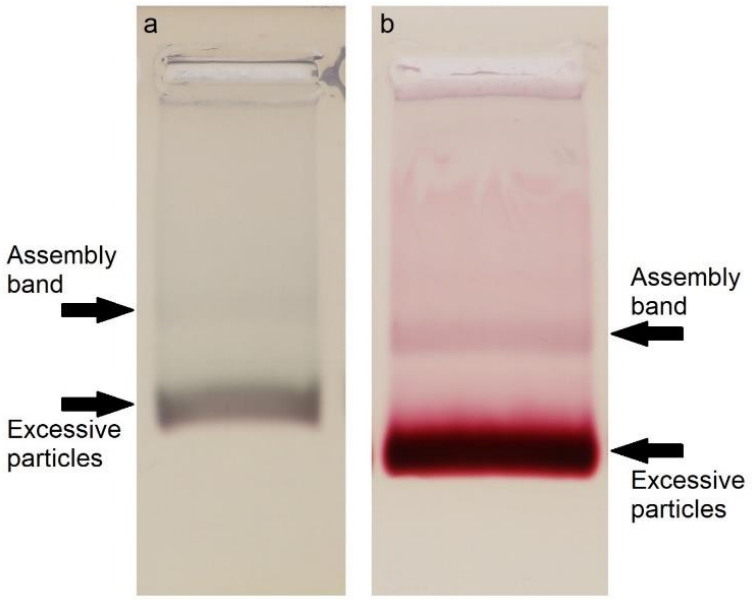

Figure A.34: Gel electrophoresis bands of samples with **a**) the NR– –NR arrangement and **b**) the NR–NS–NR arrangement

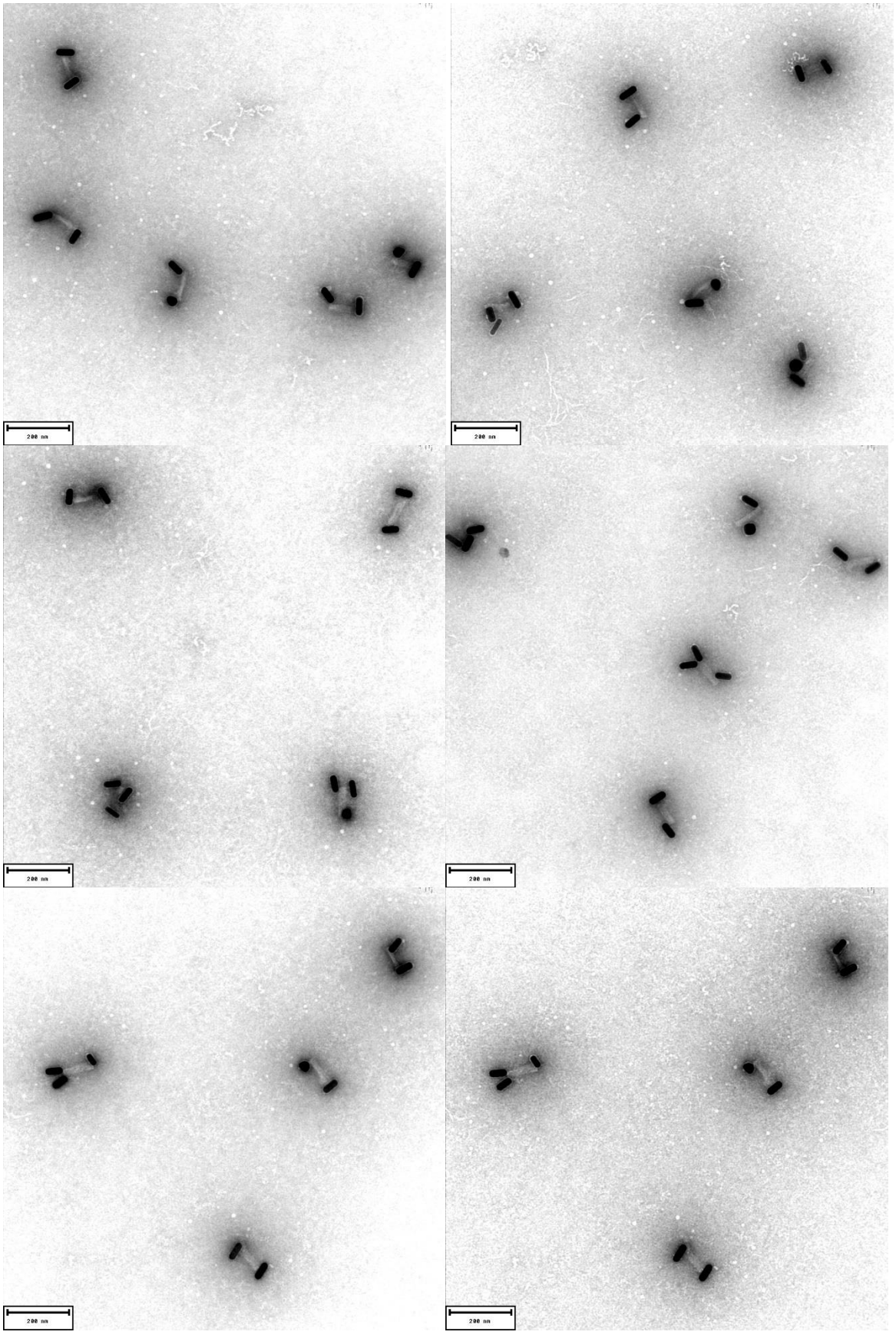

Figure A.35: Electron micrographs of the NR– –NR arrangement. The structures were purified using gel electrophoresis purification and imaged using uranyl format for staining. Scale bar: 200 nm.

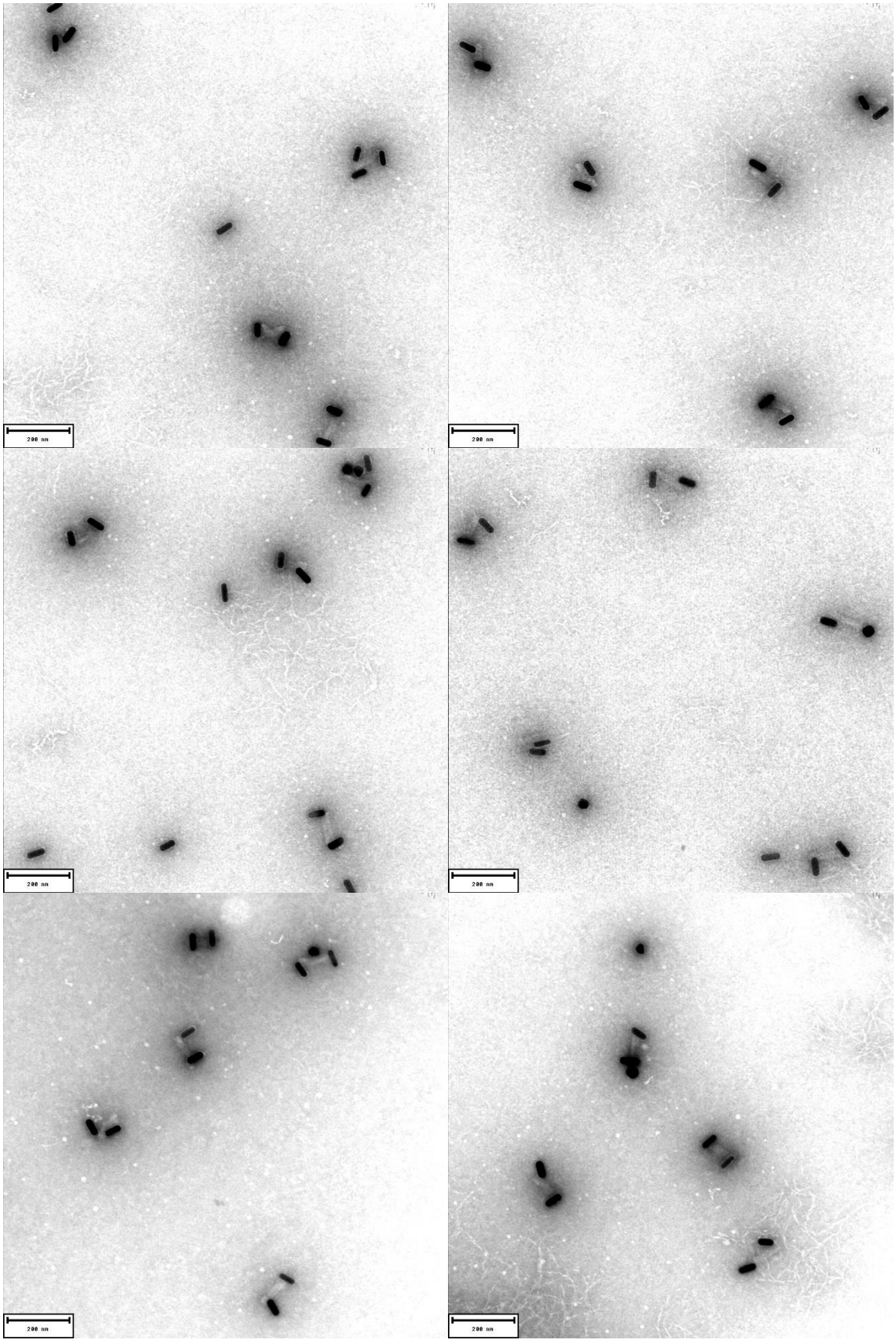

Figure A.36: Electron micrographs of the NR– –NR arrangement. The structures were purified using gel electrophoresis purification and imaged using uranyl format for staining. Scale bar: 200 nm.

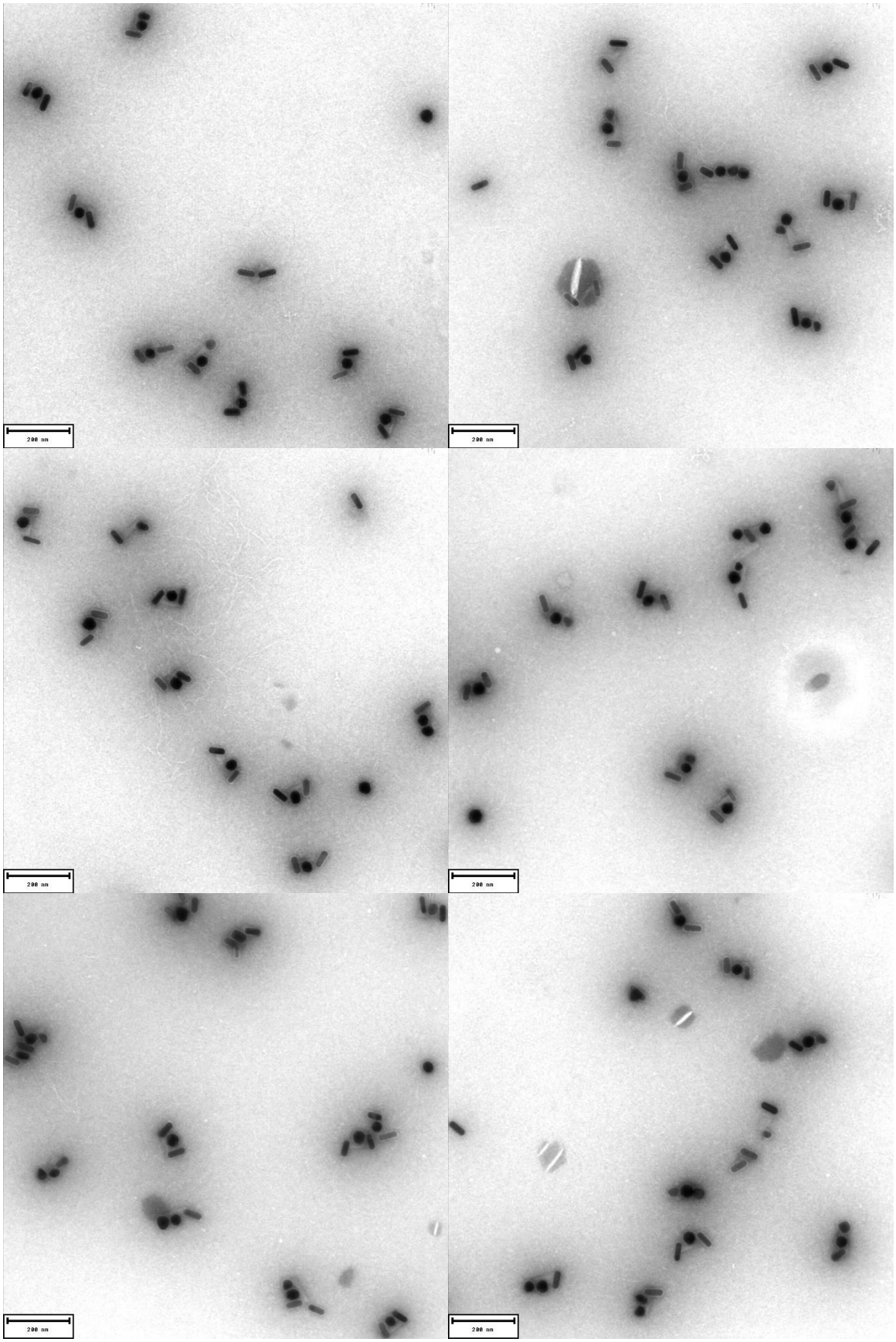

Figure A.37: Electron micrographs of NR–NS–NR sample. The structures were purified using gel electrophoresis purification and imaged using uranyl format for staining. Scale bar: 200 nm.

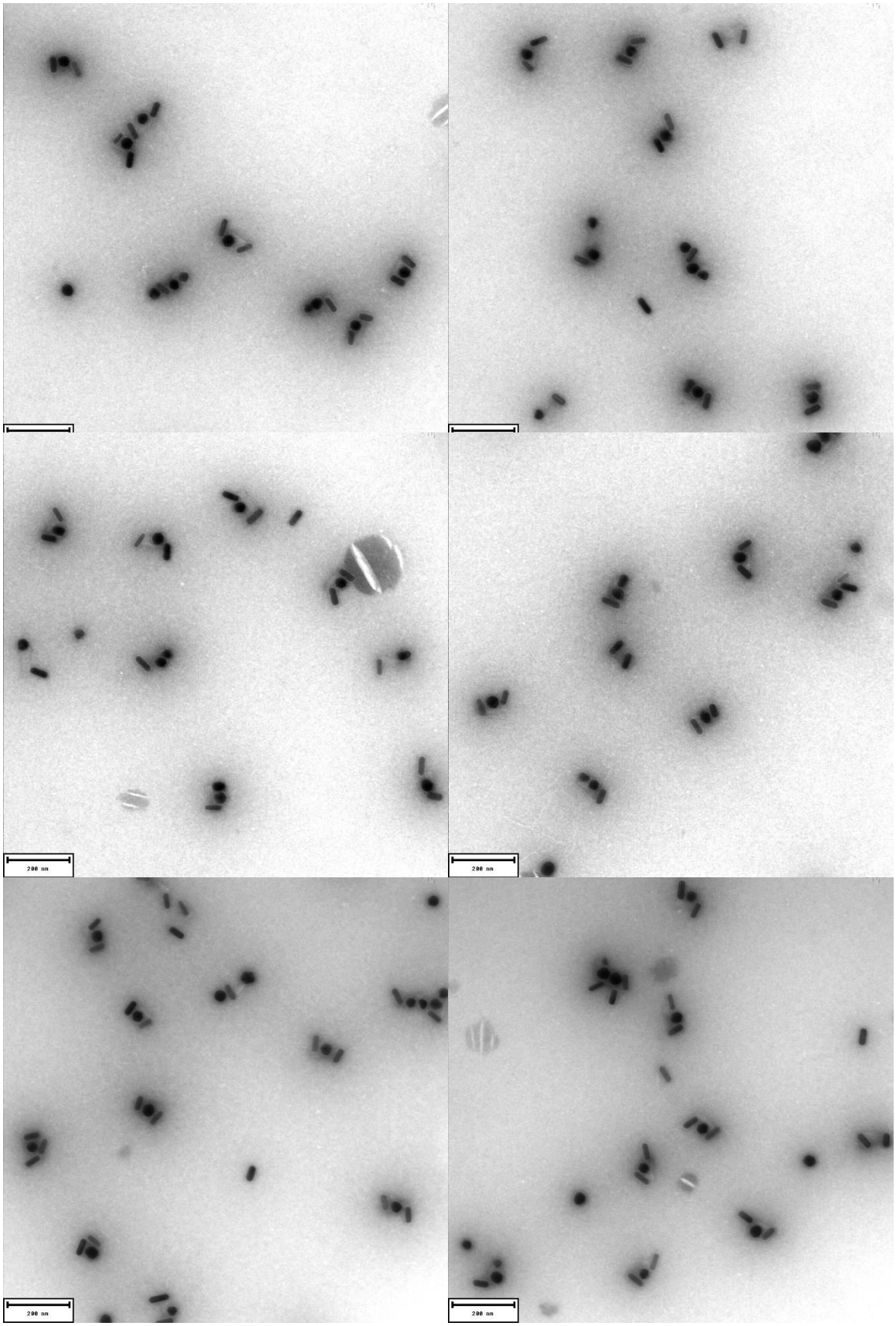

Figure A.38: Electron micrographs of NR–NS–NR sample. The structures were purified using gel electrophoresis purification and imaged using uranyl format for staining. Scale bar: 200 nm.

Table A.10: NR– –NR Synthesis Assembly Statistics.

Assembly	Number	Percentage
NR– –	3	< 3 %
NR– –NR	113	57.5 ±7 %
NS– –NR	27	14 ±4.5 %
NS– –NS	1	< 1.5 %
NR– –2NR	30	15.5 ±5 %
NR–NS–NR	7	3.5 ±2.5 %
NR–NR–NS	8	4 ±2.5 %
NR–NS–NS	3	< 3 %
NS–NR–NS	1	< 1.5 %
NR–NR–NR–NR	2	< 2 %
NR–NR–NS–NS	1	< 1.5 %
Total	196	100 %

Table A.11: NR– –NR Synthesis Particle Statistics.

Particle	Number	Percentage
NS	54	12 ±3 %
NR	390	88 ±3 %
Total	444	100 %

Table A.12: NR–NS–NR Synthesis Assembly Statistics.

Assembly	Number	Percentage
NR– –NR	28	9 ±3 %
NS– –NR	11	3.5 ±2 %
NS– –NS	3	< 2 %
NR– –2NR	4	1.5 ±1 %
NR–NS–NR	160	51 ±5.5 %
NS– –2NR	8	2.5 ±1.5 %
NR–NS–NS	57	18 ±4.5 %
NS–NR–NS	4	1.5 ±1 %
NS–NS–NS	5	1.5 ±1.5 %
NR–2NS–NR	5	1.5 ±1.5 %
NR–NR–2NR	3	< 2 %
NS–NS–2NR	3	< 2 %
NR–NS–NR–NS	7	2 ±1.5 %
NR–NS–2NR	7	2 ±1.5 %
NR–NS–2NS	4	1.5 ±1 %
NS–NR–2NS	3	< 2 %
NS–NR–3NS	1	< 0.5 %
Total	313	100 %

Table A.13: NR– –NR Synthesis Particle Statistics.

Particle	Number	Percentage
NS	354	41 ±3 %
NR	577	59 ±3 %
Total	931	100 %

Nanowheel

20 nm gold nanoparticles and silver particles were incubated at an optical density (OD) of 4 with 10 mM thiol-modified DNA oligonucleotides, previously activated with TCEP, and 0.02% SDS. Samples were frozen, thawed and purified using gel electrophoresis with a 0.7% agarose gel in a buffer of 1X TAE, 11 mM MgCl2, run for 1.5 h at 120 V. Subsequently the correct monomer bands were cut and squeezed to redisperse in buffer.

For the synthesis of the Nanowheel samples, gold and silver nanoparticles were added to the origami structures in a ratio of 5:1 for each particle in a buffer of 1X TAE, 11 mM MgCl2 plus 500 mM NaCl and incubated for between 1 and 24 h. The samples were purified using gel electrophoresis with a 1.5% agarose gel in a buffer of 1X TAE, 11 mM MgCl2, run for 4-6 h at 70 V. The correct band of fully formed structures was cut out and squeezed and analyzed by TEM.

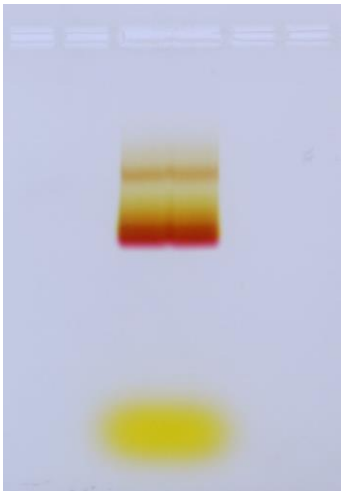

Figure A.39: Gel electrophoresis bands of Nanowheel sample

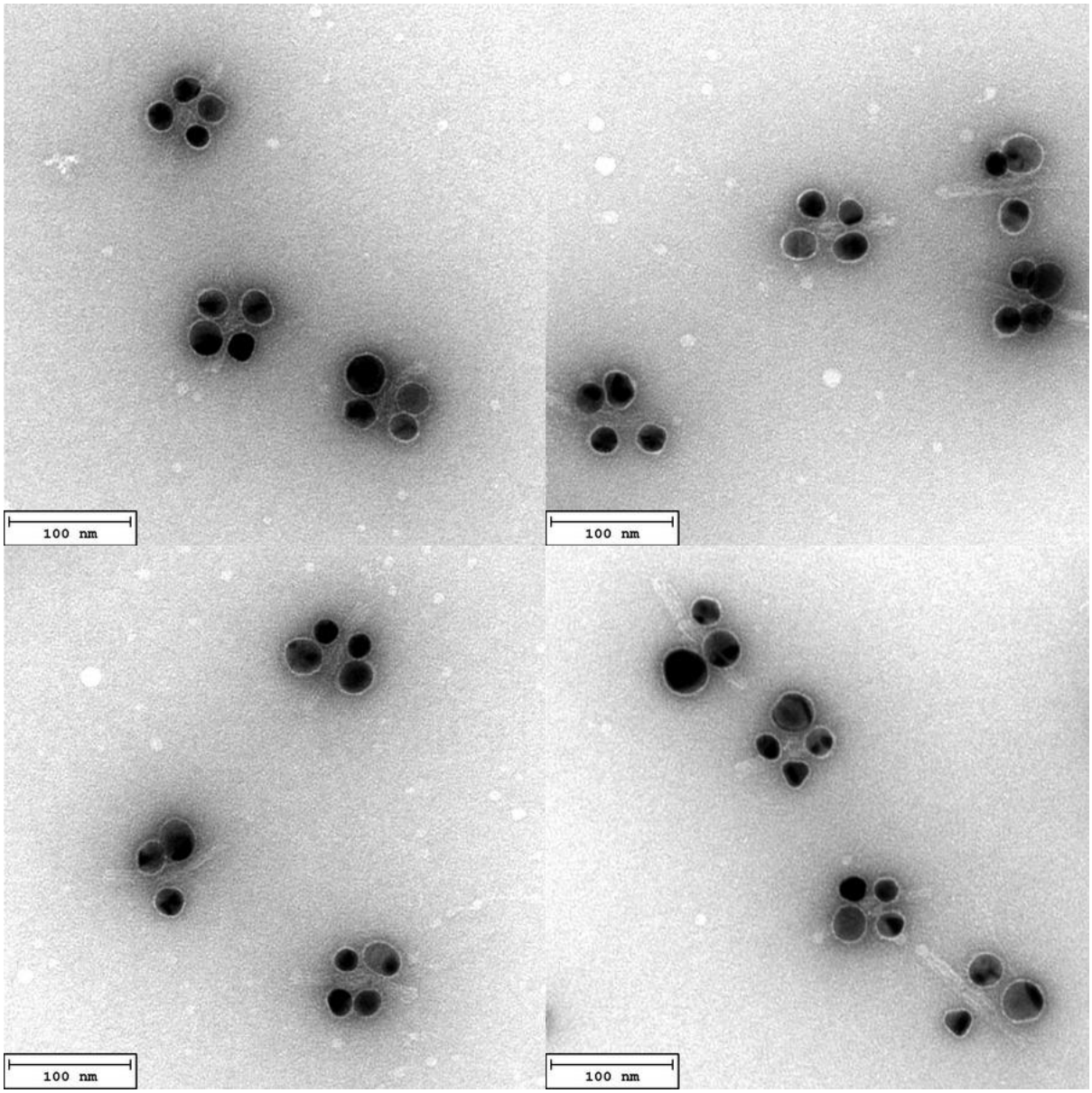

Figure A.40: Electron micrographs of Nanowheel sample. The structures were purified using gel electrophoresis purification and imaged using uranyl format for staining.

A.5 CD and Extinction Measurements

Samples were measured with a Chirascan circular dichroism spectrometer (Applied Photophysics, Surrey, UK) in cuvettes with 3 mm pathlengths.

For the Large Pitch and Small Pitch Helix, spectra were collected in 1 nm steps with 1 s for each step. 2 measurements were made and averaged for the LPH samples, 3 measurements were made and averaged for the SPH samples.

For the Chirality Transfer**,** spectra were collected in 0.5 nm steps with 0.3 s for each step. 3 measurements were made an averaged for the NR– –NR sample.

A.6 Numerical Simulations

Large Pitch and Small Pitch Helix

To compute absorption and circular dichroism (CD) spectra for a given nanoassembly sample, we numerically solve the linear Maxwell's equations in the frequency domain, i.e., the steady-state field oscillating at a fixed optical frequency is computed. A geometry model is defined from the experimentally given parameters of a single nanoparticle helix arrangement (number and diameter of Au particles, their placement in space relatively to the DNA origami structure). The DNA origami is modeled as a dielectric cylinder of length 232nm (69nm), diameter 17nm (18nm), top and bottom edge rounding of 2nm for the LPH (SPH) assembly. For the SPH helix the cylinder is hollow with an inner diameter of 6nm. The model assumes wavelength dependent [Johnson&Christy] optical material parameters (refractive index) for gold, a constant refractive index of 1.58 for the dielectric cylinder modeling the DNA origami, and a constant refractive index of 1.33 for the background solution. In order to model the random orientation of the nanoassemblies in the background solution, the single assembly in our model is illuminated using left- and right-hand circularly polarized plane waves from 60 directions, and the results are obtained by averaging over the independent solutions for the various illuminations.

For computing the scattered light field ("near field") we use an adaptive finite-element method, implemented in the solver JCMsuite, version V4.2. The geometry model is discretized using tetrahedral mesh elements. Typical mesh element side lengths range between 2.5nm and 20nm. The electric field solution is discretized using second-order edge-elements. For checking the sufficient accuracy of the achieved results, reference

solutions with third-order edge-elements have been computed for the same space discretizations. Transparent boundary conditions are realized by using perfectly matched layers.

The absorbed electromagnetic field energy for each source is calculated through volume integration of the electromagnetic field energy density in the absorbing Au nanoparticles. Correspondingly, the scattered electromagnetic field energy is calculated through surface integration of the electromagnetic energy flux density over the boundary of the computational domain. Absorption and CD signals are obtained from these quantities. For computing the spectral responses of the various nanoparticle assemblies, the physical quantities in the input for the simulation software are parameterized, and the FEM computations are distributed automatically to various threads on a workstation, for parallel execution.

For obtaining field patterns for visualization purposes (Fig 4), for each source direction and polarization, the electric field energy density is computed in a post-process. The densities are summed up to give the total energy density field in a further post-process. This total field is then exported on the geometry patches of the material interfaces within the computational domain, and displayed using a field viewer.

Chirality Transfer

For solving Maxwell's equations we use a higher-order finite-element method (FEM), implemented in the solver JCMsuite. [149] The geometry is discretized using a tetrahedral mesh with curvilinear mesh elements along the curved surfaces of the NPs. Transparent boundary conditions are realized by using perfectly matched layers. We use tabulated material data for NP material Au [150] and a constant refractive index of 1.4 for the background material. High numerical accuracy is ensured by using a conservative setting of the numerical parameters (polynomial degree of the FEM ansatz functions of p=2 and mesh element edge size smaller than 7 nm for the NPs and 14 nm for background material). The absorbed electromagnetic field energy and the electromagnetic field energy scattered outwards, corresponding to each circular polarized source term (left-hand circular polarization, LCP, and right-hand circular polarization, RCP), are obtained

in post-processes. The extinction is given by the sum of absorption and scattering for both polarization directions, LCP and RCP, and for all six directions of incidence. The CD (g-factor) is given by the difference between absorption and scattering for LCP and absorption and scattering for RCP, and is normalized to the extinction maximum of the respective wavelength spectrum. Field patterns for visualization purposes (Fig. 3e, f) are obtained by exporting the computed near-fields on specific cross-sections, and a summation of the exported fields over all source terms at a specific wavelength. For performing numerical parameter studies as shown in Fig. 4, the physical quantities of the project are parameterized, and a scripting language (Matlab) is used to automatically generate the input files and to distribute the FEM computations to various threads on a workstation for parallel computation of the parameter- and wavelength-scans.

Bibliography

[1] Web Page. URL: https://commons.wikimedia.org/wiki/

[2] Seeman, N. C. (2003). DNA in a material world. *Nature*, 421(6921), 427-431.

[3] Douglas, S. M., Dietz, H., Liedl, T., Högberg, B., Graf, F., & Shih, W. M. (2009). Self-assembly of DNA into nanoscale three-dimensional shapes. *Nature*, 459(7245), 414-418.

[4] Dahm, R. (2008). Discovering DNA: Friedrich Miescher and the early years of nucleic acid research. *Human genetics*, 122(6), 565-581.

[5] Bryson, B. (2004). Book Review: A Short History of Nearly Everything/Broadway Books, 2003 Doubleday. *Monthly Notes of the Astronomical Society of South Africa*, 63, 94.

[6] Kossel, A. (1891). Über die chemische Zusammensetzung der Zelle. *Archiv für Anatomie und Physiologie/Physiologische Abteilung*. 178.

[7] Professor Raymond Gosling, DNA scientist – obituary. (2015, May 22) *The Daily Telegraph.* https://www.telegraph.co.uk/news/obituaries/11624246/Professor-Raymond-Gosling-DNA-scientist-obituary.html

[8] Franklin, R. E., & Gosling, R. G. (1953). Molecular configuration in sodium thymonucleate. *Nature*, 171(4356), 740-741.

[9] Watson, J. D., & Crick, F. H. (1953). Molecular structure of nucleic acids: a structure for deoxyribose nucleic acid. *Nature*, 171(4356), 737-738.

[10] Wilkins, M. H. F., Stokes, A. R. & Wilson, H. R. (1953). Molecular Structure of Nucleic Acids: Molecular Structure of Deoxypentose Nucleic Acids. *Nature*, 171, 738--740.

[11] Tinland, B., Pluen, A., Sturm, J., & Weill, G. (1997). Persistence length of single-stranded DNA. *Macromolecules*, 30(19), 5763-5765.

[12] Bednar, J., Furrer, P., Katritch, V., Stasiak, A., Dubochet, J., & Stasiak, A. (1995). Determination of DNA persistence length by cryo-electron microscopy. Separation of the static and dynamic contributions to the apparent persistence length of DNA. *Journal of molecular biology*, 254(4), 579-594.

[13] Holliday, R. (1964). The induction of mitotic recombination by mitomycin C in Ustilago and Saccharomyces. *Genetics*, 50(3), 323.

[14] Seeman, N. C. (1982). Nucleic acid junctions and lattices. *Journal of theoretical biology*, 99(2), 237-247.

[15] Kallenbach, N. R., Ma, R. I., & Seeman, N. C. (1983). An immobile nucleic acid junction constructed from oligonucleotides. *Nature*, 305(5937), 829-831.

[16] Chen, J., & Seeman, N. C. (1991). Synthesis from DNA of a molecule with the connectivity of a cube. *Nature*, 350(6319), 631-633.

[17] Mao, C., Sun, W., & Seeman, N. C. (1997). Assembly of Borromean rings from DNA. *Nature*, 386(6621), 137-138.

[18] Mao, C., Sun, W., Shen, Z., & Seeman, N. C. (1999). A nanomechanical device based on the B–Z transition of DNA. *Nature*, 397(6715), 144-146.

[19] Gehring, K., Leroy, J. L., & Gueron, M. (1993). A tetrameric DNA structure with protonated cytosine-cytosine base pairs. *Nature*, 363(6429), 561-565.

[20] Liu, D., & Balasubramanian, S. (2003). A proton-fuelled DNA nanomachine. *Angewandte Chemie International Edition*, 42(46), 5734-5736.

[21] Yurke, B., Turberfield, A. J., Mills, A. P., Simmel, F. C., & Neumann, J. L. (2000). A DNA-fuelled molecular machine made of DNA. *Nature*, 406(6796), 605-608.

[22] Alivisatos, A. P., Johnsson, K. P., Peng, X., Wilson, T. E., Loweth, C. J., Bruchez, M. P., & Schultz, P. G. (1996). Organization of'nanocrystal molecules' using DNA. *Nature*, 382(6592), 609-611.

[23] Winfree, E., Liu, F., Wenzler, L. A., & Seeman, N. C. (1998). Design and self-assembly of two-dimensional DNA crystals. *Nature*, 394(6693), 539-544.

[24] Yan, H., Park, S. H., Finkelstein, G., Reif, J. H., & LaBean, T. H. (2003). DNA-templated self-assembly of protein arrays and highly conductive nanowires. *Science*, 301(5641), 1882-1884.

[25] Wei, B., Dai, M., & Yin, P. (2012). Complex shapes self-assembled from single-stranded DNA tiles. *Nature*, 485(7400), 623-626.

[26] Ke, Y., Ong, L. L., Shih, W. M., & Yin, P. (2012). Three-dimensional structures self-assembled from DNA bricks. *Science*, 338(6111), 1177-1183.

[27] Rothemund, P. W. (2006). Folding DNA to create nanoscale shapes and patterns. *Nature*, 440(7082), 297-302.

[28] Ke, Y., Ong, L. L., Shih, W. M., & Yin, P. (2012). Three-dimensional structures self-assembled from DNA bricks. *Science*, 338(6111), 1177-1183.

[29] Andersen, E. S., Dong, M., Nielsen, M. M., Jahn, K., Subramani, R., Mamdouh, W., ... & Kjems, J. (2009). Self-assembly of a nanoscale DNA box with a controllable lid. *Nature*, 459(7243), 73-76.

[30] Liu, D., Wang, M., Deng, Z., Walulu, R., & Mao, C. (2004). Tensegrity: construction of rigid DNA triangles with flexible four-arm DNA junctions. *Journal of the American Chemical Society*, 126(8), 2324-2325.

[31] Liedl, T., Högberg, B., Tytell, J., Ingber, D. E., & Shih, W. M. (2010). Self-assembly of three-dimensional prestressed tensegrity structures from DNA. *Nature nanotechnology*, 5(7), 520-524.

[32] Douglas, S. M., Marblestone, A. H., Teerapittayanon, S., Vazquez, A., Church, G. M., & Shih, W. M. (2009). Rapid prototyping of 3D DNA-origami shapes with caDNAno. *Nucleic acids research*, 37(15), 5001-5006.

[33] Castro, C. E., Kilchherr, F., Kim, D. N., Shiao, E. L., Wauer, T., Wortmann, P., ... & Dietz, H. (2011). A primer to scaffolded DNA origami. *Nature methods*, 8(3), 221-229.

[34] Kim, D. N., Kilchherr, F., Dietz, H., & Bathe, M. (2012). Quantitative prediction of 3D solution shape and flexibility of nucleic acid nanostructures. *Nucleic acids research*, 40(7), 2862-2868.

[35] Gerling, T., Wagenbauer, K. F., Neuner, A. M., & Dietz, H. (2015). Dynamic DNA devices and assemblies formed by shape-complementary, non–base pairing 3D components. *Science*, 347(6229), 1446-1452.

[36] Wagenbauer, K. F., Sigl, C., & Dietz, H. (2017). Gigadalton-scale shape-programmable DNA assemblies. *Nature*, 552(7683), 78-83.

[37] Praetorius, F., Kick, B., Behler, K. L., Honemann, M. N., Weuster-Botz, D., & Dietz, H. (2017). Biotechnological mass production of DNA origami. *Nature*, 552(7683), 84-87.

[38] Zhang, T., Hartl, C., Frank, K., Heuer-Jungemann, A., Fischer, S., Nickels, P. C., ... & Liedl, T. (2018). 3D DNA origami crystals. *Advanced Materials*, 30(28), 1800273.

[39] Schuller, V. J., Heidegger, S., Sandholzer, N., Nickels, P. C., Suhartha, N. A., Endres, S., ... & Liedl, T. (2011). Cellular immunostimulation by CpG-sequence-coated DNA origami structures. *ACS nano*, 5(12), 9696-9702.

[40] Jiang, Q., Song, C., Nangreave, J., Liu, X., Lin, L., Qiu, D., ... & Ding, B. (2012). DNA origami as a carrier for circumvention of drug resistance. *Journal of the American Chemical Society*, 134(32), 13396-13403.

[41] Zhao, Y. X., Shaw, A., Zeng, X., Benson, E., Nyström, A. M., & Högberg, B. (2012). DNA origami delivery system for cancer therapy with tunable release properties. *ACS nano*, 6(10), 8684-8691.

[42] Zhang, Q., Jiang, Q., Li, N., Dai, L., Liu, Q., Song, L., ... & Du, Y. (2014). DNA origami as an in vivo drug delivery vehicle for cancer therapy. *ACS nano*, 8(7), 6633-6643.

[43] Mei, Q., Wei, X., Su, F., Liu, Y., Youngbull, C., Johnson, R., ... & Meldrum, D. (2011). Stability of DNA origami nanoarrays in cell lysate. *Nano letters*, 11(4), 1477-1482.

[44] Hahn, J., Wickham, S. F., Shih, W. M., & Perrault, S. D. (2014). Addressing the instability of DNA nanostructures in tissue culture. *ACS nano*, 8(9), 8765-8775.

[45] Perrault, S. D., & Shih, W. M. (2014). Virus-inspired membrane encapsulation of DNA nanostructures to achieve in vivo stability. *ACS nano*, 8(5), 5132-5140.

[46] Paunescu, D., Puddu, M., Soellner, J. O., Stoessel, P. R., & Grass, R. N. (2013). Reversible DNA encapsulation in silica to produce ROS-resistant and heat-resistant synthetic DNA'fossils'. *Nature protocols*, 8(12), 2440-2448.

[47] Liu, X., Zhang, F., Jing, X., Pan, M., Liu, P., Li, W., ... & Fan, C. (2018). Complex silica composite nanomaterials templated with DNA origami. *Nature*, 559(7715), 593-598.

[48] Nguyen, L., Döblinger, M., Liedl, T., & Heuer-Jungemann, A. (2019). DNA-Origami-Templated Silica Growth by Sol–Gel Chemistry. *Angewandte Chemie International Edition*, 58(3), 912-916.

[49] Douglas, S. M., Bachelet, I., & Church, G. M. (2012). A logic-gated nanorobot for targeted transport of molecular payloads. *Science*, 335(6070), 831-834.

[50] Thubagere, A. J., Li, W., Johnson, R. F., Chen, Z., Doroudi, S., Lee, Y. L., ... & Qian, L. (2017). A cargo-sorting DNA robot. *Science*, 357(6356).

[51] Kopperger, E., List, J., Madhira, S., Rothfischer, F., Lamb, D. C., & Simmel, F. C. (2018). A self-assembled nanoscale robotic arm controlled by electric fields. *Science*, 359(6373), 296-301.

[52] Hurst, S. J., Lytton-Jean, A. K., & Mirkin, C. A. (2006). Maximizing DNA loading on a range of gold nanoparticle sizes. *Analytical chemistry*, 78(24), 8313-8318.

[53] Ding, B., Deng, Z., Yan, H., Cabrini, S., Zuckermann, R. N., & Bokor, J. (2010). Gold nanoparticle self-similar chain structure organized by DNA origami. *Journal of the American Chemical Society*, 132(10), 3248-3249.

[54] Kuzyk, A., Schreiber, R., Fan, Z., Pardatscher, G., Roller, E. M., Högele, A., ... & Liedl, T. (2012). DNA-based self-assembly of chiral plasmonic nanostructures with tailored optical response. *Nature*, 483(7389), 311-314.

[55] Fan, Z., & Govorov, A. O. (2010). Plasmonic circular dichroism of chiral metal nanoparticle assemblies. *Nano letters*, 10(7), 2580-2587.

[56] Schreiber, R., Luong, N., Fan, Z., Kuzyk, A., Nickels, P. C., Zhang, T., ... & Liedl, T. (2013). Chiral plasmonic DNA nanostructures with switchable circular dichroism. *Nature communications*, 4(1), 1-6.

[57] Kuzyk, A., Schreiber, R., Zhang, H., Govorov, A. O., Liedl, T., & Liu, N. (2014). Reconfigurable 3D plasmonic metamolecules. *Nature materials*, 13(9), 862-866.

[58] Funck, T., Nicoli, F., Kuzyk, A., & Liedl, T. (2018). Sensing picomolar concentrations of RNA using switchable plasmonic chirality. *Angewandte Chemie International Edition*, 57(41), 13495-13498.

[59] Nguyen, L., Dass, M., Ober, M. F., Besteiro, L. V., Wang, Z. M., Nickel, B., ... & Heuer-Jungemann, A. (2020). Chiral Assembly of Gold–Silver Core–Shell Plasmonic Nanorods on DNA Origami with Strong Optical Activity. *ACS nano*, 14(6), 7454-7461.

[60] Maier, S. A. (2007). *Plasmonics: fundamentals and applications* (Vol. 1, p. 245). New York: springer.

[61] Stockman, M. I. (2011). Nanoplasmonics: past, present, and glimpse into future. *Optics express*, 19(22), 22029-22106.

[62] Pelton, M., & Bryant, G. W. (2013). *Introduction to metal-nanoparticle plasmonics* (Vol. 5). John Wiley & Sons.

[63] Saha, K., Agasti, S. S., Kim, C., Li, X., & Rotello, V. M. (2012). Gold nanoparticles in chemical and biological sensing. *Chemical reviews*, 112(5), 2739-2779.

[64] Meier, M., & Wokaun, A. (1983). Enhanced fields on large metal particles: dynamic depolarization. *Optics letters*, 8(11), 581-583.

[65] Rosenfeld, L. (1929). Quantenmechanische Theorie der natürlichen optischen Aktivität von Flüssigkeiten und Gasen. *Zeitschrift für Physik*, 52(3), 161-174.

[66] Urbanová, M., & Maloň, P. (2007). Circular dichroism spectroscopy. In *Analytical methods in supramolecular chemistry* (pp. 265-304). Wiley–VCH Weinheim, Germany.

[67] Govorov, A. O., Gun'ko, Y. K., Slocik, J. M., Gérard, V. A., Fan, Z., & Naik, R. R. (2011). Chiral nanoparticle assemblies: circular dichroism, plasmonic interactions, and exciton effects. *Journal of Materials Chemistry*, 21(42), 16806-16818.

[68] Pang, Y. K., Lee, J. C. W., Lee, H. F., Tam, W. Y., Chan, C. T., & Sheng, P. (2005). Chiral microstructures (spirals) fabrication by holographic lithography. *Optics Express*, 13(19), 7615-7620.

[69] Zhao, R., Zhang, L., Zhou, J., Koschny, T., & Soukoulis, C. M. (2011). Conjugated gammadion chiral metamaterial with uniaxial optical activity and negative refractive index. *Physical Review B*, 83(3), 035105.

[70] Gansel, J. K., Latzel, M., Frölich, A., Kaschke, J., Thiel, M., & Wegener, M. (2012). Tapered gold-helix metamaterials as improved circular polarizers. *Applied Physics Letters*, 100(10), 101109.

[71] Ogier, R., Fang, Y., Svedendahl, M., Johansson, P., & Käll, M. (2014). Macroscopic layers of chiral plasmonic nanoparticle oligomers from colloidal lithography. *Acs Photonics*, 1(10), 1074-1081.

[72] Pendry, J. B. (2004). A chiral route to negative refraction. *Science*, 306(5700), 1353-1355.

[73] Govorov, A. O., Fan, Z., Hernandez, P., Slocik, J. M., & Naik, R. R. (2010). Theory of circular dichroism of nanomaterials comprising chiral molecules and nanocrystals: plasmon enhancement, dipole interactions, and dielectric effects. *Nano letters*, 10(4), 1374-1382.

[74] Goring, C. R., & Pritchard, A. (1837). *Micrographia: Containing Practical Essays on Reflecting, Solar, Oxy-hydrogen Gas Microscopes; Micrometers; Eye-pieces, etc.* Whitaker and Company.

[75] Zsigmondy, R. (1926). Nobel Lecture: Properties of Colloids. Nobelprize. org. Nobel Media AB 2014.

[76] Erni, R., Rossell, M. D., Kisielowski, C., & Dahmen, U. (2009). Atomic-resolution imaging with a sub-50-pm electron probe. *Physical review letters*, 102(9), 096101.

[77] Meyer, J. C., Girit, C. O., Crommie, M. F., & Zettl, A. (2008). Imaging and dynamics of light atoms and molecules on graphene. Nature, 454(7202), 319-322.

[78] Martens, K., Funck, T., Santiago, E. Y., Govorov, A. O., Burger, S., & Liedl, T. (2021). On the origin of chirality in plasmonic meta-molecules. *arXiv preprint* arXiv:2110.06689.

[79] Cahn, R. S., Ingold, C., & Prelog, V. (1966). Specification of molecular chirality. *Angewandte Chemie International Edition in English*, 5(4), 385-415.

[80] Bentley, R. (2005). Role of sulfur chirality in the chemical processes of biology. *Chemical Society Reviews*, 34(7), 609-624.

[81] Thilgen, C., & Diederich, F. (2006). Structural aspects of fullerene chemistry a journey through fullerene chirality. *Chemical reviews*, 106(12), 5049-5135.

[82] Naaman, R., Paltiel, Y., & Waldeck, D. H. (2019). Chiral molecules and the electron spin. *Nature Reviews Chemistry*, 3(4), 250-260.

[83] Woody, R. W. (1995). [4] Circular dichroism. *Methods in enzymology*, 246, 34-71.

[84] Ranjbar, B., & Gill, P. (2009). Circular dichroism techniques: biomolecular and nanostructural analyses-a review. *Chemical biology & drug design*, 74(2), 101-120.

[85] Shen, X., Asenjo-Garcia, A., Liu, Q., Jiang, Q., García de Abajo, F. J., Liu, N., & Ding, B. (2013). Three-dimensional plasmonic chiral tetramers assembled by DNA origami. *Nano letters*, 13(5), 2128-2133.

[86] Cecconello, A., Kahn, J. S., Lu, C. H., Khosravi Khorashad, L., Govorov, A. O., & Willner, I. (2016). DNA scaffolds for the dictated assembly of left-/right-handed plasmonic Au NP helices with programmed chiro-optical properties. Journal of the *American Chemical Society*, 138(31), 9895-9901.

[87] Hartl, C., Frank, K., Amenitsch, H., Fischer, S., Liedl, T., & Nickel, B. (2018). Position accuracy of gold nanoparticles on DNA origami structures studied with small-angle X-ray scattering. *Nano letters*, 18(4), 2609-2615.

[88] Wang, Y., Xu, J., Wang, Y., & Chen, H. (2013). Emerging chirality in nanoscience. *Chemical Society Reviews*, 42(7), 2930-2962.

[89] Bruhn, T., Schaumlöffel, A., Hemberger, Y., & Bringmann, G. (2013). SpecDis: Quantifying the comparison of calculated and experimental electronic circular dichroism spectra. *Chirality*, 25(4), 243-249.

[90] Shen, X., Song, C., Wang, J., Shi, D., Wang, Z., Liu, N., & Ding, B. (2012). Rolling up gold nanoparticle-dressed DNA origami into three-dimensional plasmonic chiral nanostructures. *Journal of the American Chemical Society*, 134(1), 146-149.

[91] Gansel, J. K., Thiel, M., Rill, M. S., Decker, M., Bade, K., Saile, V., ... & Wegener, M. (2009). Gold helix photonic metamaterial as broadband circular polarizer. *Science*, 325(5947), 1513-1515.

[92] Xu, Z., Xu, L., Liz-Marzán, L. M., Ma, W., Kotov, N. A., Wang, L., ... & Xu, C. (2013). Sensitive detection of silver ions based on chiroplasmonic assemblies of nanoparticles. *Advanced Optical Materials*, 1(9), 626-630.

[93] Ma, W., Kuang, H., Xu, L., Ding, L., Xu, C., Wang, L., & Kotov, N. A. (2013). Attomolar DNA detection with chiral nanorod assemblies. *Nature communications*, 4(1), 1-8.

[94] Tang, L., Li, S., Xu, L., Ma, W., Kuang, H., Wang, L., & Xu, C. (2015). Chirality-based Au@ Ag nanorod dimers sensor for ultrasensitive PSA detection. *ACS applied materials & interfaces*, 7(23), 12708-12712.

[95] Jansat, S., Gómez, M., Philippot, K., Muller, G., Guiu, E., Claver, C., ... & Chaudret, B. (2004). A case for enantioselective allylic alkylation catalyzed by palladium nanoparticles. *Journal of the American Chemical Society*, 126(6), 1592-1593.

[96] Wang, W., Besteiro, L. V., Liu, T., Wu, C., Sun, J., Yu, P., ... & Govorov, A. O. (2019). Generation of hot electrons with chiral metamaterial perfect absorbers: giant optical chirality for polarization-sensitive photochemistry. ACS Photonics, 6(12), 3241-3252.

[97] Che, S., Liu, Z., Ohsuna, T., Sakamoto, K., Terasaki, O., & Tatsumi, T. (2004). Synthesis and characterization of chiral mesoporous silica. *Nature*, 429(6989), 281-284.

[98] Moloney, M. P., Gun'ko, Y. K., & Kelly, J. M. (2007). Chiral highly luminescent CdS quantum dots. *Chemical Communications*, (38), 3900-3902.

[99] Elliott, S. D., Moloney, M. P., & Gun'ko, Y. K. (2008). Chiral shells and achiral cores in CdS quantum dots. *Nano Letters*, 8(8), 2452-2457.

[100] Govan, J. E., Jan, E., Querejeta, A., Kotov, N. A., & Gun'ko, Y. K. (2010). Chiral luminescent CdS nano-tetrapods. *Chemical communications*, 46(33), 6072-6074.

[101] Fan, Z., & Govorov, A. O. (2012). Chiral nanocrystals: plasmonic spectra and circular dichroism. *Nano letters*, 12(6), 3283-3289.

[102] Lee, H. E., Ahn, H. Y., Mun, J., Lee, Y. Y., Kim, M., Cho, N. H., ... & Nam, K. T. (2018). Amino-acid-and peptide-directed synthesis of chiral plasmonic gold nanoparticles. *Nature*, 556(7701), 360-365.

[103] Govorov, A. O., & Fan, Z. (2012). Theory of chiral plasmonic nanostructures comprising metal nanocrystals and chiral molecular media. *ChemPhysChem*, 13(10), 2551-2560.

[104] Cathcart, N., Mistry, P., Makra, C., Pietrobon, B., Coombs, N., Jelokhani-Niaraki, M., & Kitaev, V. (2009). Chiral thiol-stabilized silver nanoclusters with well-resolved optical transitions synthesized by a facile etching procedure in aqueous solutions. *Langmuir*, 25(10), 5840-5846.

[105] Dolamic, I., Knoppe, S., Dass, A., & Bürgi, T. (2012). First enantioseparation and circular dichroism spectra of Au 38 clusters protected by achiral ligands. *Nature communications*, 3(1), 1-6.

[106] Chen, C. L., Zhang, P., & Rosi, N. L. (2008). A new peptide-based method for the design and synthesis of nanoparticle superstructures: construction of highly ordered gold nanoparticle double helices. *Journal of the American Chemical Society*, 130(41), 13555-13557.

[107] Oh, H. S., Liu, S., Jee, H., Baev, A., Swihart, M. T., & Prasad, P. N. (2010). Chiral poly (fluorene-alt-benzothiadiazole)(PFBT) and nanocomposites with gold nanoparticles: plasmonically and structurally enhanced chirality. *Journal of the American Chemical Society*, 132(49), 17346-17348.

[108] Qi, H., Shopsowitz, K. E., Hamad, W. Y., & MacLachlan, M. J. (2011). Chiral nematic assemblies of silver nanoparticles in mesoporous silica thin films. *Journal of the American Chemical Society*, 133(11), 3728-3731.

[109] Guerrero-Martínez, A., Auguié, B., Alonso-Gómez, J. L., Džolić, Z., Gómez-Graña, S., Žinić, M., ... & Liz-Marzán, L. M. (2011). Intense optical activity from three-dimensional chiral ordering of plasmonic nanoantennas. *Angewandte Chemie International Edition*, 50(24), 5499-5503.

[110] Zhang, Q., Hernandez, T., Smith, K. W., Jebeli, S. A. H., Dai, A. X., Warning, L., ... & Link, S. (2019). Unraveling the origin of chirality from plasmonic nanoparticle-protein complexes. *Science*, 365(6460), 1475-1478.

[111] González-Rubio, G., Mosquera, J., Kumar, V., Pedrazo-Tardajos, A., Llombart, P., Solís, D. M., ... & Liz-Marzán, L. M. (2020). Micelle-directed chiral seeded growth on anisotropic gold nanocrystals. *Science*, 368(6498), 1472-1477.

[112] Seeman, N. C., & Sleiman, H. F. (2017). DNA nanotechnology. *Nature Reviews Materials*, 3(1), 1-23.

[113] Sharma, J., Chhabra, R., Cheng, A., Brownell, J., Liu, Y., & Yan, H. (2009). Control of self-assembly of DNA tubules through integration of gold nanoparticles. *Science*, 323(5910), 112-116.

[114] Mastroianni, A. J., Claridge, S. A., & Alivisatos, A. P. (2009). Pyramidal and chiral groupings of gold nanocrystals assembled using DNA scaffolds. *Journal of the American Chemical Society,* 131(24), 8455-8459.

[115] Chen, W., Bian, A., Agarwal, A., Liu, L., Shen, H., Wang, L., ... & Kotov, N. A. (2009). Nanoparticle superstructures made by polymerase chain reaction: collective interactions of nanoparticles and a new principle for chiral materials. *Nano letters*, 9(5), 2153-2159.

[116] Molotsky, T., Tamarin, T., Moshe, A. B., Markovich, G., & Kotlyar, A. B. (2010). Synthesis of chiral silver clusters on a DNA template. *The Journal of Physical Chemistry C*, 114(38), 15951-15954.

[117] Yan, W., Xu, L., Xu, C., Ma, W., Kuang, H., Wang, L., & Kotov, N. A. (2012). Self-assembly of chiral nanoparticle pyramids with strong R/S optical activity. *Journal of the American Chemical Society*, 134(36), 15114-15121.

[118] Thacker, V. V., Herrmann, L. O., Sigle, D. O., Zhang, T., Liedl, T., Baumberg, J. J., & Keyser, U. F. (2014). DNA origami based assembly of gold nanoparticle dimers for surface-enhanced Raman scattering. *Nature communications*, 5(1), 1-7.

[119] Dey, S., Fan, C., Gothelf, K. V., Li, J., Lin, C., Liu, L., ... & Zhan, P. (2021). DNA origami. *Nature Reviews Methods Primers*, 1(1), 1-24.

[120] Gansel, J. K., Wegener, M., Burger, S., & Linden, S. (2010). Gold helix photonic metamaterials: a numerical parameter study. *Optics express*, 18(2), 1059-1069.

[121] Fan, Z., & Govorov, A. O. (2011). Helical metal nanoparticle assemblies with defects: plasmonic chirality and circular dichroism. The Journal of Physical Chemistry C, 115(27), 13254-13261.

[122] Martens, K., Binkowski, F., Nguyen, L., Hu, L., Govorov, A. O., Burger, S., & Liedl, T. (2021). Long-and short-ranged chiral interactions in DNA-assembled plasmonic chains. Nature communications, 12(1), 1-6.

[123] Nguyen, L. A., He, H., & Pham-Huy, C. (2006). Chiral drugs: an overview. *International journal of biomedical science: IJBS*, 2(2), 85.

[124] Navea, S., de Juan, A., & Tauler, R. (2002). Detection and resolution of intermediate species in protein folding processes using fluorescence and circular dichroism

spectroscopies and multivariate curve resolution. *Analytical chemistry*, 74(23), 6031-6039.

[125] Bruhn, T., Schaumlöffel, A., Hemberger, Y., & Bringmann, G. (2013). SpecDis: Quantifying the comparison of calculated and experimental electronic circular dichroism spectra. *Chirality*, 25(4), 243-249.

[126] Toader, O., & John, S. (2001). Proposed square spiral microfabrication architecture for large three-dimensional photonic band gap crystals. *Science*, 292(5519), 1133-1135.

[127] Thiel, M., Decker, M., Deubel, M., Wegener, M., Linden, S., & von Freymann, G. (2007). Polarization Stop Bands in Chiral Polymeric Three-Dimensional Photonic Crystals. *Advanced Materials*, 19(2), 207-210.

[128] Ye, Y., & He, S. (2010). 90° polarization rotator using a bilayered chiral metamaterial with giant optical activity. Applied Physics Letters, 96(20), 203501.

[129] Schaaff, T. G., & Whetten, R. L. (2000). Giant gold− glutathione cluster compounds: intense optical activity in metal-based transitions. *The Journal of Physical Chemistry B*, 104(12), 2630-2641.

[130] Elliott, S. D., Moloney, M. P., & Gun'ko, Y. K. (2008). Chiral shells and achiral cores in CdS quantum dots. *Nano Letters*, 8(8), 2452-2457.

[131] Shemer, G., Krichevski, O., Markovich, G., Molotsky, T., Lubitz, I., & Kotlyar, A. B. (2006). Chirality of silver nanoparticles synthesized on DNA. *Journal of the American Chemical Society*, 128(34), 11006-11007.

[132] Bieri, M., Gautier, C., & Bürgi, T. (2007). Probing chiral interfaces by infrared spectroscopic methods. *Physical Chemistry Chemical Physics*, 9(6), 671-685.

[133] Hendry, E., Carpy, T., Johnston, J., Popland, M., Mikhaylovskiy, R. V., Lapthorn, A. J., ... & Kadodwala, M. J. N. N. (2010). Ultrasensitive detection and characterization of biomolecules using superchiral fields. *Nature nanotechnology*, 5(11), 783-787.

[134] Slocik, J. M., Govorov, A. O., & Naik, R. R. (2011). Plasmonic circular dichroism of peptide-functionalized gold nanoparticles. *Nano letters*, 11(2), 701-705.

[135] Zhang, H., & Govorov, A. O. (2013). Giant circular dichroism of a molecule in a region of strong plasmon resonances between two neighboring gold nanocrystals. *Physical Review B*, 87(7), 075410.

[136] Maoz, B. M., Chaikin, Y., Tesler, A. B., Bar Elli, O., Fan, Z., Govorov, A. O., & Markovich, G. (2013). Amplification of chiroptical activity of chiral biomolecules by surface plasmons. *Nano letters*, 13(3), 1203-1209.

[137] Kneer, L. M., Roller, E. M., Besteiro, L. V., Schreiber, R., Govorov, A. O., & Liedl, T. (2018). Circular dichroism of chiral molecules in DNA-assembled plasmonic hotspots. *ACS nano*, 12(9), 9110-9115.

[138] Lan, X., Chen, Z., Dai, G., Lu, X., Ni, W., & Wang, Q. (2013). Bifacial DNA origami-directed discrete, three-dimensional, anisotropic plasmonic nanoarchitectures with tailored optical chirality. *Journal of the American Chemical Society*, 135(31), 11441-11444.

[139] Shen, X., Zhan, P., Kuzyk, A., Liu, Q., Asenjo-Garcia, A., Zhang, H., ... & Liu, N. (2014). 3D plasmonic chiral colloids. *Nanoscale*, 6(4), 2077-2081.

[140] Zhou, C., Duan, X., & Liu, N. (2015). A plasmonic nanorod that walks on DNA origami. *Nature communications*, 6(1), 1-6.

[141] Lan, X., Liu, T., Wang, Z., Govorov, A. O., Yan, H., & Liu, Y. (2018). DNA-guided plasmonic helix with switchable chirality. *Journal of the American Chemical Society*, 140(37), 11763-11770.

[142] Maier, S. A., Kik, P. G., Sweatlock, L. A., Atwater, H. A., Penninkhof, J. J., Polman, A., ... & Koel, B. E. (2003). Energy transport in metal nanoparticle plasmon waveguides. *MRS Online Proceedings Library* (OPL), 777.

[143] Roller, E. M., Besteiro, L. V., Pupp, C., Khorashad, L. K., Govorov, A. O., & Liedl, T. (2017). Hotspot-mediated non-dissipative and ultrafast plasmon passage. *Nature physics*, 13(8), 761-765.

[144] Hu, L., Liedl, T., Martens, K., Wang, Z., & Govorov, A. O. (2019). Long-range plasmon-assisted chiral interactions in nanocrystal assemblies. *ACS Photonics*, 6(3), 749-756.

[145] Born, M. (1918). Elektronentheorie des natürlichen optischen Drehungsvermögens isotroper und anisotroper Flüssigkeiten. Annalen der Physik, 360(3), 177-240.

[146] Kuhn, W. (1930). The physical significance of optical rotatory power. *Transactions of the Faraday Society*, 26, 293-308.

[147] Auguié, B., Alonso-Gómez, J. L., Guerrero-Martínez, A., & Liz-Marzán, L. M. (2011). Fingers crossed: Optical activity of a chiral dimer of plasmonic nanorods. *The Journal of Physical Chemistry Letters*, 2(8), 846-851.

[148] Davis, M. S., Zhu, W., Lee, J. K., Lezec, H. J., & Agrawal, A. (2019). Microscopic origin of the chiroptical response of optical media. *Science advances*, 5(10), eaav8262.

[149] Pomplun, J., Burger, S., Zschiedrich, L., & Schmidt, F. (2007). Adaptive finite element method for simulation of optical nano structures. *physica status solidi (b)*, 244(10), 3419-3434.

[150] Johnson, W. R., Kolb, D., & Huang, K. N. (1983). Electric-dipole, quadrupole, and magnetic-dipole susceptibilities and shielding factors for closed-shell ions of the He, Ne, Ar, Ni (Cu+), Kr, Pb, and Xe isoelectronic sequences. *Atomic Data and Nuclear Data Tables*, 28(2), 333-340.

[151] Liedl, T., Sobey, T. L., & Simmel, F. C. (2007). DNA-based nanodevices. *Nano Today*, 2(2), 36-41.

[152] Ijäs, H., Nummelin, S., Shen, B., Kostiainen, M. A., & Linko, V. (2018). Dynamic DNA origami devices: from strand-displacement reactions to external-stimuli responsive systems. *International journal of molecular sciences*, 19(7), 2114.

[153] Simmel, F. C., & Yurke, B. (2001). Using DNA to construct and power a nanoactuator. *Physical Review E*, 63(4), 041913.

[154] Yan, H., Zhang, X., Shen, Z., & Seeman, N. C. (2002). A robust DNA mechanical device controlled by hybridization topology. *Nature*, 415(6867), 62-65.

[155] von Delius, M., & Leigh, D. A. (2011). Walking molecules. *Chemical Society Reviews*, 40(7), 3656-3676.

[156] Pan, J., Li, F., Cha, T. G., Chen, H., & Choi, J. H. (2015). Recent progress on DNA based walkers. *Current opinion in biotechnology*, 34, 56-64.

[157] Yin, P., Yan, H., Daniell, X. G., Turberfield, A. J., & Reif, J. H. (2004). A unidirectional DNA walker that moves autonomously along a track. *Angewandte Chemie*, 116(37), 5014-5019.

[158] Bath, J., Green, S. J., & Turberfield, A. J. (2005). A free-running DNA motor powered by a nicking enzyme. *Angewandte Chemie International Edition*, 44(28), 4358-4361.

[159] Yin, P., Choi, H. M., Calvert, C. R., & Pierce, N. A. (2008). Programming biomolecular self-assembly pathways. *Nature*, 451(7176), 318-322.

[160] Wickham, S. F., Endo, M., Katsuda, Y., Hidaka, K., Bath, J., Sugiyama, H., & Turberfield, A. J. (2011). Direct observation of stepwise movement of a synthetic molecular transporter. *Nature nanotechnology*, 6(3), 166-169.

[161] Sherman, W. B., & Seeman, N. C. (2004). A precisely controlled DNA biped walking device. *Nano letters*, 4(7), 1203-1207.

[162] Shin, J. S., & Pierce, N. A. (2004). A synthetic DNA walker for molecular transport. *Journal of the American Chemical Society*, 126(35), 10834-10835.

[163] Omabegho, T., Sha, R., & Seeman, N. C. (2009). A bipedal DNA Brownian motor with coordinated legs. *Science*, 324(5923), 67-71.

[164] Wang, Z. G., Elbaz, J., & Willner, I. (2011). DNA machines: bipedal walker and stepper. *Nano letters*, 11(1), 304-309.

[165] Tian, Y., He, Y., Chen, Y., Yin, P., & Mao, C. (2005). A DNAzyme that walks processively and autonomously along a one-dimensional track. *Angewandte Chemie*, 117(28), 4429-4432.

[166] Lund, K., Manzo, A. J., Dabby, N., Michelotti, N., Johnson-Buck, A., Nangreave, J., ... & Yan, H. (2010). Molecular robots guided by prescriptive landscapes. *Nature*, 465(7295), 206-210.

[167] Wickham, S. F., Endo, M., Katsuda, Y., Hidaka, K., Bath, J., Sugiyama, H., & Turberfield, A. J. (2011). Direct observation of stepwise movement of a synthetic molecular transporter. *Nature nanotechnology*, 6(3), 166-169.

[168] Liber, M., Tomov, T. E., Tsukanov, R., Berger, Y., & Nir, E. (2015). A bipedal DNA motor that travels back and forth between two DNA origami tiles. *Small*, 11(5), 568-575.

[169] Wang, D., Vietz, C., Schröder, T., Acuna, G., Lalkens, B., & Tinnefeld, P. (2017). A DNA walker as a fluorescence signal amplifier. *Nano letters*, 17(9), 5368-5374.

[170] He, Y., & Liu, D. R. (2010). Autonomous multistep organic synthesis in a single isothermal solution mediated by a DNA walker. *Nature nanotechnology*, 5(11), 778-782.

[171] Gu, H., Chao, J., Xiao, S. J., & Seeman, N. C. (2010). A proximity-based programmable DNA nanoscale assembly line. *Nature*, 465(7295), 202-205.

[172] Cha, T. G., Pan, J., Chen, H., Salgado, J., Li, X., Mao, C., & Choi, J. H. (2014). A synthetic DNA motor that transports nanoparticles along carbon nanotubes. *Nature nanotechnology*, 9(1), 39-43.

[173] Cha, T. G., Pan, J., Chen, H., Robinson, H. N., Li, X., Mao, C., & Choi, J. H. (2015). Design principles of DNA enzyme-based walkers: translocation kinetics and photoregulation. *Journal of the American Chemical Society*, 137(29), 9429-9437.

[174] Jung, C., Allen, P. B., & Ellington, A. D. (2016). A stochastic DNA walker that traverses a microparticle surface. *Nature nanotechnology*, 11(2), 157-163.

[175] Yehl, K., Mugler, A., Vivek, S., Liu, Y., Zhang, Y., Fan, M., ... & Salaita, K. (2016). High-speed DNA-based rolling motors powered by RNase H. *Nature nanotechnology*, 11(2), 184-190.

[176] Douglas, S. M., Chou, J. J., & Shih, W. M. (2007). DNA-nanotube-induced alignment of membrane proteins for NMR structure determination. *Proceedings of the National Academy of Sciences*, 104(16), 6644-6648.

[177] Ye, X., Jin, L., Caglayan, H., Chen, J., Xing, G., Zheng, C., ... & Murray, C. B. (2012). Improved size-tunable synthesis of monodisperse gold nanorods through the use of aromatic additives. *ACS nano*, 6(3), 2804-2817.